THERMAL DESORPTION, PHOTODESORPTION, AND PHOTODISSOCIATION OF WATER ON AMORPHOUS ICE AND LUNAR SURFACES

A Dissertation
Presented to
The Academic Faculty

by

Alice Johnson DeSimone

In Partial Fulfillment
of the Requirements for the Degree
Doctor of Philosophy in the
School of Chemistry and Biochemistry

Georgia Institute of Technology
December 2013

THERMAL DESORPTION, PHOTODESORPTION, AND PHOTODISSOCIATION OF WATER ON AMORPHOUS ICE AND LUNAR SURFACES

Approved by:

Dr. Thomas Orlando, Advisor
School of Chemistry and Biochemistry
Georgia Institute of Technology

Dr. Jiri Janata
School of Chemistry and Biochemistry
Georgia Institute of Technology

Dr. Ken Brown
School of Chemistry and Biochemistry
Georgia Institute of Technology

Dr. Paul Wine
School of Chemistry and Biochemistry
Georgia Institute of Technology

Dr. Greg Huey
School of Earth and Atmospheric Sciences
Georgia Institute of Technology

Date Approved: October 31, 2013

ACKNOWLEDGEMENTS

I wish to thank my advisor, Dr. Thomas Orlando, and the entire Orlando group for valuable discussions, assistance in the lab, and moral support throughout my years in graduate school. I would especially like to recognize the assistance of Drs. Gregory Grieves, Alexandr Aleksandrov, Jason McClain, and Reuben Gann. These research scientists and postdocs taught me about ultrahigh vacuum equipment, lasers, power tools, LabVIEW programming, and everything else in the lab that was a complete mystery to me five years ago. Outside the lab, my family has been a great source of strength for me. My parents gently nurtured my love of school as I was growing up, and they fill my life with joy, especially when singing and running with me. My grandparents have shown me that education is a life-long endeavor that becomes even more fun as you get older. My brother makes me laugh and inspires me with his desire to help others. Finally, my loving husband helped me to believe that everything would be all right even when the laser was broken.

TABLE OF CONTENTS

LIST OF TABLES

LIST OF FIGURES

SUMMARY

Water plays a central role in interstellar, planetary, and atmospheric chemistry, so understanding the interactions of water with ultraviolet photons and low-temperature surfaces is extremely important. Recent discoveries of water and/or hydroxyls on the Moon have made lunar substrates appropriate for experiments involving desorption and dissociation of water. The competition between photodissociation and photodesorption of amorphous solid water (ASW) has been investigated on three substrates: copper with a thin oxide coating, an impact melt breccia from Apollo 16, and a mare basalt from Apollo 17. Additionally, in order to better understand the observed variations in lunar water abundance with temperature, mineral composition, and crystallinity, the temperature-programmed desorption (TPD) profiles of water from three lunar analogs were measured.

These temperature-programmed desorption experiments showed that glassy materials were hydrophobic, that water on multiphase materials occupied a continuum of adsorption sites, and that feldspar exhibited significant chemisorption of water. The TPD results in Chapter 2 were published in *Icarus* as part of a larger study that also involved infrared measurements of water on lunar analogs by Carl Hibbitts and modeling of water migration within the lunar regolith by Greg Grieves.[1] The TPD instrumentation, data acquisition, and data analysis were done in collaboration with Alexandr Aleksandrov and Michael Poston.

The photodesorption of water molecules from amorphous solid water by 157-nm irradiation has been examined using resonance-enhanced multiphoton ionization on oxide-coated copper and on two lunar slabs: an impact melt breccia and a mare basalt.

The rotational temperature of desorbing H_2O did not vary significantly with substrate, but the time-of-flight (TOF) spectra were broader on the lunar slabs than on copper. Additionally, the cross sections for water removal at low coverages were higher on the lunar slabs than on copper. The results for H_2O photodesorption from ASW on copper (Chapter 3) were published in the *Journal of Chemical Physics* as part of a joint experimental and theoretical study with graduate student Vernon Crowell and Professor David Sherrill.[2]

$O(^3P_J)$ produced by 157-nm irradiation of ASW on copper and the two lunar substrates was measured as a function of spin-orbit state, H_2O exposure, and irradiation time. The same Maxwell-Boltzmann components were present in each case, with translational temperatures of 10,000 K, 1800 K, 400 K, and the surface temperature, but the relative intensities of these components differed widely between substrates. For example, the diffusion component was least significant on the oxidized copper surface and most significant on the porous mare basalt.

The experiments on the impact melt breccia presented in Chapters 4 and 6 will be submitted for back-to-back publication in the *Journal of Geophysical Research – Planets*. These papers will be called "Mechanisms and Cross Sections for Water Desorption from a Lunar Impact Melt Breccia" and "Photodissociation of Water and $O(^3P_J)$ Formation on a Lunar Impact Melt Breccia." Chapter 5 has been submitted for publication in the *Journal of Chemical Physics* with the title "$O(^3P_J)$ Formation and Desorption by 157-nm Photoirradiation of Amorphous Solid Water."

CHAPTER 1

INTRODUCTION

Water is one of the most thoroughly studied molecules in all areas of science due to its importance in creating and sustaining life, its abundance on Earth, its catalytic properties, and its many unique characteristics associated with hydrogen bonding. In physical chemistry, the interactions of water with ultraviolet photons and low-temperature surfaces have been extensively examined for their crucial roles in interstellar and planetary chemistry.[3, 4] In particular, recent discoveries of water or hydroxyls on the Moon have made lunar substrates prime candidates for experiments involving desorption or dissociation of water.[5]

1.1 Electronic Structure of Water

The electronic structure of water ice plays an important role in photodesorption and photodissociation of H_2O from amorphous solid water (ASW) and crystalline ice (CI). ASW is formed by depositing water vapor at substrate temperatures below 140 K, while deposition at higher temperatures results in formation of CI. The electronic structures of ASW and CI are essentially the same,[6] but they differ in several respects from that of gas-phase water. The ground-state electron configuration of a gas-phase water molecule is $1a_1^2 2a_1^2 1b_2^2 3a_1^2 1b_1^2$. The ground-state configuration in water ice is the same, but the energy levels are broader and shifted. Figure 1.1 directly compares the energies of molecular orbitals for an isolated water molecule with the band energies of a solid-phase water molecule.[7] Due to hydrogen bonding between water molecules, bands with a_1

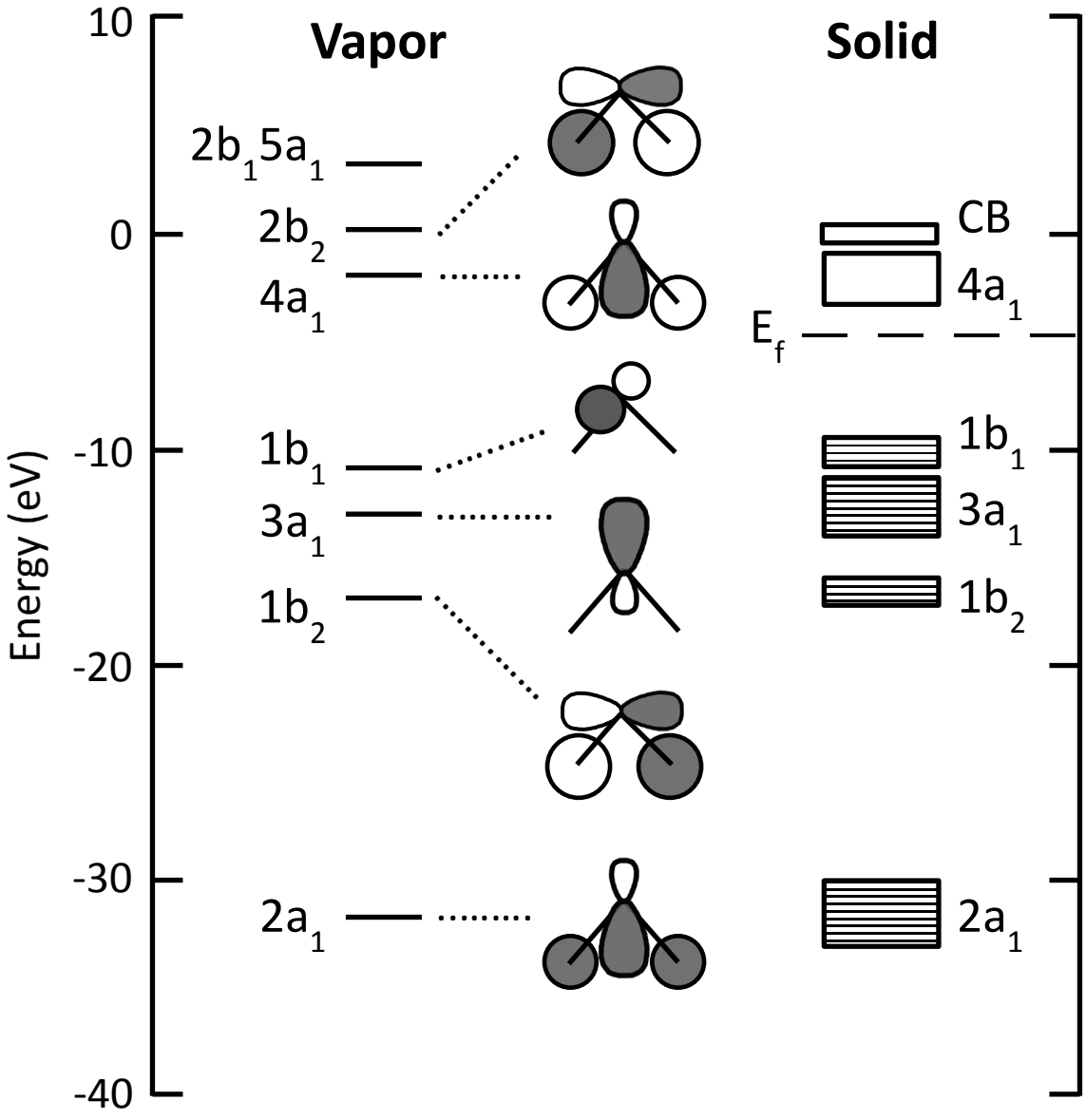

Figure 1.1. Electronic structure diagrams for a gas-phase water molecule (left) and solid water ice (right). Energies are referenced to the vacuum level. For each molecular orbital, the contributing atomic orbitals are shown in the center.

character are significantly wider in the solid phase than in the gas phase. These a_1 orbitals have been shown to facilitate electron travel along the hydrogen bond axis in water dimers, while the b_1 and b_2 orbitals promote electron motion perpendicular to that axis.[8] Consequently, the b_1 and b_2 orbitals are not as broadened by condensation as the a_1 orbitals are, and excitations involving a_1 orbitals are most affected by hydrogen bonding.

The first excited state of an isolated water molecule is dissociative, as it contains a hole in the $1b_1$ non-bonding orbital and an electron in the $4a_1$ anti-bonding orbital. However, in the condensed phase, coupling to neighboring water molecules leads to charge delocalization and potential pathways to desorption of intact water molecules.[9] For ASW and CI, insulating materials in which holes and electrons have significant lifetimes before recombination, excited electronic states can be considered excitons, which may have Frenkel and Wannier character. A Frenkel exciton is about the same size as the unit cell due to strong Coulomb interactions between the electron and the hole,[10] while a Wannier exciton has a radius larger than the lattice spacing.[11] Upon condensation, the first excited state of water becomes a band (sometimes labeled $\tilde{A}^1B_1$) of $1b_1 \rightarrow 4a_1$ transitions with ~7-9.5 eV, peaked at 8.7 eV, and the second band includes higher $1b_1 \rightarrow 4a_1$ exciton states as well as $3a_1 \rightarrow 4a_1$ transitions and peaks at ~10.2 eV.[12]

When these energies are available from solar photons, a competition between desorption and dissociation of water may occur. Quantum-dynamical simulations performed on a variety of hexamer isomers showed that delocalization of the exciton, which is associated with desorption, is on the same femtosecond time scale as photodissociation.[13] Even though the first excited state of an isolated water molecule is

dissociative, intermolecular interactions may allow condensed-phase water molecules to desorb intact.

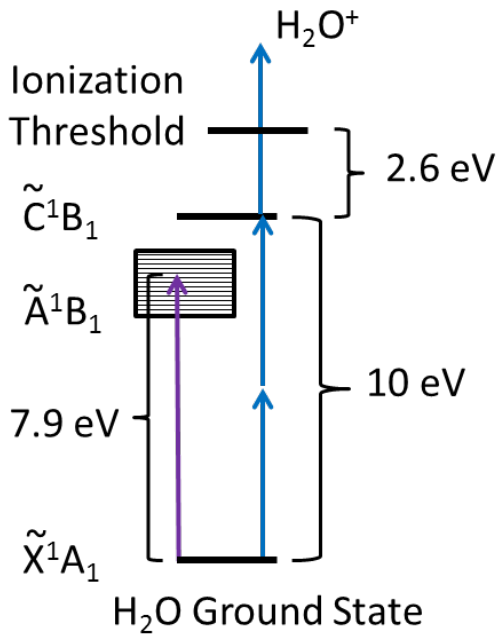

Figure 1.2. Diagram showing the ground and excited electronic states involved in one-photon desorption and 2 + 1 resonance-enhanced multiphoton ionization (REMPI) of water. Initial 7.9-eV excitation (shown in purple) can cause desorption of a neutral, ground-state water molecule. Subsequent ionization requires three 5-eV photons (shown in blue), two for resonant excitation and one for ionization.

When neutral water molecules desorb, they can be detected by resonance-enhanced multiphoton ionization (REMPI), which also requires detailed knowledge of water's electronic structure. Figure 1.2 illustrates one-photon excitation of water ice on the left and 2 + 1 REMPI of a desorbed water molecule on the right. Initial excitation to the first band of excited states ($\tilde{A}^1B_1$) by a 7.9-eV photon can cause desorption of a neutral, ground-state water molecule (see Chapter 3). In order to detect neutral water molecules with time-of-flight mass spectrometry, they must be ionized. This ionization is

greatly enhanced by the use of photons that can resonantly excite the water molecule. The REMPI scheme shown in Figure 1.2 requires three 5-eV photons, two for resonant excitation to the $\tilde{C}^1B_1$ state and one for ionization.

1.2 Water Adsorption on Metal Oxide Surfaces

For very thick ice, intermolecular hydrogen-bonding between water molecules is the main cause for electronic structure changes. However, when a small amount of water adsorbs on a surface, the forces between individual water molecules and the surface may play a more important role. Depending on the strength of the adsorbate-surface interaction, the adsorption is known as either physisorption or chemisorption. Physisorption involves weak attraction due to van der Waals forces, while chemisorption is characterized by the formation of covalent or ionic bonds with surface atoms and may change the adsorbate's electronic structure. Another possibility is dissociative adsorption, when a water molecule breaks apart into OH and H in order for both fragments to bond with the surface.

Molecular chemisorption of water on metals occurs through the oxygen atom's lone pairs,[14] and there is a strong tendency for water molecules to cluster. On single-crystal metal oxides, the water molecules are attached to specific cation sites via their oxygen lone pairs and hydrogen-bonded clusters are less likely to form.[3] Some metal oxides, including ZnO and Ti_2O_3, exhibit relatively strong chemisorption bonds, with molecularly adsorbed water that is stable up to room temperature, while chemisorbed water on metals generally desorbs at much lower temperatures [by ~190 K on Ni(111)].[3] Additionally, dissociative adsorption is more likely on metal oxides than on metals. The

primary factor that determines whether dissociative adsorption occurs on a defect-free metal oxide is the availability of both metal and oxygen atoms on the surface. Dissociative adsorption of water takes place on the Fe_3O_4 (111) surface, where hydroxyl fragments bind to surface iron atoms and hydrogen fragments bind to neighboring surface oxygen atoms.[15] However, the FeO (111) surface, which is oxygen-terminated, does not allow water to dissociate because there are no adsorption sites for hydroxyl groups.[15] Thus, for single-crystal metal oxides, surface termination largely determines how water adsorbs.

Unlike defect-free single crystals, powdered metal oxides contain many defect sites and facet edges that promote dissociative adsorption. Work on powders of common oxides, such as Al_2O_3, indicates that H_2O is efficient in hydroxylating the surface.[3] Temperature-programmed desorption (TPD) of water from a highly dispersed alumina/silica sample exhibits desorption of molecular water at 429 K and diffusion-limited recombinative desorption involving isolated hydroxyl groups at a continuum of higher temperatures.[16] Thus, powdered metal oxides generally have very stable chemisorption sites for both water and hydroxyl groups.

Metal oxides that are not powdered may also have abundant defect sites, depending on how and where they were formed. Protons, electrons, and other ions from the solar wind constantly bombard the lunar surface, creating defects, such as oxygen vacancies, that could facilitate adsorption of water. Surfaces of oxide single crystals, such as TiO_2 (110), which have been ion-bombarded to produce defects can cause dissociation of H_2O, whereas pristine surfaces of the same compounds do not.[3] The adsorption behavior of water on metal oxides is strongly dependent on defect density.

Not only does the lunar surface continuously experience the defect-creating solar wind, it is also composed of a wide variety of metal oxides, so there are plenty of grain boundaries on which chemisorption can occur. The primary focus of this research is to examine the adsorption, desorption, and dissociation of water on lunar surfaces, which are mixtures of metal oxides. For comparison, these processes are also explored on thick ASW.

CHAPTER 2

TEMPERATURE-PROGRAMMED DESORPTION OF WATER FROM LUNAR ANALOGS

2.1 Introduction

The search for water on the Moon began even before the first man landed on the Moon, with a prediction that water would be stable for billions of years in permanently shadowed areas with temperatures as low as 120 K.[17] Volatile deposits in cold traps at the lunar poles could provide valuable information about the history of the Earth-Moon system over the last two billion years. The samples of the lunar regolith collected by Apollo astronauts in the early 1970s proved to be extremely desiccated, but these samples were not from the extremely cold polar regions. In the 1990s, several experiments attempted to prove the existence of water on the Moon.

The first piece of evidence supporting the theory that water could be trapped near the poles came from the Clementine bistatic radar experiment.[18] The Clementine spacecraft transmitted right-circularly polarized (RCP) radio signals toward the North and South Poles of the Moon, and reflections were received and analyzed on Earth. Total internal reflection, characteristic of volatile ices, tends to preserve the original sense of circular polarization in the reflected signal. A significant enhancement in RCP signal was observed over permanently shadowed regions of the South Pole, while sunlit regions exhibited no such enhancement.

In response to the Clementine data, Earth-based radar observations taken at the Arecibo Observatory were published.[19] Small areas were found with high circular

polarization ratios both in sunlit areas on crater slopes and in permanently shadowed areas. The team at Arecibo thus concluded that very rough surfaces, rather than water ice, were responsible for the radar features. Subsequent high-resolution measurements confirmed the correlation between RCP signal enhancement and the presence of crater walls or ejecta deposits.[20]

Still without any conclusive evidence for water on the Moon in 1998, NASA sent Lunar Prospector to orbit and then impact the Moon. No ice was detected in the impact plume, but data from Lunar Prospector's neutron spectrometer provided compelling evidence for hydrogen, possibly in water, at the lunar poles.[21] Depressions in epithermal neutron fluxes observed near permanently shaded areas at both poles were consistent with deposits of hydrogen covered by up to 40 centimeters of regolith. However, as with Clementine, the Lunar Prospector conclusions have been questioned due to surface roughness complications, as similar depletions of epithermal neutrons can be caused by structured surfaces of dry materials.[22]

In 2009, an issue of *Science* highlighted the lunar water question with articles revealing data from the Deep Impact Spacecraft, the Visual and Infrared Mapping Spectrometer (VIMS), and the Moon Mineralogy Mapper (M^3).[23-25] These three articles supported the presence of water on the Moon with infrared (IR) absorption data showing broad 3-μm hydration features. Maximum IR absorption was seen at 2.8 μm, indicating stretching vibrations of hydroxyls, and less intense absorption at wavelengths greater than 3.0 μm were attributed to H_2O. While Deep Impact detected 3-μm absorption at all latitudes greater than 10 °N, this absorption was greatest in polar regions.[24] According to radiative transfer models, VIMS data were consistent with up to 1000 ppm H_2O on the

sunlit lunar surface.[23] While these data seem to be compelling evidence for water on the Moon, there are several possible vibrations that could be excited near 3 μm. For instance, structural OH in minerals can have stretching vibrations between 2857 and 3333 nm.[26]

More convincing evidence for water on the Moon has come from the impact plume made by the Lunar CRater Observation and Sensing Satellite (LCROSS) on October 9, 2009. Both UV emissions and IR absorption data from LCROSS indicated that water and hydroxyls were excavated by the impact into a permanently shadowed region of the Cabeus crater near the South Pole.[27, 28] LCROSS uncovered water from deep within the crust, so it had not been exposed to sunlight for an extremely long time. Indeed, Monte Carlo simulations of space weathering processes indicated that ice deposits in the Cabeus crater may have been more than a billion years old.[29] Very recently, M^3 found hydroxylated minerals excavated from deep within lunar interior, suggesting that water ice may also be present below the Bullialdus Crater.[30]

Earth-based laboratory experiments can also provide valuable information relevant to the presence of water on the Moon. Since ambient pressure on the Moon is approximately 1×10^{-12} Torr,[31] ultrahigh vacuum (UHV) conditions are appropriate. Not many modern surface science techniques have been applied to water on lunar materials thus far. However, temperature-programmed desorption (TPD) of water deposited on a lunar simulant known as JSC-1A has been measured in a UHV chamber, and desorption temperatures between 140 and 450 K were reported.[32] The temperature of the lunar surface varies between about 100 and 400 K during a lunation,[33] so thermal desorption of water could certainly occur on the Moon. Because the predominant form of hydrogen on

the illuminated portion of the Moon is likely OH, recombinative desorption of water is especially important to investigate.

The Moon has two basic kinds of terrain, the highlands and the maria (singular *mare*). Maria are the dark-colored lunar plains of solidified basaltic lava, and the highlands are light-colored, heavily cratered regions where anorthositic rocks are common. Both basalts and anorthosites are aluminosilicates containing iron, calcium, magnesium, and other metals in lower concentrations. However, basalts have much more iron than anorthosites. In order to better understand the observed variations in lunar water abundance with temperature, mineral composition, and crystallinity, the temperature-programmed desorption profiles of water from three lunar analogs were measured.

2.2 Experimental Details

2.2.1 Lunar analogs

Water TPD analyses were performed on a basaltic glass slab, a powdered lunar mare analog (JSC-1A), and a powdered highland analog (Bancroft albite). The powders were manufactured from coarsely-crushed samples by wet grinding each material for ~20 minutes in a micronizing mill, producing ~1–5 μm particle sizes that were verified through optical and scanning electron microscopy (SEM) imaging. Brunauer, Emmett, and Teller (BET) analysis along with the SEM images revealed the surface area of JSC-1A to be ~8 m^2/g, while the Bancroft albite had a surface area of ~17 m^2/g.

An iron-rich basaltic glass, prepared under relatively dry conditions (~ 660 ppm H_2O by FTIR), was the first substrate studied. As shown in Table 2.1, this analog's composition is similar to that of lunar soil.[1] However, the surface structure may be quite

different from genuine lunar glasses, which are usually formed by impacts. Water does not generally chemisorb on terrestrial or synthetic glasses due to their low porosity and oxygen-terminated surfaces. In contrast, lunar glasses often have many surface defects due to micrometeoroid damage, and these defects may become chemisorption sites for water.

Table 2.1. Elemental compositions (% by mass) of lunar analogs and a real lunar sample.

Sample	SiO_2	TiO_2	Al_2O_3	MgO	CaO	Na_2O	K_2O	Fe_2O_3	Total
Glass	45.69	0.97	12.82	6.39	12.57	0.29	0.04	21.23	100
JSC-1A	47.71	1.59	13.02	9.01	10.42	2.7	0.82	10.79	96.06
Albite	63.22	0.01	22.83	0.04	4.43	7.87	1.42	0.18	100
Apollo 14	47.3	1.6	17.8	9.6	11.4	0.7	0.6	10.5	99.5

JSC-1A was created to simulate lunar regolith in the maria, which are composed of space-weathered basalts. Although the total iron content of JSC-1A shown in Table 2.1 closely matches that of a real lunar sample, different oxidation states of iron are not distinguished, as Table 2.1 lumps them all together. JSC-1A contains both Fe^{3+} (~24%) and Fe^{2+} (~76%), while actual lunar soil contains Fe^{2+} ions and nanophase Fe^0.[34, 35] Nanophase iron content was correlated with hydroxyl radical production when freshly ground lunar soil was in solution,[36] so the omission of nanophase iron from JSC-1A could lead to reduced reactivity. Additionally, the particle size distribution and surface roughness of JSC-1A do not match those of lunar soils, but micronizing the JSC-1A diminishes these differences.

The chemical composition of the Bancroft albite in Table 2.1 was determined by Casey et al.[37] Both albite ($NaAlSi_3O_8$ when pure) and anorthosite ($CaAl_2Si_2O_8$ when pure) are plagioclase feldspars, but they differ in sodium and calcium contents. The lunar highlands are primarily anorthositic, so they contain more calcium than the albite used as an analog. All feldspars probably exhibit similar water desorption profiles due to their similar structures, but the exact desorption temperatures may be different. Varying the relative concentrations of charge-compensating cations (Na^+ or Ca^{2+}) can shift the chemisorption peak, as observed for NO_2 on zeolite, another aluminosilicate.[38]

2.2.2 Experimental setup

TPD experiments on the basaltic glass were performed in a UHV chamber (base pressure = 2×10^{-10} Torr) equipped with a quadrupole mass spectrometer (QMS), a leak valve for dosing, a tungsten filament for radiative heating, a liquid nitrogen reservoir for cooling, and a copper sample mount. The basaltic glass sample was mounted vertically at the end of a long piece of copper whose other end attached to the liquid nitrogen reservoir. In order to reduce background desorption signal from this long copper piece, a copper shield was constructed that wrapped tightly around the liquid nitrogen reservoir on one end and surrounded the long copper sample mount without touching it. This shield significantly improved cooling by blocking much of the blackbody radiation from the room-temperature chamber walls, reduced the amount of water that adsorbed on and desorbed from the sample mount, and pushed the onset of the background desorption peak to a higher temperature.

Water was dosed at the lowest possible temperature (~100 K) through a tube that extended to about 2 mm away from the sample. The chamber pressure was measured with an ion gauge, but the local pressure at the sample during direct dosing was unknown, so a series of TPD experiments using background dosing without the extension tube were performed in order to better estimate the exposure. For background dosing, one Langmuir (L) is equivalent to one second of exposure at a chamber pressure of 10^{-6} Torr. The exposure calculated for background dosing was strongly correlated with the integrated area of the TPD peak due to desorption from the sample. The resulting calibration curve was used to calculate exposures obtained with direct dosing. After dosing, the chamber pressure was allowed to stabilize before the temperature ramp began. While water signal was monitored with the QMS, the sample temperature was increased at a nearly constant rate (usually 0.5 K/s).

While the UHV chamber described above worked reasonably well for glass samples, the vertically mounted sample holder was not suitable for studying powdered samples. Consequently, TPD experiments on JSC-1A and albite were performed in a different UHV system (Figure 2.1) that was specifically constructed to examine the uptake and release of water from powdered samples. A horizontally-mounted sample holder was cooled to ~110 K via mechanical contact with a liquid-nitrogen reservoir. The cooling stage could be disconnected from the sample holder so that the cooling stage never reached the temperature required for water desorption (~140 K) during heating of the sample. As an additional precaution against background desorption signal, the sample holder was chemically plated with several micrometers of gold, reducing water adsorption on exposed portions of the sample holder.

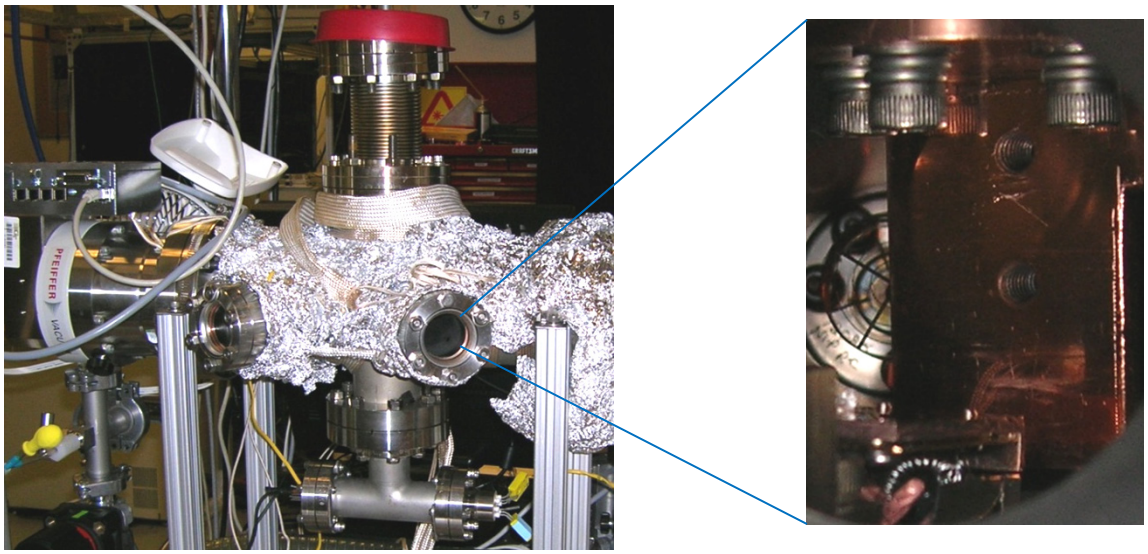

Figure 2.1. Ultrahigh vacuum chamber specifically designed for temperature-programmed desorption experiments. The sample holder is horizontal. The movable cooling stage is vertical or nearly vertical, depending on whether a wedge is placed between the two top flanges.

For experiments involving JSC-1A and albite, a small amount of powdered sample, equivalent to < 10 layers, was distributed uniformly over the sample holder. The use of a small amount of sample minimized potential complications from diffusion of water through the powdered samples during desorption measurements. After introduction into the UHV chamber, the lunar analogs were degassed overnight at ~750 K to remove surface water, hydroxyls, and organic contaminants before conducting the TPD experiments. The samples were then cooled to ~110 K and dosed with a controlled amount of water. A heating rate of 0.5 K/s was typically used, and the rate of water desorption was directly measured by monitoring the m/z = 18 peak with a QMS.

2.2.3 Data fitting procedure

When an adsorbed molecule is bound to the surface in a potential well of depth E_{des}, the probability that it will desorb at any given temperature (T) is governed by Maxwell-Boltzmann statistics. The rate law for desorption can be described by the Polanyi–Wigner equation:

$$-\frac{d\theta}{dt} = \nu \cdot \theta^n \cdot \exp\left(\frac{-E_{des}}{R \cdot T}\right), \quad (2.1)$$

where θ is instantaneous coverage at time t, ν is a frequency factor, n is the desorption order, and E_{des} is the activation energy for desorption. The frequency factor depends on adsorbate, and $\nu = 10^{13}$ s^{-1} is appropriate for water ice.[39] The desorption rate, - $d\theta/dt$, is proportional to the QMS signal intensity. The desorption order and activation energy are extracted from the experimental results. Three orders of desorption are typically observed in TPD. When n = 0, desorption rate is independent of coverage, indicating clusters or multi-layered adsorbates. First-order desorption typically corresponds to molecular chemisorption, and second-order desorption suggests recombinative desorption (e.g. OH + OH → H_2O + O).

2.3 Results

2.3.1 Basaltic glass

Figure 2.2 shows TPD data for five different exposures of water on the basaltic glass slab. A single desorption peak was observed from the basaltic glass at each exposure. The small shoulder at higher temperatures was due to background desorption from the sample holder. Although heating to 300 K was possible, no peaks from the sample were observed above 200 K. The water desorption peaks from the sample all share a common leading

edge with an exponential rise, and the temperature at peak maximum increases with coverage. This behavior indicates 0^{th} – order desorption, which is characteristic of multilayers or clusters. The fact that this multilayer desorption peak is observed even at coverages below 1 L indicates that water adsorption occurs by island formation. In other words, an adsorbing water molecule is more likely to stick to another water molecule than to the glass surface.

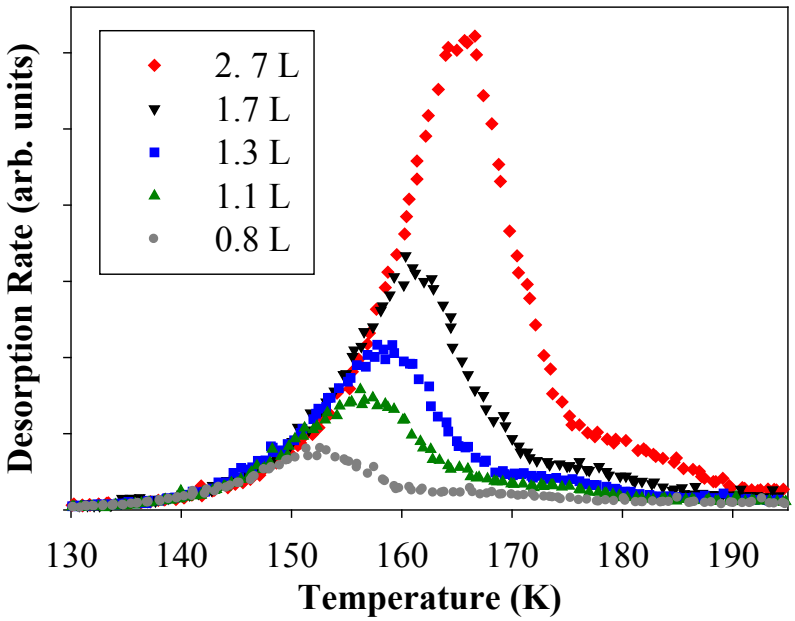

Figure 2.2. Temperature-programmed desorption of water at low exposures from the basaltic glass lunar analog. No peaks were observed below 130 K or between 200 and 300 K.

The data fitting results for TPD of 9.9 L water from the basaltic glass are shown in Figure 2.3. The large peak on the left is from the sample, while the smaller peak on the right is due to the copper sample holder. Several peaks corresponding to different coverages were also fit with equation (2.1). The average activation energy for desorption

was 0.45 eV with a standard deviation of 0.02 eV. Although this desorption appeared to be 0^{th} – order, $n = 0.8$ fit the data best due to our slow pumping speed.

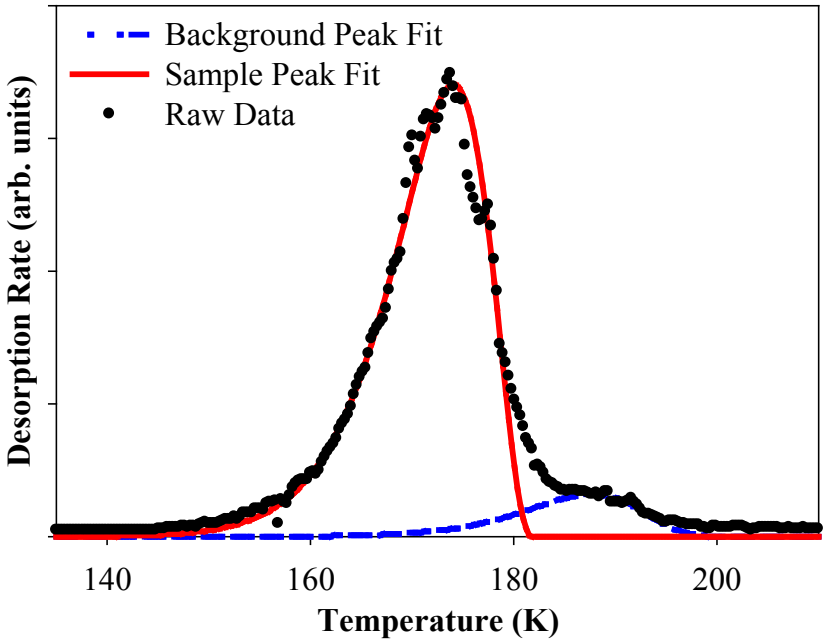

Figure 2.3. Temperature-programmed desorption of 9.9 L water from the basaltic glass. The solid red line is the Polanyi-Wigner fit to the sample desorption peak with n = 0.8, and the dashed blue line is the Polanyi-Wigner fit to the desorption peak from the copper sample holder.

2.3.2 JSC-1A

TPD of water from JSC-1A (Figure 2.4) revealed both cluster formation and molecular chemisorption of water for ≥ 1 L exposure. At exposures below 1 L, only chemisorbed water accumulated on JSC-1A, as indicated by the extremely broad peak around 225 K. This chemisorption peak had greater area than the multilayer ice peak at 160 K until ~8 L exposure. Because of the particulate nature of this sample, saturation of the chemisorption peak, which generally indicates a monolayer of coverage, did not occur until ~64 L exposure. The broad chemisorption peak likely resulted from a wide

distribution of chemisorbed states on this multiphase, mechanically micronized material composed of multiple minerals. A continuum of first-order desorption states was therefore indicated, so each desorption profile was fit with the sum of many Polanyi-Wigner curves. Calculated desorption energies ranged from about 0.5 to 1.2 eV, characteristic of physical states ranging from water clusters to strongly chemisorbed water.

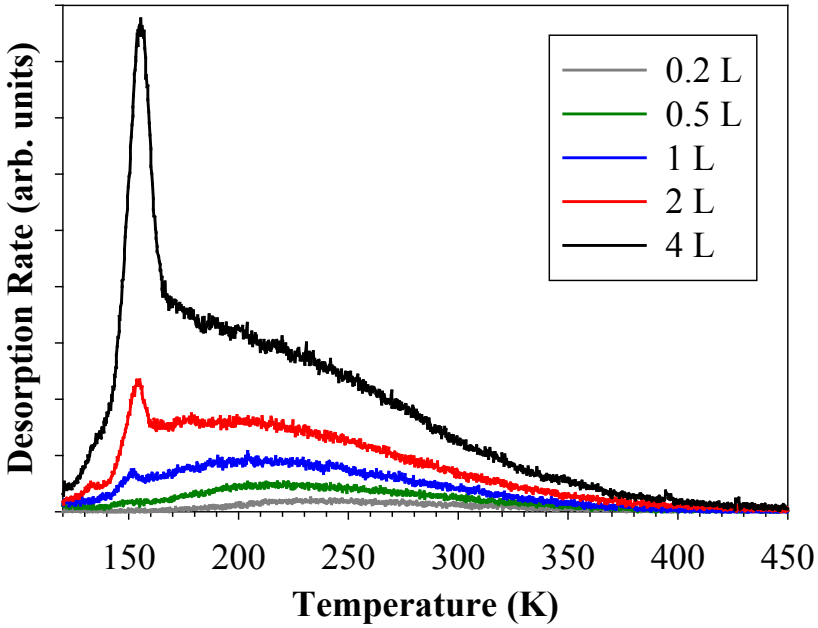

Figure 2.4. Temperature-programmed desorption curves of water from JSC-1A exposed to 0.2 – 4 L H_2O at a substrate temperature of 110 K.

2.3.3 Albite

The TPD of water from albite (Figure 2.5) was quite similar to the TPD of water from JSC-1A. On albite, the chemisorbed water has a well-defined desorption peak centered near 225 K, with a tail at higher temperatures demonstrating that some chemisorbed

water remains present until ~450 K. Since both albite and JSC-1A samples were powdered, many edge sites were available for chemisorption. Defects in the crystal structure of albite may provide additional chemisorption sites. At exposures < 1 L, only chemisorbed water accumulated on albite. As exposure increased above 1 L, both multilayer and chemisorption peaks grew, but the multilayer peak eventually became larger than the chemisorption peak. Saturation of the chemisorption peak did not occur even at 512 L exposure.

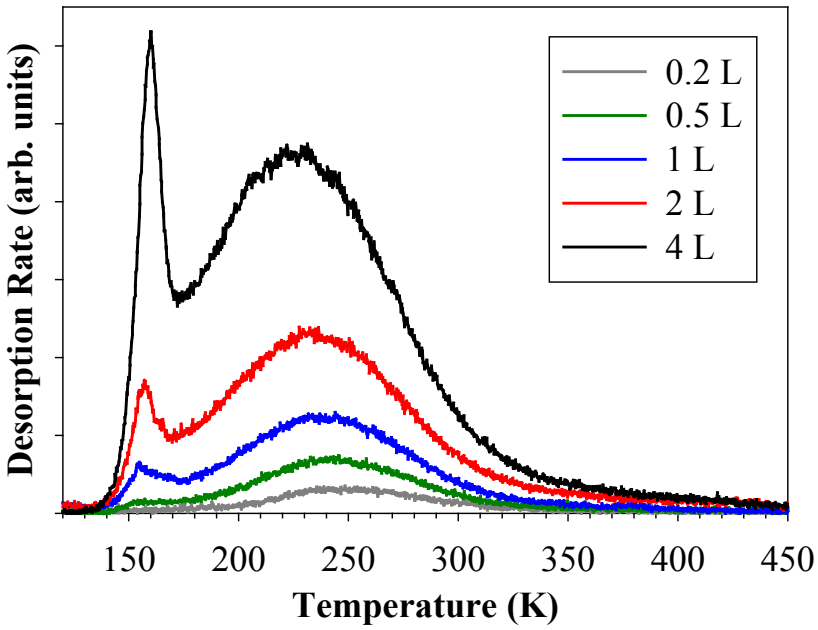

Figure 2.5. Temperature-programmed desorption curves of water from albite powder exposed to 0.2 – 4 L H_2O at a substrate temperature of 110 K.

2.4 Discussion

The fact that albite's chemisorption peak continued to grow even at 512 L exposure, while saturation occurred at 64 L on JSC-1A, suggests that albite has more chemisorption

sites than JSC-1A. As stated in Section 2.2.1, the BET surface area of albite was slightly more than twice that of JSC-1A, so the difference between the number of chemisorption sites on albite and JSC-1A is significant even after correcting for surface area. In addition, the chemisorption peak of JSC-1A is much broader, without a clear center. This difference is likely due to the fact that albite is a single mineral, while JSC-1A is a mixture of many minerals. Defect sites in albite apparently correspond to a desorption temperature of ~225 K, while defect sites in the minerals making up JSC-1A correspond to a wide range of desorption temperatures.

The basaltic glass substrate shows no evidence for chemisorption of water, as only the 0^{th} – order multilayer ice peak is observed. However, as mentioned in section 2.2.1, terrestrial and synthetic glasses have low porosity and oxygen-terminated surfaces that have very few defects when compared with lunar glasses. Therefore, it is not surprising that this basaltic glass slab seems to be hydrophobic, but lunar basaltic glasses may behave differently due to defects created by micrometeoroid bombardment.

These TPD results have significant implications for understanding the evolution of water on the Moon. For example, modelers can estimate how much water has accumulated on a permanently shadowed lunar surface and predict the amount of thermal desorption expected when the lunar surface grows warmer. In fact, Hibbitts et al. have used the above estimates of desorption energies to calculate that molecular water will desorb from a lunar grain in less than one lunation, even at temperatures as low as ~175 K.[1] However, since water has been observed on grains at this temperature, a source term is implicated, possibly migration of water from warmer to cooler parts of the lunar surface. In addition, temperature-dependent adsorption and desorption processes can

explain some of the observed distributions and variations of water on the Moon. Using the measured desorption energies for JSC-1A, Poston et al. have also estimated the diurnal concentrations of water for several lunar latitudes, assuming that a source of migrating water saturates the regolith each night, and small amounts of water are predicted to persist throughout the lunar day at temperatures above 150 K.[40]

2.5 Conclusion

The adsorption of water on lunar analog materials shows that glassy materials are hydrophobic, multiphase materials exhibit a continuum of desorption energies, and feldspar exhibits significant chemisorption of water. As expected, water adsorption depends strongly on the surface structure. The information reported in this chapter is critical to predicting the flux of water into and out of the lunar regolith. The desorption energies found by TPD will serve as input parameters for models of water diffusion through lunar regolith. Results of these calculations can be used in models of water transport from one spot on the Moon to another. These transport models can then provide more accurate results for how much water could be trapped in permanently shadowed areas. Non-thermal processes, such as photodissociation and photodesorption by solar UV irradiation, can also affect the stability of adsorbed water on the Moon. Photodesorption and photodissociation of water on lunar surfaces will be discussed in Chapters 4 and 6, respectively.

CHAPTER 3

H_2O PHOTODESORPTION FROM AMORPHOUS SOLID WATER

3.1 Introduction

Water ice is present on many low-temperature surfaces in the ring system of Saturn and throughout the outer solar system,[41, 42] and these icy grains are exposed to ultraviolet (UV) radiation. Even in astrophysical environments beyond the solar system, photodesorption of water by the far-UV component of the interstellar radiation field has been proposed to account for the large amount of water in the gas phase above cold surfaces.[43] Investigating the mechanisms and determining the cross section of H_2O photodesorption from amorphous solid water and crystalline ice are essential to understanding the electronic properties of these icy surfaces and the lifetime of ice in various solar system environments.

As mentioned in section 1.1, the first excited state of an isolated water molecule ($1b_1^{-1}4a_1^1$) is dissociative, but intact desorption is possible from this excited state in water ice due to exciton delocalization. The first absorption band in water ice consists of $1b_1 \rightarrow 4a_1$ transitions between 7 and 9.5 eV, and the second absorption band peaks at ~10.2 eV.[12] Several experimental studies of water desorption have been performed using radiation sources with energies in these two UV absorption bands, including a broadband (7–10.5 eV) hydrogen discharge lamp,[44] a more narrow Lyman-alpha source at 10.2 eV,[45, 46] two 248-nm photons at a total energy of 9.99 eV,[47] and an excimer laser at 7.89 eV.[48] The latter two experiments utilized pulsed lasers and yielded time-of-flight spectra, which were fit with Maxwell-Boltzmann distributions characterized by translational

temperatures, T_{trans}. The 9.99 eV radiation yielded T_{trans} = 770 K,[47] while the 7.89 eV radiation yielded T_{trans} = 1800 K.[48] The authors of these two studies also interpreted the results in terms of two different mechanisms. Hama et al.[48] supported the kick-out mechanism that was modeled using molecular dynamics simulations.[49] The kick-out mechanism involves the transfer of momentum from a hot H atom produced by photodissociation to a nearby H_2O molecule. Nishi et al.[47] previously proposed a more direct mechanism that involved the exchange repulsion between an excited water molecule and the surface. This exchange repulsion energy could lead to exciton migration, self-trapping at a surface, and eventual desorption of water molecules. In this case, though not stated in the model, the excitation can be visualized as a dipole reversal, and the resulting forces act to repel the excited water molecule from the surface. Another mechanism that may contribute to water desorption is recombination of photoproducts, in which the desorption signal increases with temperature.[50]

Theoretical work has shown that exciton delocalization competes with dissociation of water in ice. Quantum-dynamical simulations performed on a variety of hexamer isomers showed that delocalization of the exciton is on the same femtosecond time scale as photodissociation.[13] Even though the first excited state of an isolated water molecule is dissociative, condensed-phase water molecules may remain intact when excited due to intermolecular interactions. Previous theoretical studies on the nature of the excited state and delocalization probabilities have not investigated the possible role of dipole reversal in the competition between photodesorption and photodissociation of water molecules.

The aims of the present study are to discover the nature of the excited states that are involved in H_2O photodesorption, to examine mechanisms other than kick out by a hot H atom, and to determine the cross section for water removal from ASW at 7.9 eV. The photodesorption of H_2O from ASW due to 157-nm radiation has been studied using resonance-enhanced multiphoton ionization (REMPI). Rotational and translational energies of the desorbed water molecules have been determined by comparison with simulations. H^+ and OH^+ fragment ions have been detected with non-resonant multiphoton ionization, and the translational energies of their vibrationally excited parent water molecules have been deduced. The cross section for ice removal by 7.9-eV photons has been measured for various thicknesses.

3.2 Experimental Details

3.2.1 Laboratory measurements

Photodesorption experiments were performed in an ultra-high vacuum (UHV) chamber with a base pressure of 2×10^{-10} Torr. As shown in Figure 3.1, the chamber was equipped with a time-of-flight (TOF) mass spectrometer, two leak valves for dosing, and a liquid-nitrogen-cooled copper sample holder. All experiments were performed at the minimum sample temperature, 108 K, unless otherwise stated.

The copper substrate was not sputtered in between experiments, so a thin oxide layer probably coated the surface. Oxygen impurities on copper surfaces are known to promote dissociative adsorption of water, so this distinction between copper oxide and copper metal is important at low exposures.[51] On CuO (100), water chemisorbs molecularly at low temperatures and only dissociatively adsorbs above 198 K.[52]

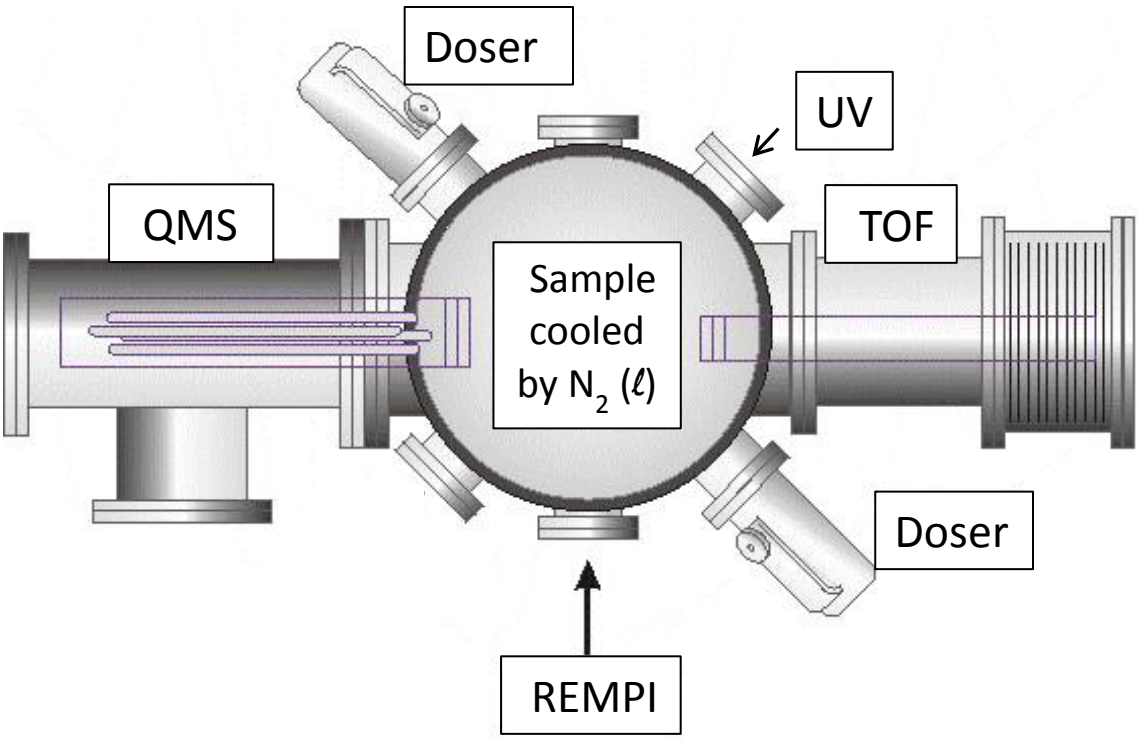

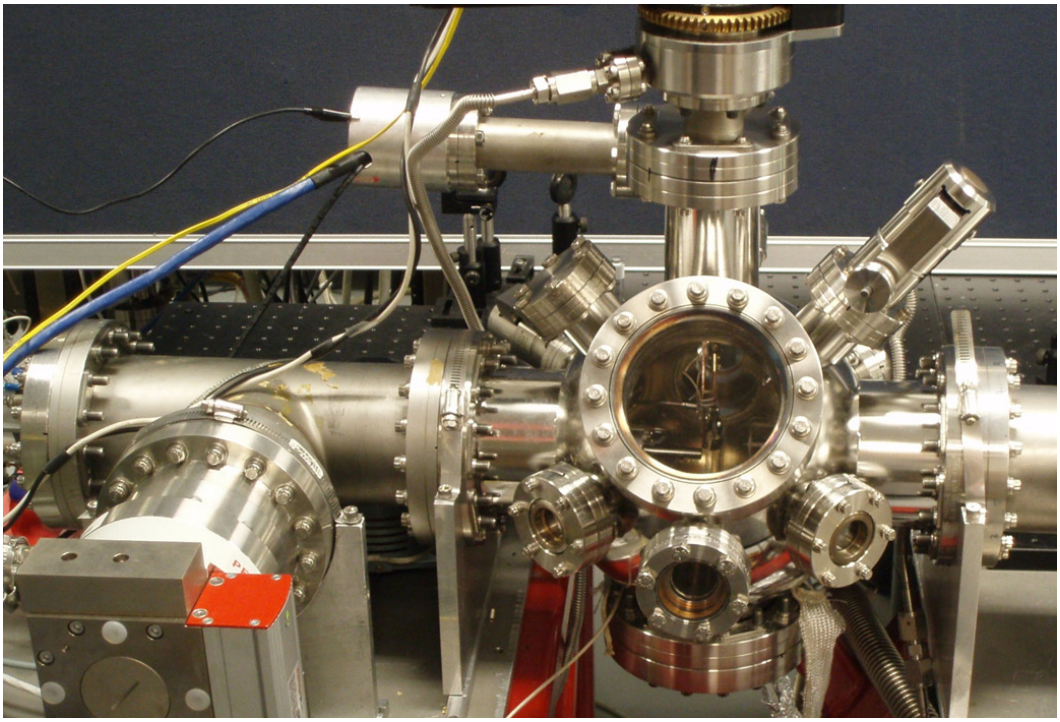

Figure 3.1. Schematic representation (top) and photograph (bottom) of the ultrahigh vacuum chamber used for all experiments described in Chapters 3-6.

On Cu_2O (100), about 10% of a monolayer of water is dissociated at 110 K, while adsorption is entirely dissociative at 300 K.[53] In the present study, the temperature of the copper with an oxide overlayer is 108 K, so minimal dissociative adsorption is expected when H_2O exposure is at least 1 L.

Unfocused 157-nm light from an excimer laser (GAM Laser, EX5) entered the chamber through a magnesium fluoride window and struck the sample at a 45° angle. To ensure that the desorption process was a single-photon event, low desorption pulse energies (50-90 μJ cm^{-2} per pulse) were used. An iris was placed in the N_2-purged beam path to control the radius of the irradiated region.

Desorbed water molecules were detected with 2 + 1 REMPI via the C(000)-X(000) transition, which corresponds to 247.8-248.6 nm. The wavelengths were obtained by frequency doubling the visible output of a Nd:YAG-pumped optical parametric oscillator (Spectra-Physics, MOPO-SL). The beam was focused between 1 and 4 mm above the surface with a focal volume of ~10 μm^3. This distance between the surface and the detection region was varied to ensure that the translational temperature obtained by fitting the data was the same at each distance.

The time between desorption and ionization was varied with a delay generator from 0 to 10 μs to probe different parts of the desorption plume. This delay time equals the flight time of the molecule from the surface to the REMPI detection region. The water peak in each mass spectrum was integrated to obtain the total water signal for each time delay. The resulting graph of water signal versus time is referred to as the TOF spectrum. Diagrams illustrating the laser alignment and timing of this experiment are shown in Figure 3.2.

For most experiments (if coverage is not specified), background dosing was performed for 20 minutes at a water pressure of 5 x 10^{-7} Torr, resulting in 600 L exposure (1 L = 1 x 10^{-6} Torr·s). The penetration depth of a 157-nm photon through ice is 120 nm,[12] or 230 ML at 45° to normal.[54] Assuming a sticking probability of at least 0.4, the ice was thick enough that the incoming photons did not reach the underlying substrate. Doses between 50 and 1000 L were found to produce the same TOF spectra. For doses between 5 and 50 L, while the shape of the distribution remained consistent, the amount of photodesorbed water decreased with increasing exposure, presumably due to decreasing surface area as the ice surface became smoother.

Water peak areas were collected over ~100,000 pulses in order to determine cross sections for water removal, σ. Water signal was plotted versus number of incident 157-nm photons, and the data were fit with exponential functions of the form $y = Ae^{-\sigma x}$, where x has units of photons cm^{-2}. The number of 157-nm photons was calculated using the pulse count on the excimer laser display, average excimer power measured before and after the scan, and a correction factor of 0.65 for losses passing through the MgF_2 window. Average excimer power was found to remain constant on the time scale of these experiments. However, the turbulent quality of the nitrogen purge in the purge tube affected the power, and much of the variation in water signal was likely due to the erratic desorption laser power. Ionization laser power was recorded at several times during these cross section measurements, and signal was corrected for the observed changes in average power.

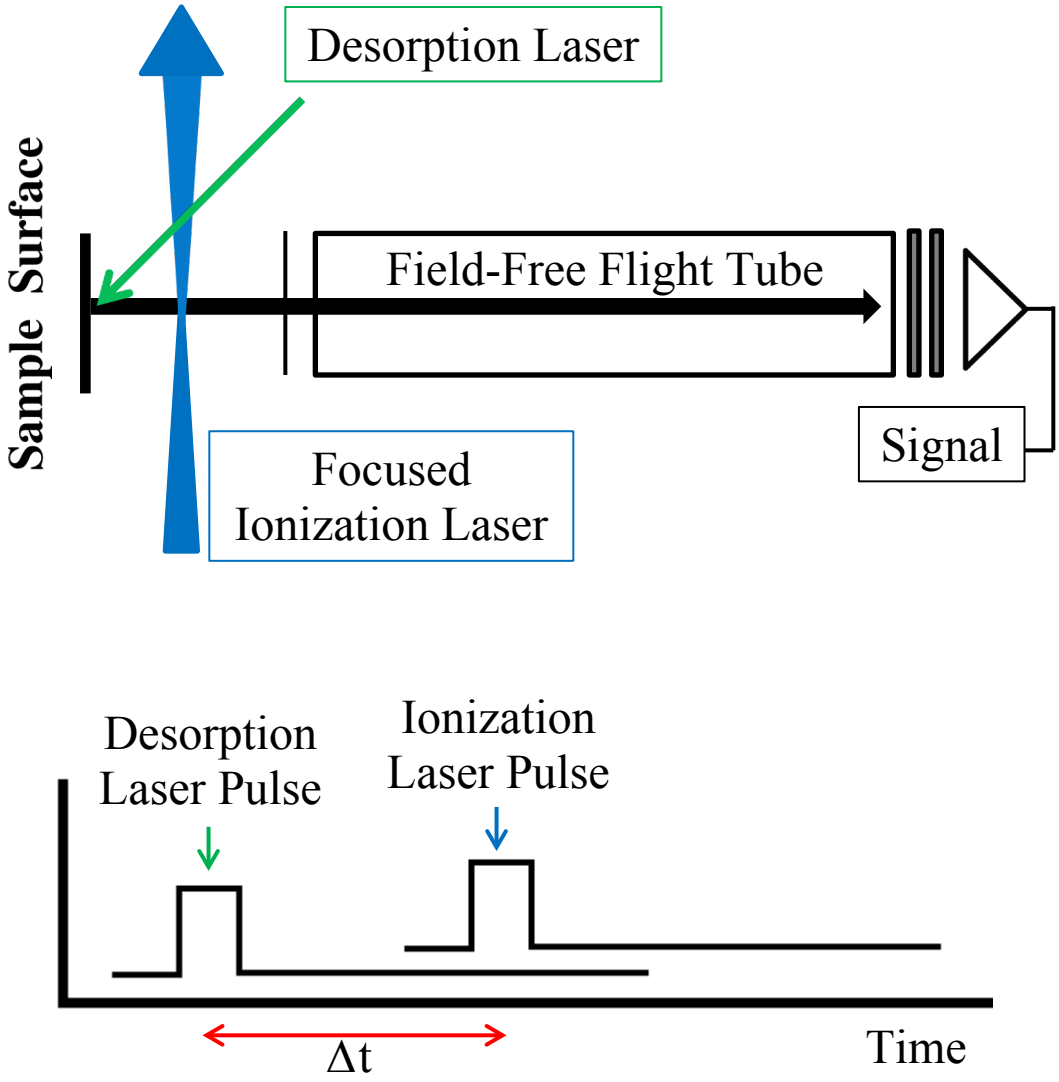

Figure 3.2. Spatial (top) and temporal (bottom) diagrams of the two-laser REMPI-TOF experimental setup. The unfocused 157-nm desorption laser beam strikes the sample at a 45° angle. After a brief delay time (Δt), the focused ionization laser beam passes through the desorption plume. Positive ions are accelerated toward the field-free flight tube by a positive voltage on the sample and a negative voltage on the TOF extractor.

An attempt was made to observe vibrationally excited water molecules by REMPI at 251.8-253.8 nm, where the H_2O(C-X) $\Delta v_2 = -1$ transitions occur.[55] OH^+ and H^+ signals were much stronger than H_2O^+ signals in this wavelength range, in part due to predissociation of the C(010) state. This intermediate state is known to dissociate to form neutral OH and H fragments, and these neutral fragments can be ionized via non-resonant ionization using the same laser pulse. However, this process requires at least four photons with no resonant steps. Although the lack of significant water signal between 251.8 and 253.8 nm can be explained by predissociation, the strong OH^+ and H^+ signals may also be due to single-photon-induced dissociation of vibrationally excited H_2O^+. This parent ion can be produced by 2 + 1 REMPI of the ground state or by single-photon ionization of an electronic excited state. Equations (3.1) and (3.2) show how an excited water molecule can become ionized and then dissociated by the absorption of subsequent photons.[55]

$$H_2O\ (C, v^*) + h\nu \rightarrow H_2O^+\ (X, v^*) \tag{3.1}$$

$$H_2O^+\ (X, v^*) + h\nu \rightarrow H^+ + OH$$

$$\rightarrow H + OH^+ \tag{3.2}$$

Because the molecule does not fragment until absorbing additional photons in the detection region, TOF measurements of the fragment ions actually probe the velocities of the parent molecules. Any additional energy imparted to H^+ or OH^+ by the fragmentation process is negligible compared to the energy gained during acceleration into the flight tube. TOF spectra for H^+ and OH^+ were obtained at 253.0 nm with a distance of 3 ± 0.5 mm between the surface and the detection region. Since these fragment ions arise from H_2O (v^*) molecules, these measurements allow the H_2O (v^*) velocity distribution to be determined.

3.2.2 Simulation of TOF spectra

Simulation of TOF spectra was accomplished using the flux-weighted Maxwell-Boltzmann distribution, which is appropriate for photodesorption of chemisorbed species.[56] A simple fit of the TOF spectrum, $S(t, T_{trans})$ was slightly narrower than the data:

$$S(t, T_{trans}) = At^{-4}\exp\left(\frac{-mr^2}{2k_B T_{trans} t^2}\right), \tag{3.3}$$

where T_{trans} is the translational temperature, r is the distance between the surface and the detection volume, and A is a scaling factor. Following the work of Hama et al.,[57] we integrated over the entire irradiated area ($0 \leq R \leq R_{max}$), where R_{max} is the radius of the desorption laser spot, the spot is approximated as a circle, and $2\pi R\, dR$ is the infinitesimal area. Fitting curves of appropriate width were obtained by using the following equation at each desired flight time (t):

$$S(R_{max}, t, T_{trans}) = \int_0^{R_{max}} \frac{\pi r R}{t^4}\left(\frac{m}{k_B T_{trans}}\right)^2 \sqrt{r^2 + R^2}\, \exp\left(\frac{-m(r^2+R^2)}{2k_B T_{trans} t^2}\right) dR, \tag{3.4}$$

as shown in Figure 3.3a, where all fitting curves used r = 2 mm. However, this method of fitting the data was not supported by experiments with varying desorption laser spot sizes. An iris was inserted into the desorption beam path to change the radius of the irradiated area, which should correspond to R_{max} in Equation (3.4), and nearly identical spectra were produced with different iris opening radii, R(iris). Figure 3.3a shows that TOF spectra obtained at R(iris) = 1, 2, and 3 mm were all fit best with R_{max} ~ 4 mm in Equation (3.4). Figure 3.3b displays those three TOF spectra scaled to the same amplitude so that their similarities can be better appreciated. Clearly, changing R(iris) from 3 mm to 1 mm did not alter the width of the TOF spectrum, as it should have

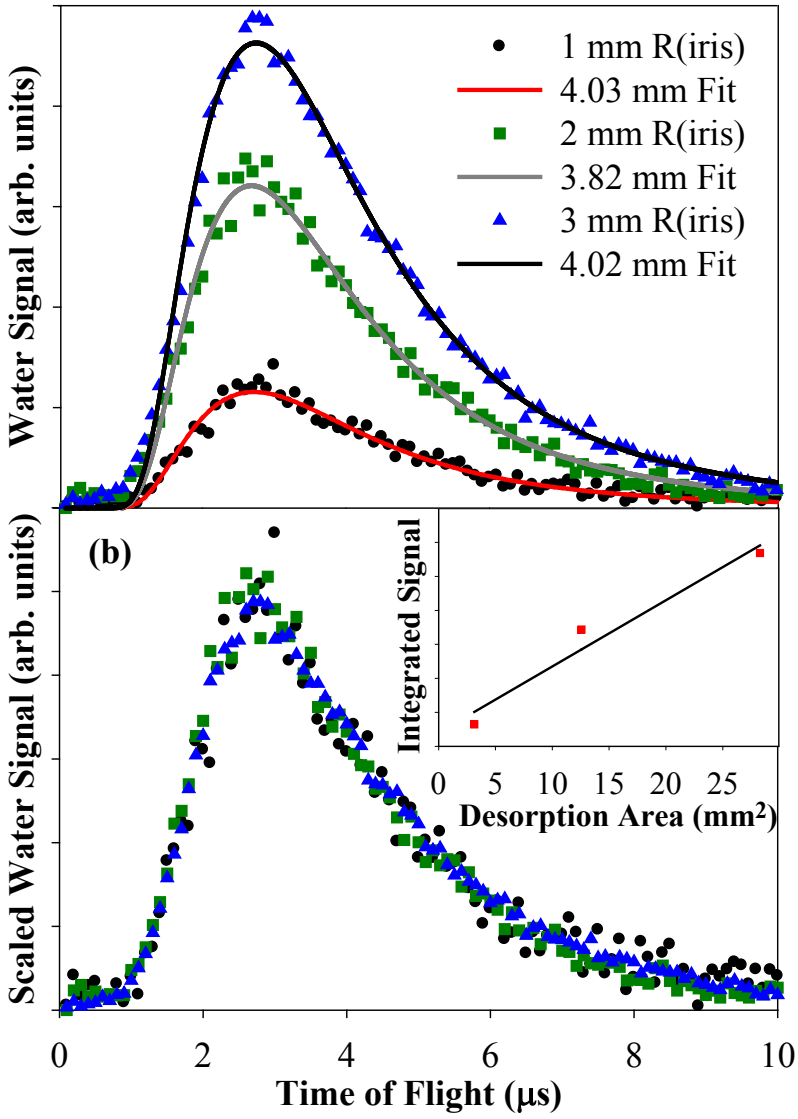

Figure 3.3. TOF spectra of H_2O desorbed from ASW by 157-nm photons with three different desorption laser spot sizes. The desorption laser beam passed through an iris opening with a radius of 1 mm (black circles), 2 mm (green squares), and 3 mm (blue triangles). The fits in (a) were calculated using Equation (3.4) with r = 2 mm, T_{trans} = 625 ± 5 K, and R_{max} ~ 4 mm (exact values in legend). In (b), the TOF spectra were scaled and overlaid to emphasize their indistinguishable shapes. The inset shows a nearly linear relationship between integrated water signal (from 0 to 10 μs) and desorption laser spot area.

according to Equation (3.4). In fact, the only difference between these spectra was multiplication by a scaling factor that increased nearly linearly with increasing irradiation area (inset of Figure 3.3b).

Although decreasing the spot size was predicted to narrow the TOF spectrum, experiments did not reveal any change in width, possibly because the ionization volume was very small (10 μm^3) compared to the desorption areas tested. However, increasing the spot size significantly increased the number of detected water molecules, so there must have been some contribution from the outer parts of the desorption spot. In the simple model that led to Equation (3.4), only those trajectories that led in a straight line from the surface to the detection region were considered. In reality, water molecules desorbing from ASW have a wide range of take-off angles, and collisions between desorbing molecules are possible. Such collisions would broaden the TOF spectrum. In addition, the photodesorption event was not merely a statistical process that would necessarily follow Maxwell-Boltzmann statistics. However, Maxwell-Boltzmann distributions are often useful in empirical fitting to elucidate the various dissociation or desorption channels that contribute to the total observed yield.[56]

In this case, a single desorption channel was indicated even though the TOF spectrum was slightly broader than a Maxwell-Boltzmann distribution. Therefore, the peak of the TOF spectrum was fit using Equation (3.3). TOF data were also collected at multiple values of r and plotted in velocity space using the Jacobian transform, $P_v(v) = tr^2S(t)$, where $v = r/t$ and $S(t)$ is the measured signal intensity at each time.

3.2.3 Simulation of 2 + 1 REMPI spectra

The 2 + 1 REMPI spectrum of H_2O was simulated with PGOPHER, a freely available program for simulating rotational spectra.[58] Rotational constants of the ground and C states were taken from Yang and Skinner,[59] who used their own velocity map imaging REMPI data as well as experimental data available from the JPL spectral line catalog[60] to modify constants from Johns.[61] The nuclear spin temperature was set to 300 K, which gives an ortho:para ratio of 3:1, the statistical distribution expected at temperatures above 65 K.[62]

3.3 Results

3.3.1 2 + 1 REMPI spectrum for H_2O (v = 0)

The 2 + 1 REMPI spectrum of desorbed water exhibited rotational excitation, with a rotational temperature of 425 ± 75 K. In Figure 3.4, the peak positions and relative intensities in the REMPI spectrum of desorbed H_2O nearly match a simulated spectrum using a rotational temperature of 425 K. The experimental peaks are slightly broader than the calculated peaks, most likely due to power broadening. The fitting parameters were not guaranteed to be accurate for rotational temperatures above 300 K due to the large number of transitions and overlapping peaks. This uncertainty at high rotational temperatures may contribute to the fact that simulated spectra over quite a large range (350-500 K) fit the data, which have a considerable amount of noise due to fluctuations in both desorption and ionization laser powers. For the same experimental conditions, the rotational temperature reported by Hama et al.[57] was 350 ± 150 K, so the results are consistent within error.

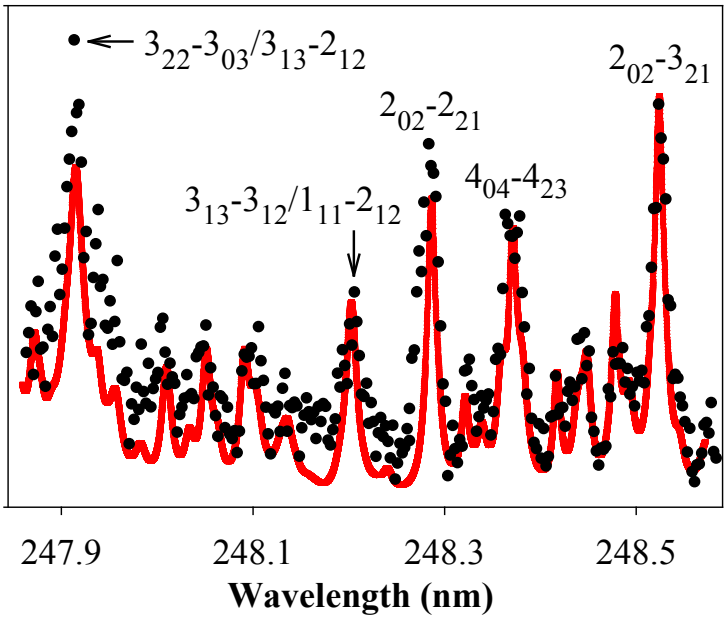

Figure 3.4. Experimental 2 + 1 REMPI spectrum of H_2O desorbed from ASW by 157-nm photons at 108 K, measured at 2.8-μs delay (dots) and simulated two-photon C-X spectrum with a rotational temperature of 425 K and an ortho:para ratio of 3:1 (line). The rotational transitions associated with the five largest peaks are shown.

3.3.2 TOF spectra and velocity distributions

The shape of the TOF spectrum was found to be remarkably robust with respect to changes in coverage, desorption laser flux, ionization energy, desorption laser spot size, ice morphology (ASW vs. CI), and rotational state sampled. While the amount of detected water was affected by varying each of these parameters, the TOF spectra were all indistinguishable after multiplication by a scaling factor. The distribution calculated with Equation (3.3), using r = 3.1 mm and T_{trans} = 700 K, is shown to fit the peak of the TOF spectrum in Figure 3.5. The uncertainty in intensity is shown with 95% confidence intervals. The distance from the sample to the detection region, r, was not easily measured. However, based on the method of laser alignment, r for this experiment was

determined to be 3.1 ± 0.5 mm, which corresponds to T_{trans} = 700 ± 200 K (0.12 ± 0.03 eV), as both r and T_{trans} primarily affect the simulated distribution by shifting it horizontally.

As mentioned in Section 3.1, Hama et al.[57] reported T_{trans} = 1800 ± 500 K for roughly the same experimental conditions. Their experimental data were very similar to the data shown in Figure 3.5, except for a horizontal shift because their value of r was 2 mm. However, because their data were fit using the method examined in Figure 3.3 (with R_{max} = 6 mm), the reported translational temperature of 1800 K may be an overestimate.

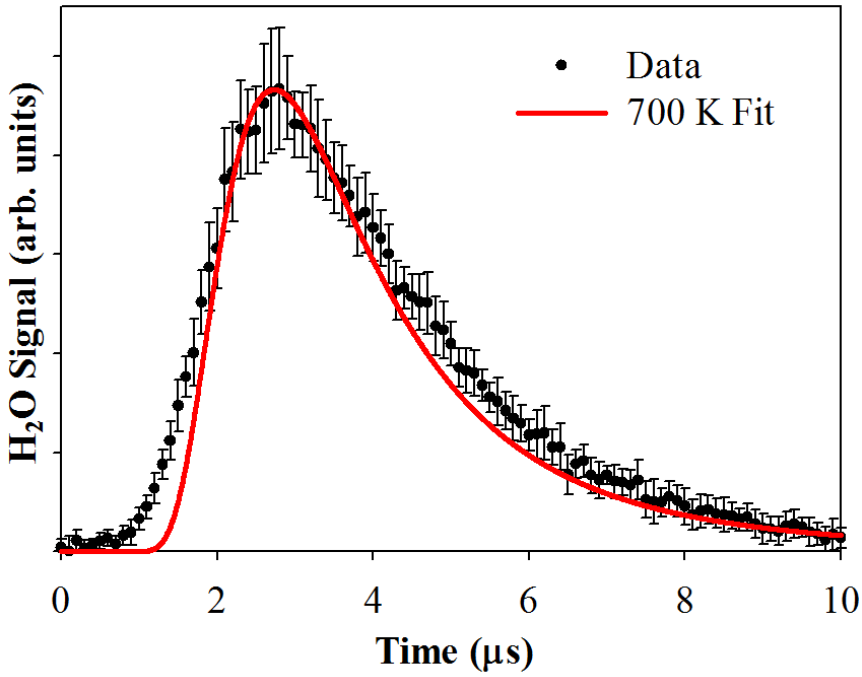

Figure 3.5. TOF spectrum of H_2O desorbed from ASW at 108 K by 157-nm photons and detected by 2 + 1 REMPI on the 2_{02}-3_{21} rotational peak at 248.52 nm. The solid red line is a Maxwell-Boltzmann distribution with r = 3.1 mm and T_{trans} = 700 K.

The focal point of the ionization laser was moved to several different distances from the sample, and TOF data were collected at these multiple values of r. As expected,

the TOF spectra shifted to lower time and narrowed as *r* decreased. The velocity distribution, shown in Figure 3.6, was consistent between data sets. Although the precise values of *r* shown in Figure 3.6 were chosen to show the best possible overlap between data sets, the distances and uncertainties obtained by careful laser alignment were really 2.0 ± 0.5 mm, 2.5 ± 0.5 mm, and 3.1 ± 0.5 mm. Maximum signal corresponded to a velocity of ~950 m/s.

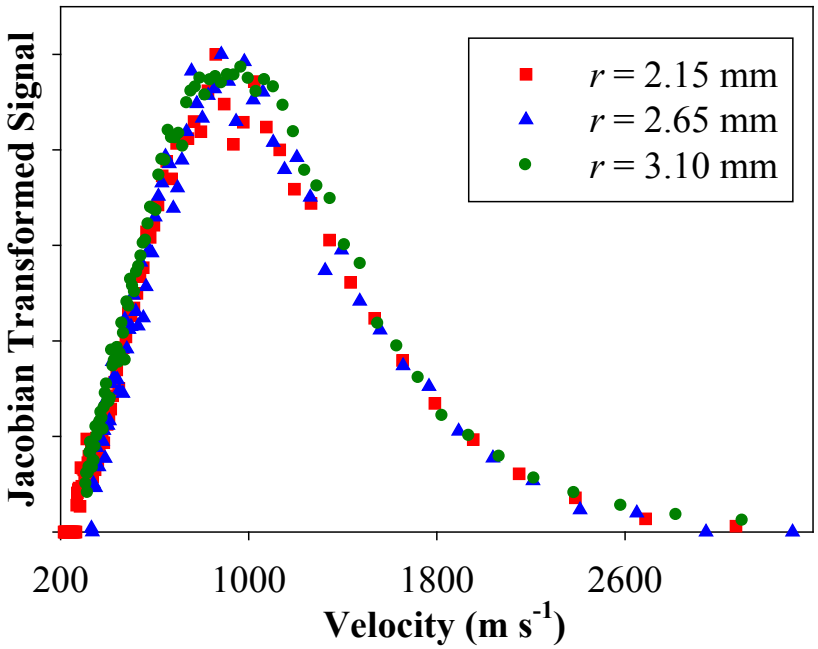

Figure 3.6. Velocity distribution of H_2O desorbed from ASW at 108 K by 157-nm photons and detected by 2 + 1 REMPI on the 2_{02}-3_{21} rotational peak at 248.52 nm. Three different distances between sample and detection region yielded consistent results.

Desorption signal was found to be linear with respect to desorption laser flux. Figure 3.7 shows integrated water signal from 2.3 to 3.9 μs as a function of energy per pulse with *r* = 3.1 mm. The two different data sets were obtained with slightly different

ionization energies, but both clearly show a linear dependence of signal on energy, so a single-photon mechanism of desorption is indicated.

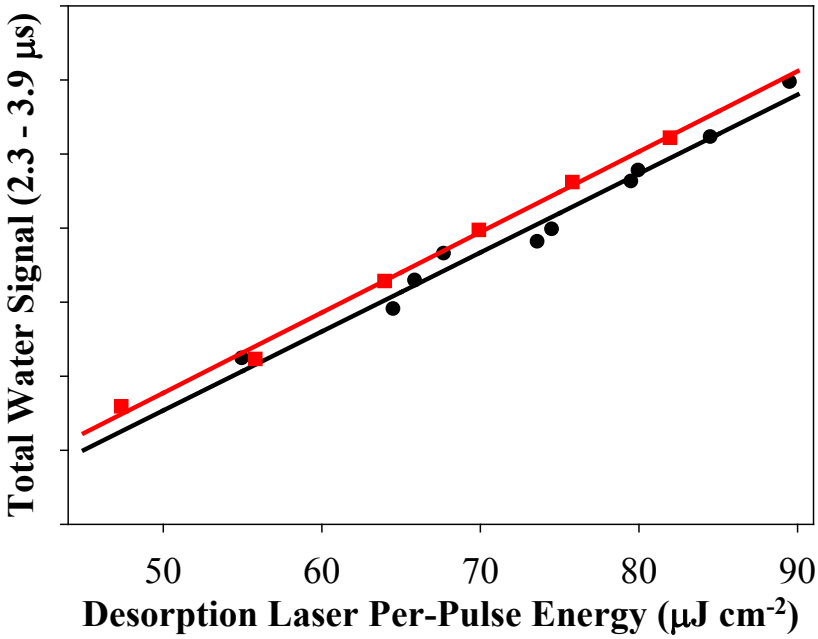

Figure 3.7. Water signal detected by 2 + 1 REMPI on the 2_{02}-3_{21} rotational peak integrated from 2.3 to 3.9 μs delay time as a function of energy per pulse. The two sets of data were obtained with slightly different ionization energies. The solid lines are linear regressions.

Signal per pulse, measured at the TOF distribution peak, was not found to require an incubation period. Within the first 32 desorption laser pulses, water signal was already maximized. Due to fluctuations in laser powers, at least 32 shots had to be averaged to obtain reproducible results. Signal also remained approximately constant after long irradiation times for initial coverages ≥ 100 L.

3.3.3 Cross sections for water removal

Water removal cross sections were measured at 1, 5, 10, 20 and 30 L exposures. With r = 2 mm, water signals at 1.1 and 2.3 μs delays were averaged over 64, 128, or 256 laser pulses by an oscilloscope, and data were collected for a total of ~100,000 pulses. These delay times were chosen to probe the faster and slower parts of the TOF spectrum. However, no significant differences in cross section were found between the cross sections at 1.1 and 2.3 μs. This result supports the idea that a single mechanism is responsible for H_2O photodesorption. Figure 3.8 shows two examples of the cross section measurement. The slowly decreasing water signals were fit with exponentials of the form $y = Ae^{-\sigma x}$, where x is the number of photons per cm^2 and σ is the cross section.

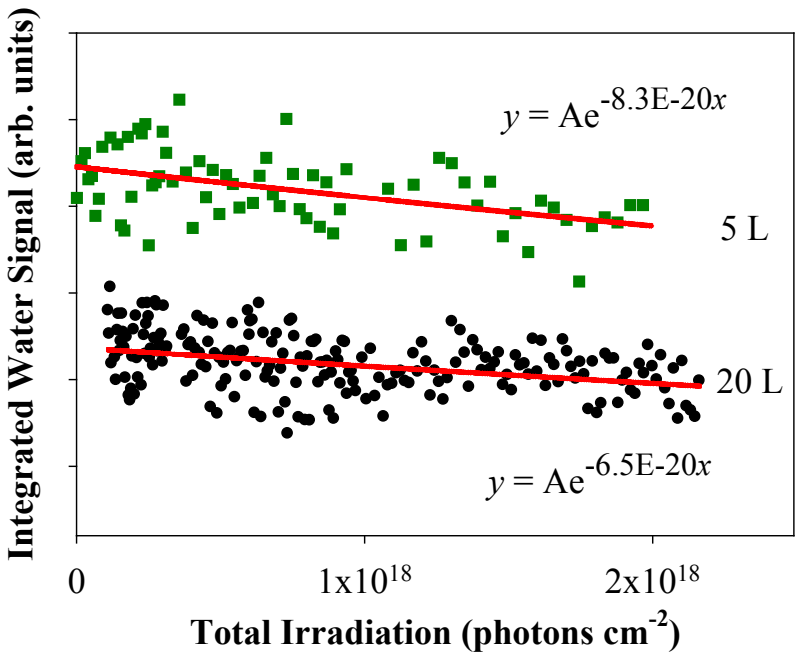

Figure 3.8. Representative cross section measurements for H_2O removal from 5 and 20 L ASW by 157-nm irradiation. 5 L data and exponential fitting curve were offset for clarity. The number of 157-nm photons was calculated using the pulse counter on the excimer laser display and an average energy of 55 μJ cm^{-2} per pulse.

Although only specific rovibrational states of photodesorbed water were detected, the observed decrease in signal was caused by surface water depletion in all forms: photodesorption of H_2O ($v = 0$), photodesorption of H_2O (v^*), and photodissociation. Multiplying all water signals by a constant did not affect the calculated cross sections; only the relative decrease in signal over irradiation time was important. Assuming that measured signal was proportional to the number of water molecules at the surface, the reported cross sections were characteristic of water removal as a whole.

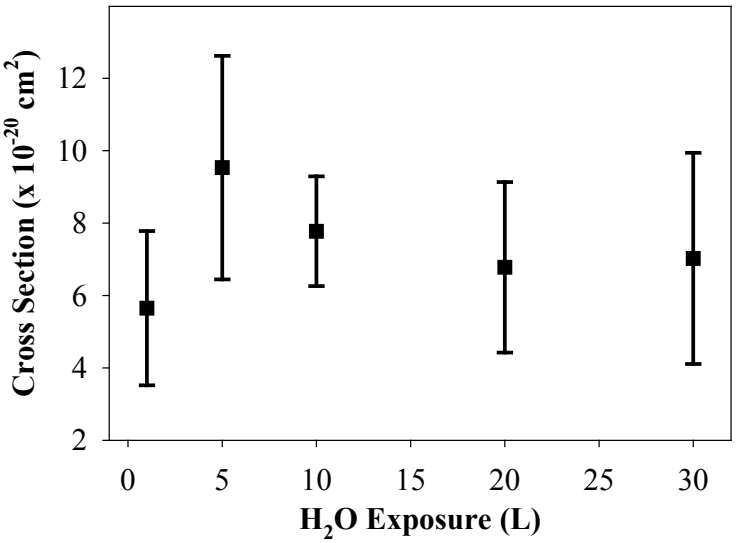

Figure 3.9. Average cross sections for H_2O removal from 1-30 L ASW by 157-nm irradiation. Error bars represent 95% confidence intervals based on 4-6 different measurements at each exposure.

Four to six cross section measurements were performed at each exposure, and the results are summarized in Figure 3.9. For 20-30 L exposure, the average cross section was $(6.9 \pm 1.8) \times 10^{-20}$ cm^2. Although no statistically significant differences were found between cross sections at different exposures, 1 L exposure tended to result in lower

cross sections, while 5 L exposure tended to result in higher cross sections. These trends are expected based on how water sticks to surfaces in clusters at low exposures, with maximum surface roughness around 5 L. When an attempt was made to determine the cross section at 100 L, water signal did not decrease during irradiation with 2×10^{18} photons cm^{-2}.

3.3.4 Photofragments from vibrationally excited water

The TOF spectra of OH^+ and H^+ fragment ions from vibrationally excited water molecules are shown in Figure 3.10. The translational temperatures associated with the best fitting Maxwell-Boltzmann distributions were found to be 1400 ± 450 K for OH^+ and 1200 ± 400 K for H^+, though these temperatures should be identical according to the theory in Section 3.2.1. The H^+ peak was obscured by ringing from the excimer laser for the first 1 μs, so those early data points are omitted for H^+. Another complication with detecting H^+ fragments was the large H^+ signal due only to the ionization laser. Although the two H^+ peaks were slightly separated in time, some overlap did occur. Thus, only the OH^+ TOF spectrum was used to determine the parent molecule energies. The distance between the surface and the detection region was 3.0 ± 0.5 mm, and this uncertainty in distance led to uncertainty in the translational energies of vibrationally excited parent water molecules. Based on the OH^+ data, the parent water molecules have translational energies centered around 0.24 ± 0.08 eV. Therefore, the translational energy of $H_2O(v^*)$ is greater than that of $H_2O(v = 0)$ when desorbed from ASW at 108 K by 157-nm irradiation.

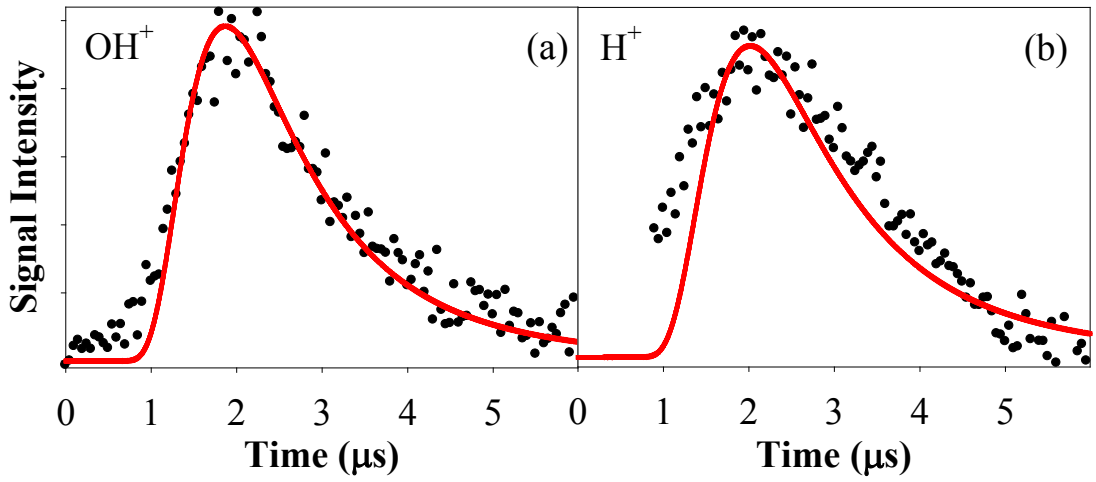

Figure 3.10. TOF spectra of (a) OH^+ and (b) H^+ fragment ions from vibrationally excited H_2O molecules desorbed by 157-nm photons, ionized and fragmented by 253-nm photons. A Maxwell-Boltzmann distribution with T_{trans} = 1400 K fits the OH^+ data, and a distribution with T_{trans} = 1200 K fits the peak of the H^+ spectrum.

The effect of increasing the irradiation fluence on the vibrationally excited water yield was determined by measuring OH^+ signal at flight times of 0.9 μs and 3.4 μs. For the desorption energies (50-90 μJ cm^{-2} per pulse) and ionization energies (4.5-5.0 mJ per pulse) used here, there was no difference other than scale between signal at the two flight times, so a single Maxwell-Boltzmann distribution was used to fit the data. Both appeared promptly, rose slowly at a linear rate, and increased by about 18% in the first ten minutes of irradiation. In a nearly identical experiment, Andersson et al.[55] found that the fast and slow signals behaved differently with increasing irradiation, so they reported a fast component with T_{trans} = 10,000 ± 2000 K and a slow component at 1800 ± 300 K. While our results match their slow component (within error), we did not detect a fast component. However, our results do not exclude the possibility of two convoluted components with similar translational temperatures. The addition of one component that

does not depend on irradiation time and another that increases with irradiation time could lead to the observed signal.

3.4 Discussion

3.4.1 H_2O photodesorption mechanisms

There are several possible mechanisms for H_2O desorption following 157-nm irradiation of ASW. These mechanisms include recombinative desorption of photoproducts from different water molecules, geminate recombinative desorption of photoproducts from the same water molecule, the dipole-reversal mechanism involving a delocalized exciton, and the kick-out mechanism involving an energetic hydrogen atom. Because the TOF spectrum in Figure 3.5 only requires one Maxwell-Boltzmann distribution for a good fit, one mechanism is likely responsible for the observed H_2O ($v = 0$) signal.

Andersson et al.[55] used molecular dynamics simulations, in which only the excited water molecule was not rigid, to calculate $T_{trans} = 1450 \pm 150$ K for the kick-out mechanism and $T_{trans} = 2000 \pm 200$ K for geminate recombinative desorption. The products of geminate recombinative desorption exhibited significant vibrational excitation as well, but the kicked out molecules were not allowed to vibrate in these simulations. As shown in Figure 3.5, T_{trans} for H_2O ($v = 0$) is only 700 ± 200 K, so neither mechanism is supported by these data. Like geminate recombination, recombination of photoproducts from different water molecules is expected to produce mostly vibrationally excited water. In addition, signal from this recombination mechanism should initially increase with irradiation time, so it is not responsible for the H_2O ($v = 0$) signal, which only decreases in intensity with irradiation time. The only other mechanism from the list

of possibilities is dipole reversal, which has not received much theoretical treatment previously.

In order to elucidate the dipole-reversal mechanism for photodesorption of a water molecule from the surface of ice, electron attachment and detachment densities of excited ice clusters were calculated by our collaborators (Crowell and Sherrill) at the CIS/aug-cc-pVDZ level of theory. These calculations included the effect of the bulk ice using mixed quantum mechanics/molecular mechanics (QM/MM) methods.[2] The tetramer in Figure 3.11 was extracted from a model of hexagonal ice, with the central water corresponding to one of the water molecules on the surface. This surface water molecule receives two hydrogen bonds and donates one.

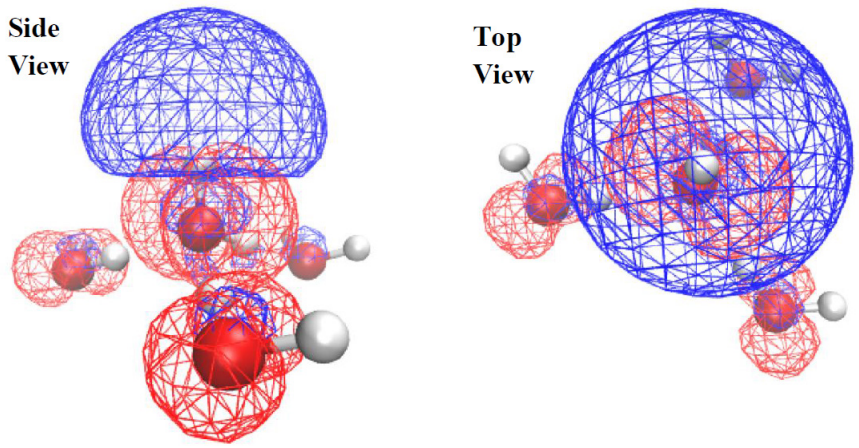

Figure 3.11. Electron attachment/detachment densities of the first excited state of the tetramer in the QM/MM model system (CIS/aug-cc-pVDZ). Blue represents electron attachment density, while red represents a region of depleted electron density.

As in the first singlet excited state of the gas-phase water monomer, most of the electron detachment comes from the p-orbital of the surface water oxygen, although the oxygen p-orbitals of surrounding waters also contribute. However, unlike in the water

monomer, the attachment density is placed outside of the hydrogen pointing away from the surface. This dipole reversal results in unfavorable electrostatic interactions between the surface water and its neighbors, specifically between the central oxygen and its former hydrogen-bonding partners. While the central oxygen is not quite electropositive, its atomic charge is close to zero. Thus, the excited state charge distribution seems to create an unfavorable interaction that could lead to ejection of the surface water molecule.

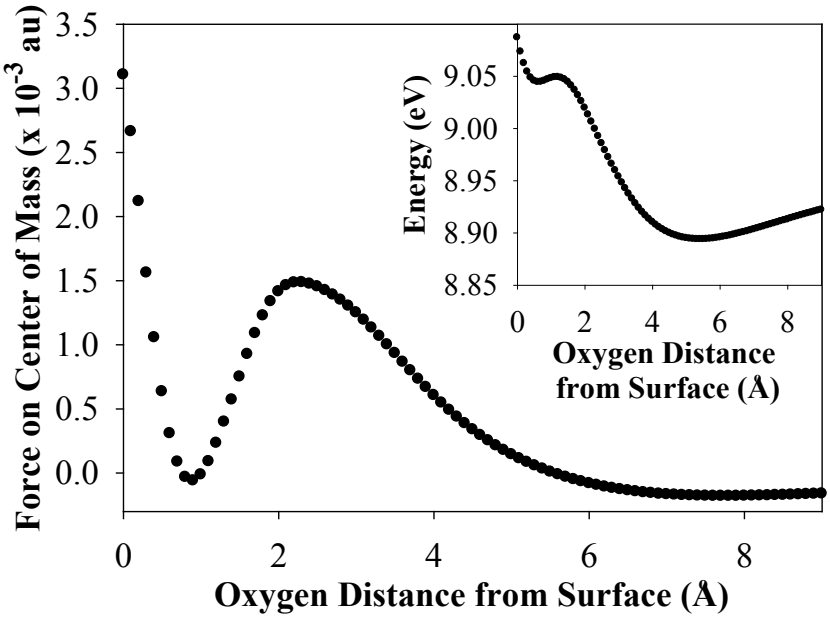

Figure 3.12. Force and energy (inset) plots constructed for the first singlet excited state potential of the QM/MM model at the CIS/aug-cc-pVDZ level of theory.

To estimate an upper-bound for the velocity of a desorbing water molecule, Crowell and Sherrill also constructed force and energy plots for the first singlet excited state potential of the QM/MM model at the CIS/aug-cc-pVDZ level of theory.[2] The central water of the quantum mechanical tetramer was pulled rigidly away from the

surface, and the force on each atom was calculated at 0.1-Å intervals. The force on the central water's center of mass is plotted versus distance from the surface in Figure 3.12. The force plot was integrated to obtain a potential of 0.202 eV, which can be interpreted as an upper bound to the energy of a desorbing water molecule. The corresponding potential curve is shown in the inset to Figure 3.12. Alternatively, Crowell also computed the difference in energies between the excited cluster at equilibrium and the excited cluster with the central water 100 Å from the surface, with a result of 0.144 eV.[2] This value can also be considered an upper bound to the energy of a desorbing water molecule. However, the true upper bound could be higher in energy due to the limitations of the CIS/aug-cc-pVDZ level of theory.

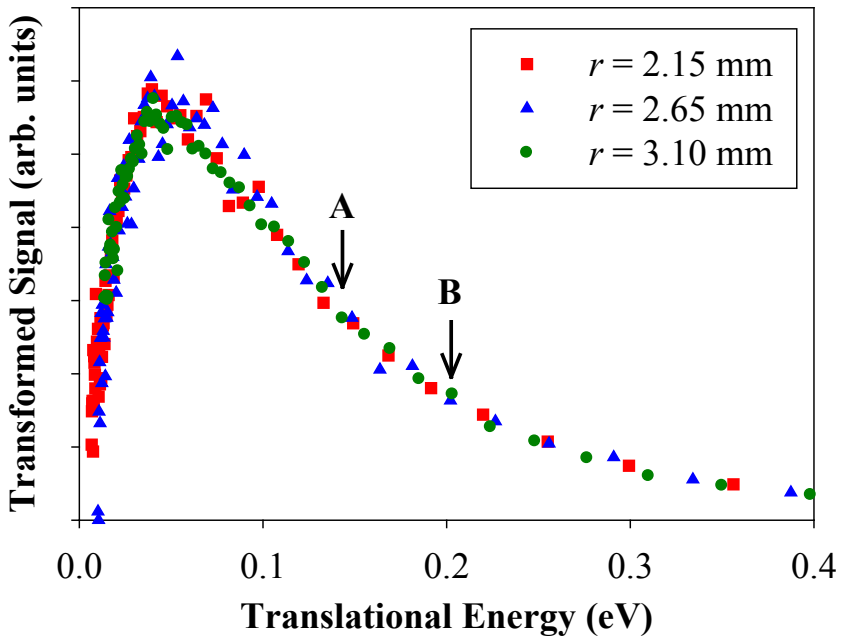

Figure 3.13. Translational energy distribution of H_2O desorbed from ASW at 108 K by 157-nm photons and detected by 2 + 1 REMPI at three different distances between the sample and the detection region. Upper bounds estimated at the CIS/aug-cc-pVDZ level of theory are shown at A (0.144 eV) and B (0.202 eV).

The desorption curves in Figure 3.12 show that first excited state should lead to desorption, although a local minimum in the force curve indicates that the desorbing molecule may be slowed by interactions with the bulk. The estimated upper bounds obtained from those curves are shown in Figure 3.13, which contains the experimental data from Figure 3.6 plotted as a function of translational energy. Most of the experimentally observed desorbing water molecules have less translational energy than both computed upper bounds, which are indicated in Figure 3.13 by arrows at 0.144 eV (A) and 0.202 eV (B).

Photodesorption of H_2O (v*) may also be due in part to the dipole-reversal mechanism. Although the translational energy of H_2O (v*) is approximately twice that of H_2O ($v = 0$), the same mechanism could be responsible for both. Unlike in unimolecular decay, energy conservation in the condensed phase involves neighboring molecules. After excitation, water molecules with relatively long lifetimes on the surface can lose both vibrational and translational energy to surrounding molecules, while those that desorb more quickly can retain both forms of energy. Indeed, water molecules that desorb as a result of an exciton-mediated process are expected to exhibit vibrational excitation.[57]

As mentioned in Section 3.3.4, there may be more than one mechanism responsible for desorbing H_2O (v*). Since T_{trans} for H_2O (v*) is 1400 ± 450 K, the kick-out mechanism (calculated T_{trans} = 1450 K for rigid H_2O) might be responsible for desorption of vibrationally excited water. Unfortunately, because the kicked out water molecules in the simulations of Andersson et al.[55] were not allowed to vibrate, the translational temperature of H_2O (v*) desorbing due to the kick-out mechanism has not

been specifically calculated. Still, the kick-out mechanism cannot be ruled out as a mechanism for producing H_2O (v*).

Recombinative desorption of photofragments from different water molecules may also be responsible for desorption of vibrationally exited H_2O. A mechanism involving the build-up of hydroxyl groups on the surface would help to explain why signal indicative of H_2O (v*) increases with irradiation time. As photodissociation occurs, more OH radicals become available for recombination: OH + OH → H_2O + O. The irradiation time dependence results can be explained if both recombinative desorption and one of the direct mechanisms of desorption lead to translational temperatures near 1400 K.

3.4.2 Water removal cross section

In the present cross section experiments, only H_2O (v = 0) molecules are detected, but the calculated cross sections are characteristic of total water removal from the ice surface. With increasing irradiation, H_2O (v = 0) signal declines due to the decreasing number of surface water molecules, which are removed through both photodesorption and photodissociation. According to Oberg et al.,[44] at 100 K, 64% of water loss is attributed to intact desorption, while the rest is attributed to dissociation. The average cross section observed for 20-30 L exposure was $(6.9 \pm 1.8) \times 10^{-20}$ cm^2, so the cross section of intact H_2O desorption would be approximately $(4.4 \pm 1.2) \times 10^{-20}$ cm^2. However, Oberg et al.[44] used a hydrogen discharge lamp with up to 10.5-eV photons, so it is probable that an even greater ratio of desorption relative to dissociation occurs with only 7.9-eV photons. A more extensive discussion of the wavelength dependence follows later in this section.

The lowest cross section observed in these experiments, 5.7×10^{-20} cm^2 for 1 L exposure, is slightly higher than the 2.3×10^{-20} cm^2 cross section from 6.4-eV irradiation of 0.6 ML H_2O on p(2x2)O/Pd(111).[63] Higher coverage and photon energy are responsible for making our cross sections higher.

The water desorption cross section that most astrophysical models use, 8×10^{-18} cm^2, was determined for Lyman-α photons (10.2 eV) using a microbalance to measure total ice removal from the surface.[45] This value is two orders of magnitude larger than the cross section obtained in the present experiments. Quadrupole detection of D_2 from D_2O ice at 126 nm led to an estimate of 9×10^{-18} cm^2 for the cross section of ice destruction, which includes desorption, dissociation, and ionization.[64] Because it includes ionization, the ice destruction cross section should be much larger than the water removal cross section. Therefore, the water removal cross section at 10.2 eV may actually be much lower than the estimate of Westley et al.[45] Even if the true value is significantly lower than 8×10^{-18} cm^2, the water removal cross section at 7.9 eV (6.9×10^{-20} cm^2) will likely provide a lower limit.

The most important difference between these two experiments is the wavelength of photons used. The absorption coefficient at 10.2 eV is approximately twice the value at 7.9 eV for amorphous ice.[12] If the same mechanisms were dominant at 10.2 eV and 7.9 eV, the cross section would only be expected to be twice as large at 10.2 eV. However, additional mechanisms of ice removal could be responsible for making the cross section at 10.2 eV so large. The photoelectric threshold of ASW is 8.7 eV, and the photoelectric yield at 10 eV is ~ 10^{-3} per photon.[65] Therefore, photoionization of water plays a significant role in ice removal at 10.2 eV, while it is negligible at 7.9 eV. Once H_2O^+ is

formed, it can react and recombine with electrons to form an excited state similar to the dipole reversal state described in Section 3.4.1. This excited state could lead to desorption or decay to form other species.[66]

An extensive study of the H_2O photodesorption yield using a hydrogen discharge lamp (7-10.5 eV) obtained a yield of 4.5 x 10^{-3} molecules photon^{-1} for exposures greater than 8 L at 100 K,[44] which is close to the corresponding yield from Westley et al. of 7.5 x 10^{-3} molecules photon^{-1}.[45] These similar results led Oberg et al. to hypothesize that the photodesorption yield would not be affected by different lamp spectral energy distributions.[44] While all hydrogen discharge lamps may give similar yields due to their common high-energy photons, the wavelength of the irradiation source does make an enormous difference. The yield has not been determined from the present experiments because the relationship between water signal and thickness is unknown. However, for 1 L exposure, clusters are likely to form. Under these conditions, the maximum coverage is assumed to be 10^{14} molecules. Assuming that signal is proportional to coverage, an estimate of the yield is 1.8 x 10^{-4} molecules photon^{-1}. Therefore, our estimated yield is about one order of magnitude below the corresponding yield from Oberg et al., 1.3 x 10^{-3} molecules photon^{-1}.[44]

3.4.3 Astrophysical implications

Clearly, cross section and yield are greatly influenced by the UV wavelength and flux. The interstellar UV field is often simulated with a hydrogen discharge lamp since the Lyman-α flux is dominant. However, many regions within our solar system are not dominated by the Lyman-α flux. Calculations intended to model a specific location in

space should obviously use the cross sections specific to the prevailing UV wavelengths in the area. In addition, though not explicitly shown in this study, the ice surface temperature can play a large role in determining cross sections for dissociation and desorption, mainly due to increases in excited state lifetimes as increasing temperature reduces coupling between neighbors.[7, 67]

As an example, the cross sections presented in this paper apply to the rings of Saturn, which are comprised of icy grains with temperatures near 100 K. The solar photon flux below 230 nm near Saturn is 3.5×10^{11} photons cm^{-2} s^{-1}.[68] In the previous section, we stated that the cross section of intact H_2O desorption would be approximately 4.4×10^{-20} cm^2, assuming that 64% of our measured cross section is due to intact desorption and that the remainder is due to dissociation. We can then calculate a rate of desorption by multiplying the photon flux by the cross section and the number of molecules on the surface of a grain. For a grain with a radius of 1 cm, the result is 4.8×10^7 molecules s^{-1}. Using the value from Westley et al.[45] would instead give a rate of 8.8×10^9 molecules s^{-1}, but this rate would include dissociation and ionization in addition to intact desorption. Since the solar photon flux below 230 nm includes more photons above 7.9 eV than below, our calculated rate of 4.8×10^7 molecules s^{-1} for intact H_2O desorption from a 1-cm grain should be treated as a lower bound.

3.5 Conclusion

The photodesorption of water molecules from amorphous solid water by 157-nm irradiation has been examined using resonance-enhanced multiphoton ionization. The rotational temperature has been determined, by comparison with simulations, to be 425 ±

75 K. The TOF spectrum of H_2O ($v = 0$) has been fit with a Maxwell-Boltzmann distribution with a translational temperature of 700 ± 200 K (0.12 ± 0.03 eV). H^+ and OH^+ fragment ions have been detected with non-resonant multiphoton ionization, indicating vibrationally excited parent water molecules with translational energies of 0.24 ± 0.08 eV. The cross section for water removal by 7.9-eV photons near 100 K was determined to be (6.9 ± 1.8) x 10^{-20} cm^2 for > 10 L H_2O exposure. Electronic structure computations have also probed the excited states of water and the mechanisms of desorption. Calculated electron attachment and detachment densities show that exciton delocalization leads to a dipole reversal state in the first singlet excited state of a model system of water ice.

CHAPTER 4

H_2O PHOTODESORPTION FROM AMORPHOUS SOLID WATER ON GENUINE LUNAR SURFACES

4.1 Introduction

For several decades after the Apollo missions, the Moon was thought to be completely anhydrous. In recent years, however, water has been discovered in permanently shadowed regions of the Moon,[24] in lunar volcanic glasses,[69] in lunar melt inclusions,[70] and in anorthosites from the lunar magma ocean.[71] Certain locations on the Moon seem to contain water with hydrogen isotope ratios similar to those found in comets, and it has been proposed that cometary water was delivered to the Moon shortly after it was formed.[72] While it is possible that most of the Moon contained water in its distant past, the only evidence for water on the sunlit surface of the Moon today is infrared absorption near 3 μm,[23] which could be due merely to hydroxyl groups.[26] Two of the primary causes of water depletion on the Moon's surface are photodesorption and photodissociation by solar photons.

Ultraviolet photons in the solar flux are able to excite H_2O to its first excited state, which is dissociative for an isolated water molecule. In the condensed phase, the first excited state becomes a band of $1b_1 \rightarrow 4a_1$ transitions with ~7-9.5 eV,[12] and coupling to neighboring water molecules opens a pathway to intact desorption.[9] However, significant dissociation still occurs when ASW experiences irradiation, and a competition exists between dissociation and exciton delocalization, which facilitates desorption.[73] Both desorption and dissociation from 157-nm irradiation of ASW have been studied

experimentally,[55, 57, 74] but these previous studies probed extremely thick ASW and did not involve the substrate at all.

In the present study, we investigate water desorption mechanisms and measure the water removal cross sections for 157-nm irradiation of thin ASW layers on two genuine lunar surfaces. In Chapter 3, velocity distributions were reported that support the dipole reversal mechanism for desorption of H_2O from thick ASW. Additionally, kick-out by a hot hydrogen atom and recombination mechanisms were considered for the formation of vibrationally excited water molecules. The present work aims to determine whether the same mechanisms are in effect for thin ASW layers on genuine lunar surfaces. H_2O has been desorbed by 157-nm irradiation from ASW on two lunar substrates and detected by REMPI. Rotational and translational energies of the desorbed water molecules have been determined by comparison with simulations, and cross sections for water removal have been measured for various H_2O exposures.

4.2 Experimental Details

Photodesorption experiments were performed in the same UHV chamber depicted in Figure 3.1. An impact melt breccia collected during Apollo 16 and a mare basalt collected during Apollo 17 were the two lunar substrates. The impact melt breccia was produced by a basin-forming impact that brought mafic material and KREEP (potassium, rare earth elements, and phosphorous) from beneath the crust to the surface and crushed this material into heterogeneous glass.[75] The vesicular mare basalt has large pores because it was formed by the rapid cooling of bubbling magma.[76] Table 4.1 contains the

approximate bulk chemical compositions of the impact melt breccia (NASA sample 60017.196) and mare basalt (NASA sample 70215.368).[77, 78]

Table 4.1. Bulk chemical compositions (% by mass) of impact melt breccia from NASA sample 60017 and mare basalt from NASA sample 70215.

Sample	SiO_2	FeO	TiO_2	CaO	Al_2O_3	MgO	Cr_2O_3	Na_2O	K_2O
Breccia	45.5	3.3	0.2	17.2	30.9	2.4	0	0.03	0.4
Basalt	37.2	19.6	13.1	10.4	8.7	8.5	0.4	0.3	0.04

Compared to JSC-1A, the analog in Chapter 2 that most closely resembles a mare basalt, the genuine mare basalt contains more TiO_2 and less Al_2O_3 (see Table 2.1). Additionally, JSC-1A was a powder, while both genuine lunar samples are solid slabs. Compared to the glassy lunar analog, the substrate in Chapter 2 that most closely resembles the impact melt breccia, the genuine lunar slab contains more Al_2O_3 and CaO but less FeO (see Table 2.1).

One side of each lunar slab was cut smoothly, and this flat side was pressed tightly against the copper sample holder with tantalum strips to make cooling and heating possible. Experiments on the impact melt breccia were performed at 102 K, and experiments on the mare basalt were performed at 88 K due to slightly better cooling. Figure 4.1 shows the impact melt breccia mounted on the copper sample holder and the approximate position of the desorption laser spot. Both lunar slabs were dark in color and appeared porous.

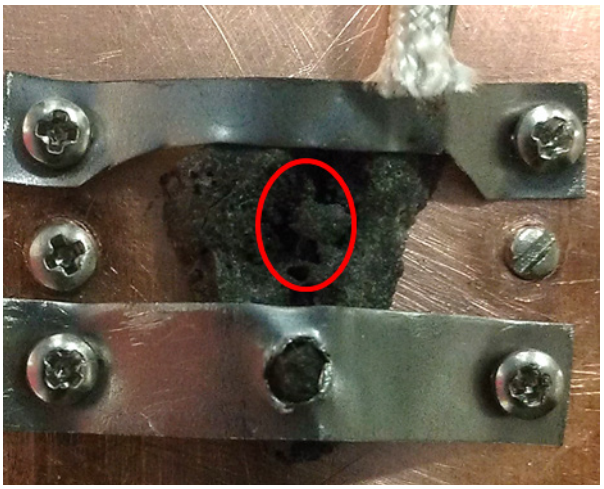

Figure 4.1. Impact melt breccia collected during Apollo 16 mounted on the copper sample holder with tantalum strips. The approximate position of the desorption laser spot is outlined in red. The lunar slab is actually ~ 1 cm on the longest side.

The experimental setup was essentially the same as that shown in Figure 3.2 and described in Section 3.2.1. Unfocused 157-nm light from an excimer laser entered the chamber through a magnesium fluoride window and struck the sample at a 45° angle. Desorption energies were typically 150-350 μJ cm^{-2} per pulse. For low-coverage experiments, background dosing was performed at a water pressure of 1 x 10^{-8} Torr, resulting in 0.1 L for 10 seconds of exposure (1 L = 1 x 10^{-6} Torr·s). For high-coverage experiments, background dosing was performed at 5 x 10^{-8} Torr H_2O, resulting in 30 L for 10 minutes of exposure.

Desorbed water molecules were detected with 2 + 1 REMPI at 247.8-248.6 nm. For the impact melt breccia, the ionization beam was 2 ± 0.5 mm above the surface. For the mare basalt, the ionization beam was 2.5 ± 0.5 mm above the surface. In both cases, the distance between the surface and the detection region was not exactly constant due to

the surface roughness. The time between desorption and ionization was varied from 0 to 10 μs to probe different parts of the desorption plume.

To determine water removal cross sections (σ), water signal was plotted versus number of incident 157-nm photons, and the data were fit with exponential functions of the form $y = Ae^{-\sigma x}$. The number of 157-nm photons was calculated using the pulse counter on the excimer laser display, average excimer power measured before and after the scan, and a correction factor of 0.65 for losses passing through the MgF_2 window.

Detecting vibrationally excited water molecules by REMPI at 251.8-253.8 nm, where the H_2O(C-X) $\Delta v_2 = -1$ transitions occur,[55] was not possible, probably due to predissociation. However, TOF spectra for the fragment ions of vibrationally excited water molecules, H^+ and OH^+, were obtained at 253.0 nm with a distance of 3.5 ± 0.5 mm between the surface and the detection region for the impact melt breccia and a distance of 2.5 ± 0.5 mm for the mare basalt. As described more thoroughly in Section 3.2.1, because the vibrationally excited water molecules do not fragment until absorbing additional photons in the detection region, TOF measurements of the fragment ions actually probe the velocities of the parent molecules. OH^+ signal at the peak of its TOF spectrum was then monitored as a function of irradiation time, and a cross section for H_2O (v^*) removal was calculated, assuming that the entire OH^+ signal was in fact due to H_2O (v^*).

Simulation of TOF spectra involved flux-weighted Maxwell-Boltzmann distributions, which are appropriate for photodesorption of chemisorbed species.[56] The data were fit adequately by the sum of three Maxwell-Boltzmann distributions, $S(t, T_{trans})$, of the form:

$$S(t, T_{trans}) = At^{-4}\exp\left(\frac{-mr^2}{2k_B T_{trans} t^2}\right), \quad (4.1)$$

where T_{trans} is the translational temperature, r is the distance between the surface and the detection region, and A is a scaling factor.

TOF data were also plotted in velocity space using the Jacobian transform, $P_v(v) = tr^2S(t)$, where $v = r/t$ and $S(t)$ is the measured signal intensity at each time. The 2 + 1 REMPI spectrum of H_2O was simulated with PGOPHER, a freely available program for simulating rotational spectra.[58] More details about this procedure are available in Section 3.2.3.

4.3 Results

4.3.1 2 + 1 REMPI spectrum for H_2O (v = 0)

The 2 + 1 REMPI spectrum of desorbed water from 1 L ASW at 102 K on the impact melt breccia exhibited rotational excitation, with a rotational temperature of 300 ± 75 K. For thick ASW, the rotational temperature was 425 ± 75 K (Chapter 3), but the data were quite similar on the lunar slabs. The true rotational temperature for both substrates may be 350-375 K, and unavoidable fluctuations in laser powers may be responsible for the slight differences in peak heights. The experimental spectrum in Figure 4.2 (black circles) was created by scanning a 0.2-nm interval in 0.0025-nm increments, averaging data from 64 laser pulses at each wavelength. A fresh 1 L of water was dosed prior to each 0.2-nm interval to avoid signal decreasing as coverage decreased. Each data point shown is the average of the signal from at least two scans with different starting wavelengths. In determining the temperature of best fit, least emphasis was placed below 248 nm because ionization laser power was not stable at those wavelengths.

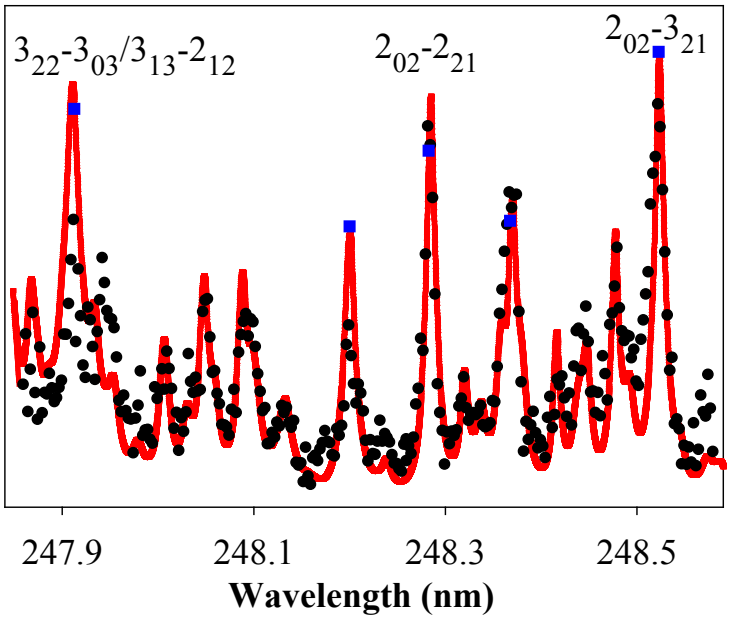

Figure 4.2. 2 + 1 REMPI spectrum of photodesorbed water from 1 L ASW on the impact melt breccia (black circles) and mare basalt (blue squares). The red line is a simulated spectrum with a rotational temperature of 300 K.

During measurements on the mare basalt, the REMPI laser power varied too greatly with wavelength to do a full scan. Instead, only the five largest peaks were examined. Because the REMPI laser power at each of these five wavelengths was forced to be the same, the relative heights of the blue squares in Figure 4.2 are actually more accurate than the relative heights of the black circles. The simulated spectrum with a rotational temperature of 300 K appears to fit water photodesorbed from the mare basalt even better than from the impact melt breccia at lower wavelengths.

4.3.2 TOF spectra and velocity distributions

The shapes of the H_2O TOF spectra from ASW on the lunar slabs were found to be independent of exposure (from 1 to 20 L), desorption laser flux, and ionization energy.

Figure 4.3 shows the TOF spectrum for H_2O desorbing from 2 L ASW on the impact melt breccia and the three Maxwell-Boltzmann components calculated according to Equation (4.1) with r = 2 mm that sum to the total fit. Similarly, Figure 4.4 shows the TOF spectrum for H_2O desorbing from 5 L ASW on the mare basalt and the three Maxwell-Boltzmann components calculated according to Equation (4.1) with r = 2.5 mm that sum to the total fit. These TOF spectra were very similar to that of desorbed water from thick ASW dosed directly onto the sample holder, except that the spectra from the lunar slabs were wider. Due to water desorbing from within pores in the lunar slabs, thermal components were added to account for some of the extra width. The larger two components had T_{trans} = 550 and 1800 K, though these exact translational temperatures were somewhat arbitrary.

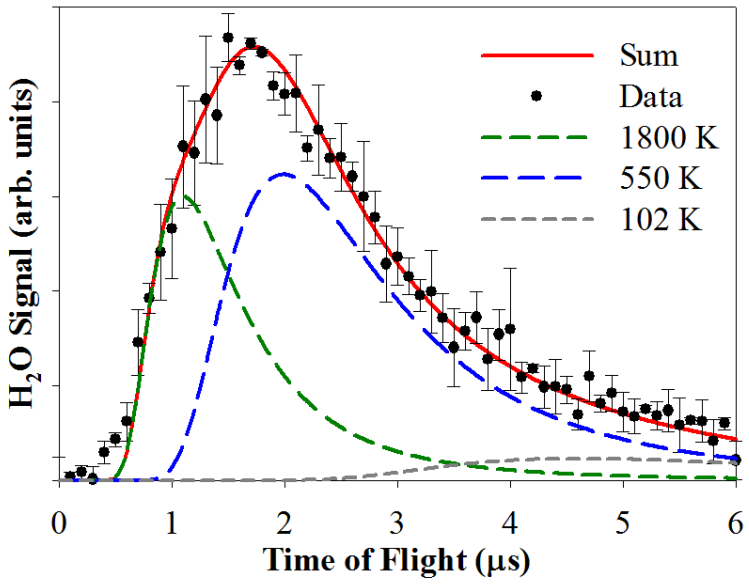

Figure 4.3. TOF spectrum for H_2O desorbing from 2 L ASW on the impact melt breccia at 102 K due to 157-nm irradiation. Maxwell-Boltzmann distributions with r = 2.0 mm and T_{trans} = 1800, 550, and 102 K sum to fit the data.

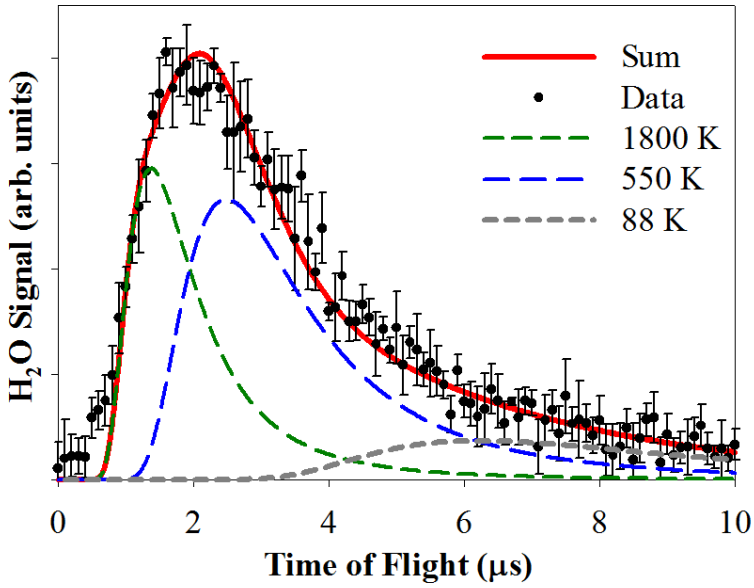

Figure 4.4. TOF spectrum for H_2O desorbing from 5 L ASW on the mare basalt at 88 K due to 157-nm irradiation. Maxwell-Boltzmann distributions with r = 2.5 mm and T_{trans} = 1800, 550, and 88 K sum to fit the data.

If only the peak of the TOF spectra were fit with one Maxwell-Boltzmann distribution, as in Chapter 3, T_{trans} would be 800 K ± 300 K (0.14 ± 0.05 eV). The single-component translational temperature was 700 ± 200 K for desorption from 600 L ASW (Chapter 3), so the peak position is the same on the lunar slabs, within error.

As shown in Section 3.2.2, an alternate method of fitting the data that yields a wider distribution, by integrating over the desorption laser spot, was unsubstantiated by experiments. However, it theoretically makes sense that the distribution should be wider when all desorption trajectories are included instead of assuming that all water molecules leave normal to the surface. Complications due to pores in the lunar slab and collisions between desorbing particles make modeling these desorption events very difficult. While it is easy to imagine how off-normal trajectories and collisions can lead to lower effective translational temperatures, they should not be able to explain the large amount of

desorbing water with higher translational temperatures than from thick ASW. However, different adsorption environments are available to water on the lunar substrates (further discussion in Section 4.4.1). Since there are two primary categories of adsorption geometries, either interacting with the surface through oxygen or through hydrogen, we have chosen to fit the data with two non-thermal components.

Because the data from the two lunar slabs were collected at different values of *r*, it was difficult to compare them directly until after the Jacobian transformation to velocity space. The two velocity distributions were very similar (see Figure 4.5). However, because data from the mare basalt were collected at 88 K instead of 102 K, the slowest velocities were slightly lower from the mare basalt. The peak of both velocity distributions corresponded to a velocity of ~900 m/s.

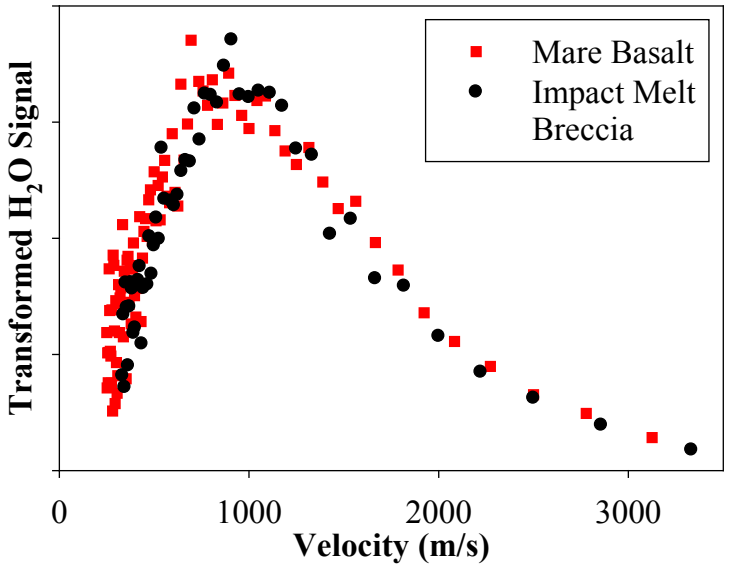

Figure 4.5. Velocity distributions of photodesorbed water from 2 L ASW on the impact melt breccia at 102 K (black circles) and 5 L ASW on the mare basalt at 88 K (red squares).

Desorption signal was found to be linear with respect to desorption laser flux. This result was already shown for desorption energies below 100 μJ cm^{-2} in Chapter 3, but signal was much lower for low H_2O exposures on the lunar slabs than for 600 L ASW on the sample holder. Consequently, higher desorption energies were required to obtain adequate signal-to-noise ratios. Figure 4.6 shows that water signal at TOF = 1.7 μs increases linearly with energy per pulse, so a single-photon mechanism of desorption is still indicated.

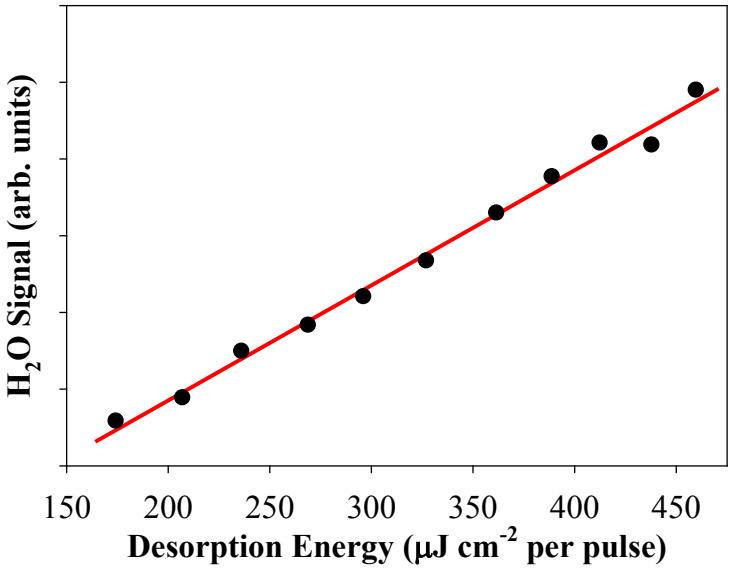

Figure 4.6. H_2O photodesorption signal from 10 L ASW on the impact melt breccia at 102 K as a function of desorption energy per pulse. A linear regression is shown in red.

4.3.3 Cross sections for water removal

Water removal cross sections were measured on both lunar slabs at 0.1, 0.3, 1, 5, and 10 L exposures, and they were found to increase with decreasing coverage. Figure 4.7 shows cross sections for water removal on the lunar slabs and on copper, which probably has an oxidized surface, for comparison. The mare basalt and impact melt breccia had

remarkably similar cross sections for water removal at all exposures. The cross section for 10 L H_2O on the lunar slabs, $(8.7 \pm 3.3) \times 10^{-20}$ cm^2, matches that for 10 L H_2O on the oxidized copper sample holder, $(7.8 \pm 1.5) \times 10^{-20}$ cm^2. The 5 L cross section on the lunar slabs, $(1.7 \pm 0.5) \times 10^{-19}$ cm^2, was slightly higher than on oxidized copper. As expected, the most profound differences occur at low coverages. For example, the 1 L cross section for H_2O removal from the lunar slabs, $(3.6 \pm 0.8) \times 10^{-19}$ cm^2, was almost an order of magnitude greater than the corresponding cross section on oxidized copper.

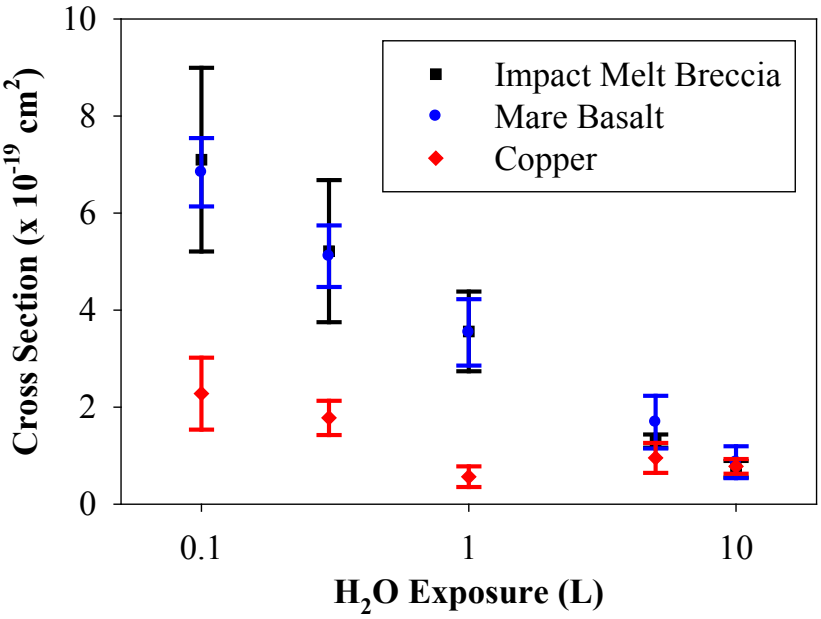

Figure 4.7. Water removal cross sections for various H_2O exposures on the impact melt breccia at 102 K and on the mare basalt at 88 K. For comparison, corresponding cross sections are also shown for ASW on copper (probably oxide-coated).

4.3.4 Photofragments from vibrationally excited water

While predissociation made direct detection of H_2O (v*) impossible, TOF spectra for the H^+ and OH^+ fragments from vibrationally excited water were detected via non-resonant

ionization at 253 nm. All Maxwell-Boltzmann distributions shown in Figure 4.8 were calculated according to Equation (4.1) with T_{trans} = 1200 K. The uncertainty in flight distance corresponds to the following uncertainty in translational temperature: T_{trans} = 1200 ± 300 K (0.21 ± 0.05 eV). These TOF spectra were nearly identical to those from thick ASW on the oxidized copper sample holder (Figure 3.10). However, as with the TOF spectra for H_2O ($v = 0$), there was some additional fast signal that could not be explained by off-normal trajectories, collisions, pores, and surface roughness. Although not shown in Figure 4.8, the data could be fit with two components corresponding to the two primary categories of adsorption geometries: oxygen down and oxygen up.

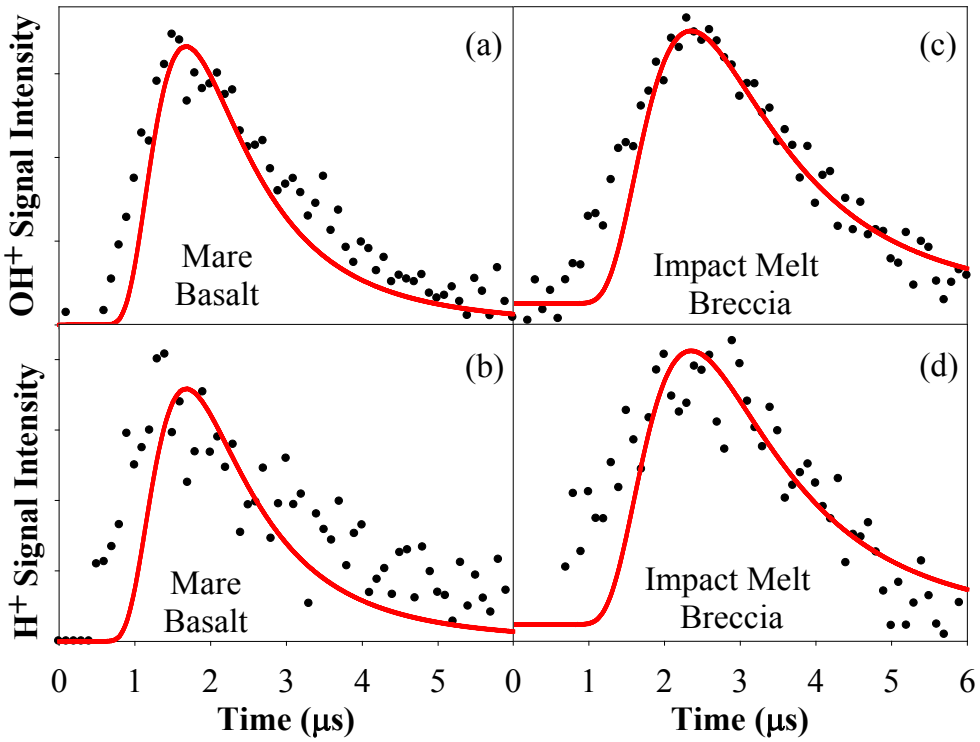

Figure 4.8. TOF spectra of OH^+ (a,c) and H^+ (b,d) fragment ions from vibrationally excited H_2O molecules desorbed by 157-nm photons from 5 L ASW on the mare basalt (a,b) at 88 K and on the impact melt breccia (c,d) at 102 K. Maxwell-Boltzmann distributions with T_{trans} = 1200 K fit the peaks. r = 2.5 mm (a,b) and 3.5 mm (c,d).

OH^+ signals at the peaks of these TOF spectra (Figure 4.8a,c) were monitored as a function of irradiation time. For 5 L H_2O exposure, OH^+ signal increased until irradiation by ~ 5 x 10^{18} photons cm^{-2} on the impact melt breccia and until irradiation by ~ 5 x 10^{17} photons cm^{-2} on the mare basalt. When OH^+ signals finally began to decrease, the depletion cross sections were 6.4 x 10^{-20} cm^2 on the impact melt breccia and 1.2 x 10^{-19} cm^2 on the mare basalt. These cross sections represent H_2O (v*) removal, assuming that the entire OH^+ signal was in fact due to H_2O (v*).

4.4 Discussion

4.4.1 H_2O photodesorption mechanisms

In Chapter 3, for the desorption of H_2O ($v = 0$) by 157-nm irradiation of thick ASW, we supported a mechanism involving dipole reversal, in which unfavorable electrostatic interactions between the excited surface water molecule and its neighbors result in desorption. Because the TOF spectra for photodesorption of water from the lunar slabs are similar to that of water from thick ASW, the same mechanism is probably responsible. Additionally, small thermal components were observed from ASW on the lunar slabs. These thermal components likely arise when water desorbing from within pores equilibrates to the surface temperature before finally escaping.

Since the lunar slabs are mixed metal oxides, there are many different adsorption sites available to water molecules. Much like for the powdered lunar simulants in Chapter 2, we expect a continuum of desorption energies. Although desorption in this case is not thermal, the strength of the interaction between a water molecule and the substrate can affect the energy with which the water molecule desorbs by changing the relevant

potential energy surfaces. For example, when the excited water molecule is surrounded by metal cations and oxygen anions instead of by other water molecules, the excitation may remain more localized, and the dipole reversal mechanism may lead to even stronger repulsion between the water molecule and the surface. Because there are two primary categories of adsorption geometries, either interacting with the surface through oxygen or through hydrogen, we have chosen to lump the desorbing water into two non-thermal components. However, the reality of water adsorption on these surfaces is much more complicated, as different metal ions undoubtedly affect water adsorption differently.

As in Chapter 3, photodesorption of H_2O (v*) may be due to several different mechanisms: dipole reversal, kick out, and recombination of hydroxyls. The formation of H_2O (v*) is likely due at least in part to recombinative desorption of photofragments because signal indicative of H_2O (v*) increases with irradiation time. As photodissociation occurs, more OH radicals become available for recombination: OH + OH $\rightarrow$ H_2O + O. The resulting water molecules are predicted to exhibit significant vibrational excitation.[55] Chapters 5 and 6 focus on the $O(^3P_J)$ fragment, which also increases with irradiation time and is primarily formed by hydroxyl recombination and photodissociation. In fact, for 5 L H_2O exposure on the impact melt breccia, signals indicative of $H_2O(v^*)$ and $O(^3P_J)$ both increase for 5 x 10^{18} photons cm^{-2} and then decrease with similar cross sections (see Chapter 6), so it is plausible that both signals depend upon the extent of surface hydroxylation.

4.4.2 Water removal cross section

The cross sections for water removal at low coverages were higher on the lunar slabs than on oxidized copper, and this difference may result from interactions between water and the lunar surfaces. If charge transfer between a water molecule and the lunar surface occurs, the equilibrium geometry of the water molecule could change, resulting in a different potential energy surface that could become excited with less photon energy. In this case, 7.9 eV photons could be near the peak of the first absorption band rather than on the edge, so more desorption and dissociation could occur. In addition, coupling to a thin Cu-O layer may lead to more effective quenching of the first electronic state of water. When quenching occurs more quickly, there is less time for the excited water molecule to gain momentum while on the repulsive potential energy surface, so desorption is less likely.

Differences in quenching rates at different H_2O exposures can also explain why cross sections increase with decreasing exposure on all substrates studied. Quenching of the excited state is very rapid within defect-free ice, as the exciton diffuses easily along hydrogen bonds. For low exposures, water clusters are smaller, and quenching of the excited state is less rapid, so there is more time for the excited water molecule to accelerate away from the surface while on the excited-state potential energy surface.

The branching between desorption and dissociation also depends on whether water molecules are isolated or in clusters. For gas-phase H_2O, excitation to the first excited state is purely dissociative. However, in water hexamers, delocalization of the exciton, which facilitates desorption, occurs on the same femtosecond time scale as photodissociation.[13] Since desorption requires some exciton delocalization (but not too

much, too fast), dissociation may be much more likely than desorption for isolated H_2O molecules on the surface. Lower H_2O exposures lead to more isolated water molecules, which are more easily photodissociated.

Therefore, the water removal cross sections for low H_2O exposures on the lunar slabs are likely due in large part to photodissociation. Many of the hydroxyls formed by photodissociation eventually recombine to form H_2O again, but these water molecules have vibrational excitation and thus are not detected at the same REMPI wavelength. By non-resonant detection of photofragments, the cross section for H_2O (v*) from 5 L ASW on the impact melt breccia was found to be 6.4×10^{-20} cm^2. This value is similar to the cross section for $O(^3P_J)$ depletion from 5 L ASW on the impact melt breccia, 4.6×10^{-20} cm^2 (Chapter 6), because both $O(^3P_J)$ and OH^+ yields depend primarily on the concentration of adsorbed hydroxyls.

4.4.3 Implications for water on the Moon

Because photodissociation of water appears to become more important than photodesorption for low coverages of ASW on the lunar slabs, it is unlikely that a significant amount of intact desorption of H_2O ($v = 0$) occurs at the low coverages of water that may be present on the sunlit lunar surface (up to 1000 ppm).[23] Although H_2O ($v = 0$) signal beings to decrease within the first few seconds (usually after less than 10^{16} photons cm^{-2}), fragments of H_2O (v*) increase initially, indicating an increasing number of hydroxyl recombination reactions. With increasing irradiation, water on the lunar surface is replaced by hydroxyls. These hydroxyl groups are stable at lunar temperatures and will not recombine thermally below 425 K,[1, 40] but solar photons allow recombination

reactions to form vibrationally excited water and oxygen atoms. Still, some H_2O molecules must remain for these photo-induced recombination reactions to occur, as they require at least one hydroxyl radical to be newly formed by irradiation of water (see Chapter 5).

Since the total amount of OH + H_2O on the Moon is low, photodissociation probably dominates over direct desorption of water. The most relevant cross sections to use in modeling the removal of OH + H_2O from the lunar surface may be 6.4 x 10^{-20} cm^2 and 1.29 x 10^{-19} cm^2, from the OH^+ fragment of H_2O (v*) on the impact melt breccia and mare basalt, respectively.

We can estimate the flux of H_2O (v*), $\Phi_{H2O\ (v^*)}$, from the lunar surface by ultraviolet photons using our measured cross sections and some assumptions based on values from the literature. The solar photon flux, F_{ph}, at the lunar surface above 8 eV is 10^{12} photons cm^{-2} s^{-1}.[79] Our 7.9-eV irradiation is just within the first absorption band of water, and most solar photons greater than 8 eV will also be in this first absorption band and will dissociate water at similar rates. Initial coverage depends largely on the exact location on the lunar surface. For Goldschmidt crater, which exhibited residual neutron enhancements compared to surrounding areas, 0.1-1 wt % water-equivalent hydrogen is plausible in the top layer 1.7 – 17 cm of lunar regolith, with a density of 1.8 g cm^{-3}.[80] Using 0.5 wt % hydrogen, the top 0.66 nm (about 1 ML) of lunar regolith should contain about 3.6 x 10^{14} water-equivalent hydrogens per cm^2. Since we believe that our cross section was obtained after irradiation significantly hydroxylated the surface, many of these water-equivalent hydrogens may actually be part of OH groups, but both H_2O and OH are required for recombination reactions. If we assume that an equal number of OH

groups and H_2O molecules are present, the water-equivalent hydrogens are part of 1.2 x 10^{14} OH groups and H_2O molecules per cm^2. Since Goldschmidt crater has experienced many impact events, we choose the cross section from the impact melt breccia, $\sigma = 6.4 \times 10^{-20}$ cm^2. The flux of H_2O (v^*) from the sunlit parts of Goldschmidt crater due to solar photons is then

$$\Phi_{H2O\ (v^*)} = F_{ph}\, \sigma\, \theta \approx 7.7 \times 10^6 \text{ molecules cm}^{-2}\ \text{s}^{-1}, \quad (4.2)$$

where θ is coverage in units of molecules cm^{-2}.

In the past, authors needing quantitative information about water photodesorption on the Moon[81, 82] used the cross section from Westley et al.[45] or the yield from Oberg et al.,[44] even though their laboratory studies involved thick ices on quartz and gold, respectively. Now, cross sections measured on an actual lunar substrate can be used instead.

4.5 Conclusion

Desorption of H_2O ($v = 0$) following 157-nm irradiation of amorphous solid water on a lunar impact melt breccia and a lunar mare basalt was detected with REMPI. Photofragments of vibrationally excited water were detected with non-resonant ionization. Cross sections for water removal were measured at 0.1, 0.3, 1, 5, and 10 L exposures, and they were found to increase with decreasing coverage. As demonstrated above, the cross sections for H_2O direct desorption and recombinative desorption can be used in modeling water lifetimes on the Moon. When water is either formed on or transported to the sunlit surface of the Moon, it may be photodissociated or photodesorbed by solar photons.

CHAPTER 5

$O(^3P_J)$ FORMATION BY PHOTOIRRADIATION OF AMORPHOUS SOLID WATER

5.1 Introduction

In Chapters 3 and 4, photodesorption of intact water molecules was examined, but the competition between desorption and dissociation in the excited state has another possible victor. In Chapters 5 and 6, the corresponding photodissociation events will be investigated through experimental detection of $O(^3P_J)$.

Oxygen atoms, which may be produced by photodissociation of water, have been observed in several exospheres within our solar system.[83] The neutral clouds around Saturn, containing H_2O, OH, and O, are thought to originate from water ice on Enceladus.[84, 85] Hydroxyls were first detected in Saturn's magnetosphere by the Faint Object Spectrograph on the Hubble Space Telescope.[86] Since then, an atomic oxygen cloud has been observed that is even broader than the OH cloud.[87] Models of the neutral cloud coming from Enceladus include losses due to charge exchange, dissociation, and ionization of H_2O, OH, and O.[88] Therefore, it is important to examine the yields of atomic fragments due to photodissociation of water. Neutral-neutral collisions within the cloud are also included in recent models to account for some of its outward spreading.[89] Although only gas-phase interactions are generally included in models, condensed-phase processes may also be important in the neutral cloud, since geysers on Enceladus can release dust grains into the cloud.[90] When an icy grain surface is involved, H_2O and O may be produced by recombination of OH radicals produced by electronic excitation.

This reaction is one of the primary mechanisms of $O(^3P_J)$ formation and release discussed in the present work.

Because photodissociation of water is such an important process in atmospheric, interstellar, and planetary chemistry, it has been studied extensively.[74, 91-95] Even when the primary experimental goal is to measure photodesorption of water, a significant amount of photodissociation occurs and complicates the interpretation of measured water removal cross sections.[2, 44, 45] $O(^3P_J)$ formation by 157-nm irradiation of 1500 L ASW at 90 K has been measured previously by Hama et al., who found that four Maxwell-Boltzmann components with translational temperatures of 5000, 1300, 300, and 100 K fit their data.[74] The 5000 K component, which was attributed to hydroxyl dissociation, increased significantly with 30 minutes of prior irradiation when compared to freshly dosed ASW.[74] When compared to the TOF spectrum of $O(^3P_J)$ from ASW, the TOF spectrum for $O(^3P_J)$ from H_2O_2 was found to be roughly the same shape but twice as intense.[74] This result lends credence to the idea that most of the $O(^3P_J)$ desorbing from ASW is indirectly formed by hydroxyl radicals, since twice as many hydroxyls are formed during irradiation of H_2O_2. Though several different hydroxyl recombination mechanisms may account for the three slowest translational temperature components, no attempt was made to assign individual components to these different pathways.[74] The present study examines the pathways of photo-induced formation and release of $O(^3P_J)$ from ASW with well-resolved TOF measurements, extracts cross sections for $O(^3P_J)$ depletion, further examines the effect of cumulative irradiation, and determines $O(^3P_J)$ spin-orbit temperatures as a function of H_2O exposure.

5.2 Experimental Details

All experiments were performed in the ultra-high vacuum (UHV) chamber described in Chapter 3. The chamber's base pressure was 2 x 10^{-10} Torr, and background dosing of H_2O was typically performed at pressures between 1 x 10^{-8} and 1 x 10^{-7} Torr. Experiments were performed at 82 K, the minimum temperature of the copper substrate, unless otherwise stated. As stated in Section 3.2.1, the copper substrate was not sputtered between experiments, so the metal was probably covered with a thin oxide layer.

Dissociation energies were typically 160-180 μJ cm^{-2} per pulse. O($^3P_{J=2,1,0}$) photoproducts were detected with 2 + 1 REMPI via the O(^3P_J – ^3P_J) transitions at 225.6 – 226.4 nm.[96] The time between desorption and ionization was varied with a delay generator from 0 to 30 μs to probe different parts of the desorption plume. This delay time equals the flight time of the atom from the surface to the detection region. The oxygen peak in each mass spectrum was integrated to obtain the total signal for each time delay, and the resulting graph of signal versus time delay is the TOF spectrum. These measurements were carried out for each spin-orbit state at several H_2O exposures.

Flux-weighted Maxwell-Boltzmann distributions were used to simulate the TOF spectra.[56] Four Maxwell-Boltzmann components, $S(t, T_{trans})$, were required to adequately fit the experimental data:

$$S(t, T_{trans}) = At^{-4}\exp\left(\frac{-mr^2}{2k_B T_{trans} t^2}\right), \quad (5.1)$$

where T_{trans} is the translational temperature, r is the distance between the surface and the detection region, and A is a scaling factor. The distance between the surface and the detection region was determined to be 3 mm by fitting the thermal component using a Maxwell-Boltzmann distribution with T_{trans} = 82 K.

Using the Jacobian transform, $P_v(v) = tr^2 S(t)$, where $v = r/t$ and $S(t)$ is the measured signal intensity at each time, $O(^3P_J)$ data were also plotted in velocity space. Velocity distributions were fit with Maxwell-Boltzmann components of the form:

$$P_v(v, T_{trans}) = Av^3 \exp\left(\frac{-mv^2}{2k_B T_{trans}}\right), \quad (5.2)$$

where the values of T_{trans} were those used to fit the TOF spectra.

5.3 Results

5.3.1 REMPI spectrum

Figure 5.1 shows a representative REMPI spectrum for $O(^3P_J - {}^3P_J)$ transitions due to 157-nm irradiation of 600 L ASW with TOF = 1.4 μs. Wavelengths shown in Figure 5.1 are in air, and the corresponding vacuum wavelengths can be found by adding ~ 0.06 nm. The ratio of the peak areas is 5.9 to 2.4 to 1 for J = 2, 1, and 0.

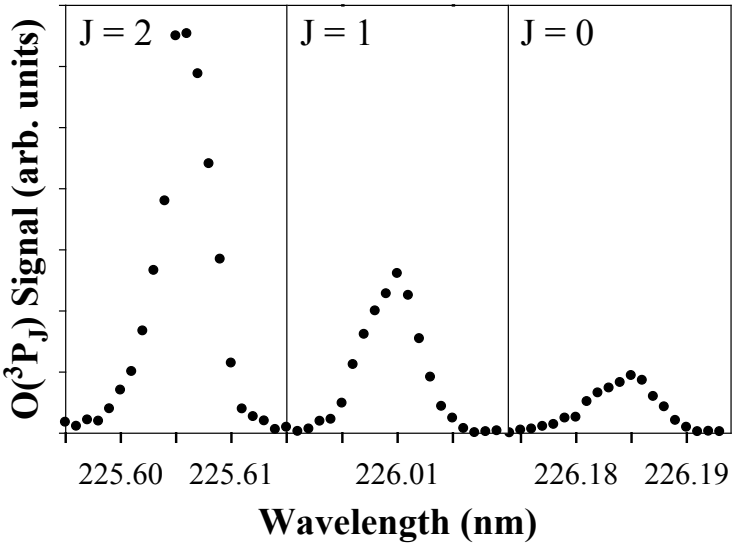

Figure 5.1. REMPI spectrum of $O(^3P_J)$ desorbing from 600 L ASW at 85 K due to 157-nm irradiation. TOF = 1.4 μs.

Generally, to calculate the spin-orbit temperature, one would divide these values by the degeneracy of each state: 5, 3, and 1 for J = 2, 1, and 0, respectively, then plot the natural log of those values versus energy, and finally set the slope equal to $-1/k_B T_{spin\text{-}orbit}$. However, in this case, the shape of the TOF spectrum is different for J = 2, so using only the signal intensity at one flight time does not yield complete information. Instead, integration of the TOF spectrum and its components is required.

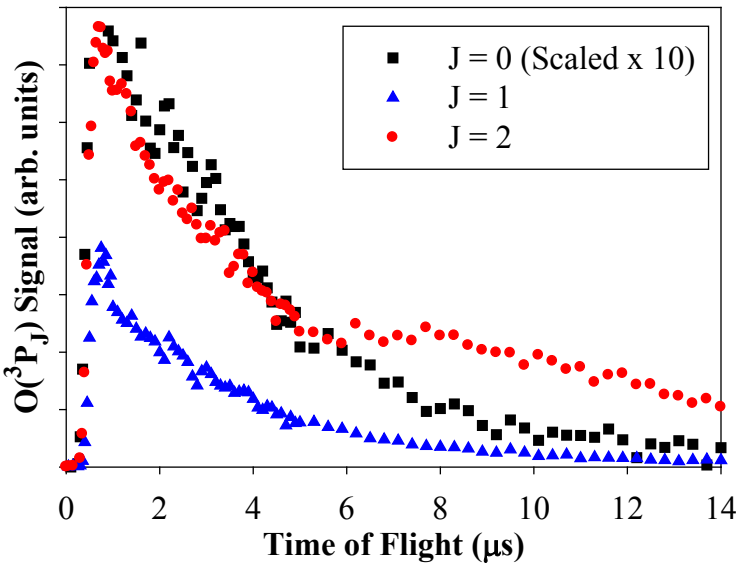

Figure 5.2. TOF spectra of $O(^3P_J)$ desorbing from 600 L ASW on copper at 82 K due to 157-nm irradiation.

5.3.2 TOF spectra and velocity distributions

Figure 5.2 shows that the slowest component of the TOF spectrum from 600 L ASW is much larger for J = 2 (the ground state) than for J = 1 or 0. The $O(^3P_0)$ TOF spectrum has been multiplied by 10 to allow a direct comparison with the $O(^3P_2)$ spectrum. The $O(^3P_1)$ spectrum has the same shape as the $O(^3P_0)$ spectrum, but it has not been scaled.

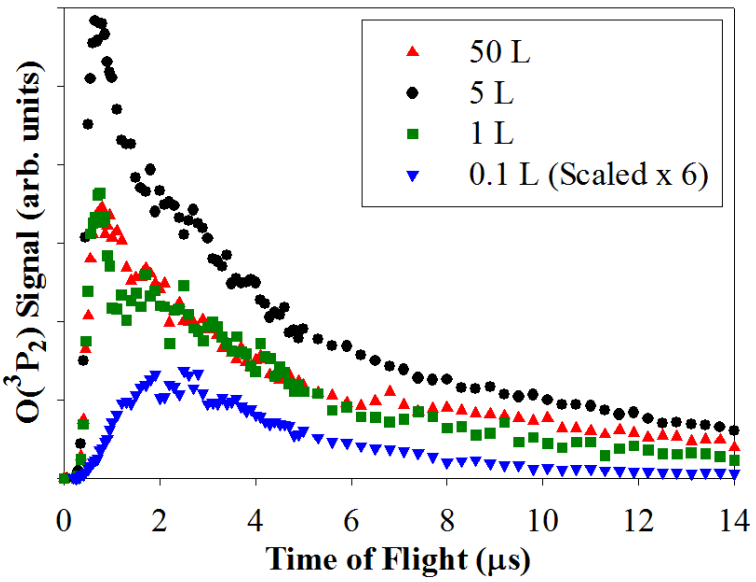

Figure 5.3. TOF spectra of $O(^3P_2)$ desorbing from 0.1, 1, 5, and 50 L ASW on copper at 82 K due to 157-nm irradiation.

The slowest component also disproportionately increased with coverage for J = 2. The TOF spectra in Figure 5.3 have not been scaled, so 1 L and 50 L H_2O exposure led to very similar spectra, except that the slowest peak was slightly larger in the 50 L TOF spectrum. While exposures ≥ 1 L had a very fast component peaked around 0.7 μs, this peak was not present at 0.1 L.

TOF spectra were also measured for J = 1 and J = 0 at 0.1, 1, 5, 50, and 600 L. All of these TOF spectra were fit with a sum of up to four Maxwell-Boltzmann components calculated using Equation 5.8 with r = 3.0 mm and translational temperatures of 10,000 K, 1800 K (allowed to vary between 1600 and 2000 K to get best fit for each scan), 400 K, and 82 K. A sub-thermal, non-Maxwellian component was also observed in some scans at high coverage. Figure 5.4 shows the 600 L ASW TOF spectrum for J = 2, the four Maxwell-Boltzmann components, and the sum of those components. The error bars

represent 95% confidence intervals calculated from many scans after substantial irradiation. After fitting the TOF data with four Maxwell-Boltzmann distributions, the signal that was not fit by their sum at longer flight times was referred to as "the diffusion component." Although Figure 5.4 only shows data up to 14 μs, signal was collected out to 30 μs so that the entire diffusion component could be captured.

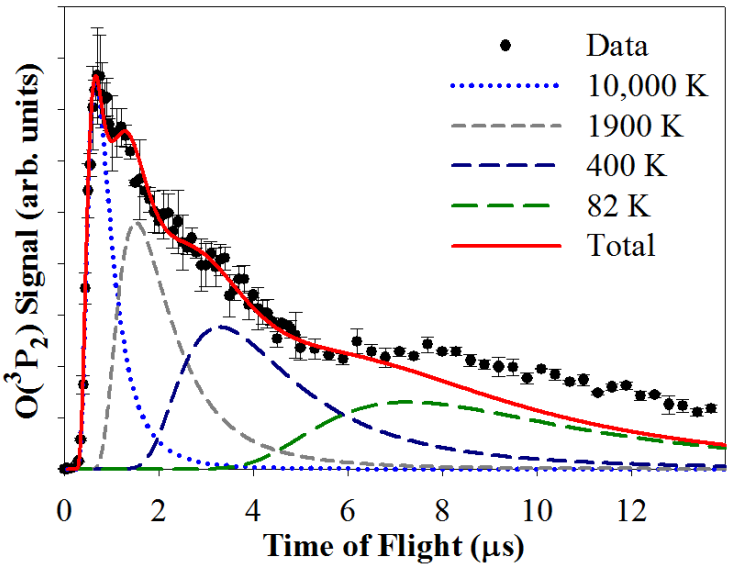

Figure 5.4. TOF spectrum of $O(^3P_2)$ desorbing from 600 L ASW on copper at 82 K due to 157-nm irradiation.

The corresponding $O(^3P_2)$ velocity distribution from 600 L ASW on copper is shown in Figure 5.5. Velocities up to 8000 m/s were observed. The most common velocity was 300 m/s, and the second highest peak appeared at 845 m/s. Because of the significant diffusion component, the velocity distribution in Figure 5.5 could not be used to accurately determine the value of *r* using the thermal component.

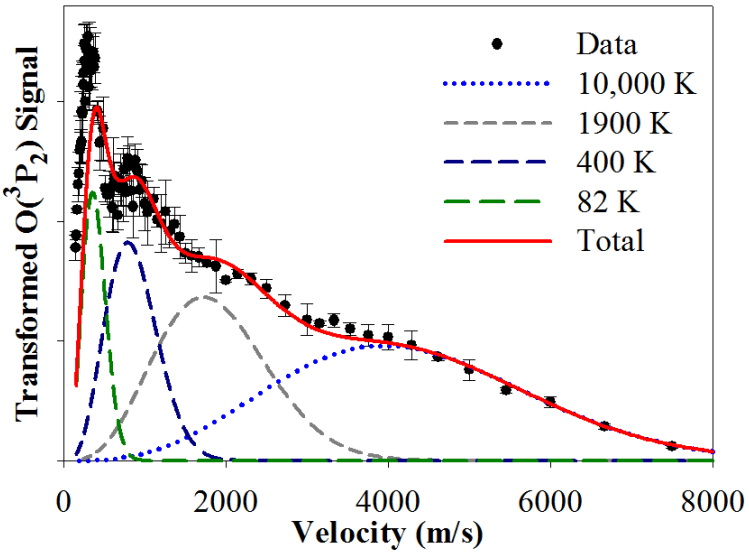

Figure 5.5. Velocity distribution of $O(^3P_2)$ desorbing from 600 L ASW on copper at 82 K due to 157-nm irradiation.

Instead, the value of *r* was determined using the velocity distribution of $O(^3P_2)$ from a thin layer of ASW deposited on the copper from the background water in the UHV chamber with no intentional dosing (Figure 5.6). With this extremely low coverage of ASW, no diffusion component was present. Because the 82 K component fit the data best at 3.0 mm, that flight distance was used for all fits. The most common velocities for $O(^3P_2)$ desorbing from a thin layer of ASW background-deposited on copper at 82 K were 600-800 m/s.

The corresponding TOF spectrum is shown in Figure 5.7. Because the $O(^3P_2)$ signal from background-deposited ASW was quite low, some interference occurred from ions produced solely by the excimer laser. The erratic signal around 3 μs can be explained by this interference. The 10,000 K component was almost unnecessary in fitting the data in Figures 5.6 and 5.7.

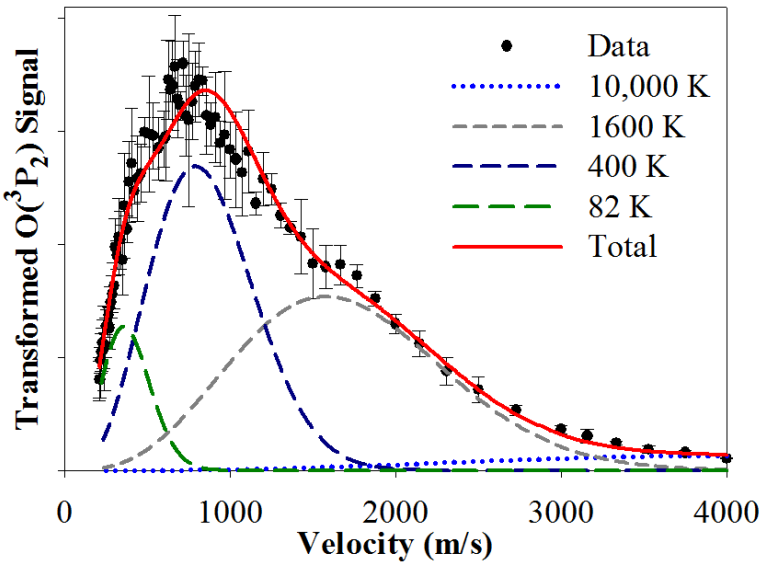

Figure 5.6. Velocity distribution of $O(^3P_2)$ desorbing from a thin layer of ASW background-deposited on copper at 82 K due to 157-nm irradiation.

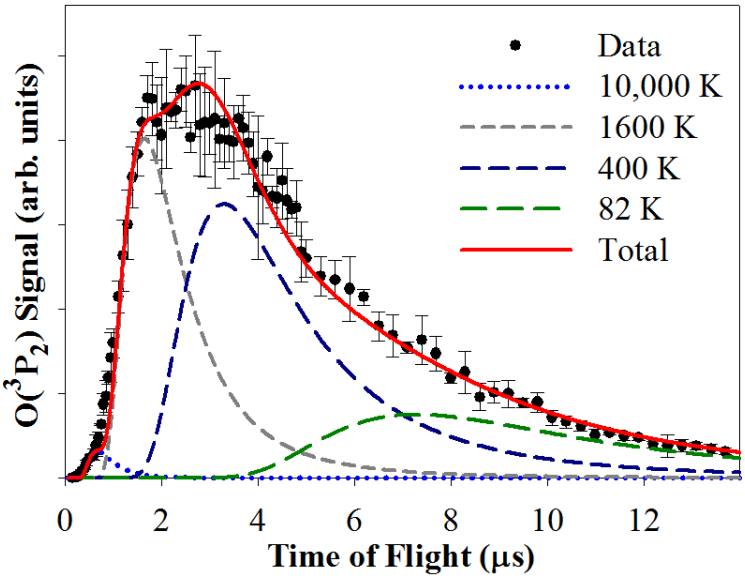

Figure 5.7. TOF spectrum of $O(^3P_2)$ desorbing from a thin layer of ASW background-deposited on copper at 82 K due to 157-nm irradiation.

Table 5.1 summarizes the relative yields and component areas for each spin-orbit state at each exposure. The rows labeled "Background" show the percentage of the total TOF area attributed to each Maxwell-Boltzmann component for scans performed without any intentional dosing of water. Therefore, "0.1 L" should be interpreted as 0.1 L on top of the unknown amount of water deposited during cooling. This amount of unintentional dosing could not be calculated because irradiation during cooling was used to keep the surface contaminant-free. The diffusion and thermal components were largest for J = 2 at ≥ 1 L exposure. 5 L, 50 L, and 600 L TOF spectra were very similar for J = 1 and 0.

Table 5.1. Relative yields for each $O(^3P_J)$ TOF spectrum and percentages of TOF areas attributed to each Maxwell-Boltzmann or diffusion component.

ASW on Copper	Rel. Yield	10,000 K	1800 K	400 K	82 K	Diffusion
J = 0						
Background	*1.0*	1.2	31.3	59.8	7.7	
0.1 L	*1.0*	4.5	35.4	54.9	5.2	
1 L	*3.6*	24.1	20.7	46.6	8.6	
5 L	*8.5*	27.4	28.9	31.9	11.8	
50 L	*5.2*	18.4	30.1	36.2	15.3	
600 L	*5.7*	24.3	27.1	37.3	11.4	
J = 1						
Background	*2.0*	1.9	35.2	50.2	12.7	
0.1 L	*2.6*	2.5	40.4	46.3	10.8	
1 L	*16.1*	24.1	28	39.7	8.2	
5 L	*20.7*	29.2	29.5	29.1	12.2	
50 L	*17.2*	18.2	31.3	35.9	14.6	
600 L	*16.5*	24.4	29.2	33.4	13.0	
J = 2						
Background	*4.2*	1.3	30.4	51.0	17.3	
0.1 L	*6.2*	2.6	36.5	47.3	13.6	
1 L	*50.4*	16.5	19.2	32.6	22.0	9.7
5 L	*90.0*	14.6	18.5	26.3	22.6	18.0
50 L	*59.4*	12.7	18.4	24.0	21.2	23.7
600 L	*60.1*	11.8	16.9	21.1	20.2	30.0

Table 5.2 shows the Boltzmann temperatures of the spin-orbit levels, $T_{spin\text{-}orbit}$, associated with each TOF component and the overall yields for each exposure. Several of the calculated temperatures were negative, corresponding to a situation in which there was much more J = 0 and much less J = 2 signal than expected. Negative spin-orbit temperatures, therefore, indicate even more excited oxygen atoms than do extremely positive spin-orbit temperatures. The average overall temperature was 543 K, similar to the 600 K spin-orbit temperature reported from 1500 L ASW kept fresh by pulsed dosing.[74]

Table 5.2. Boltzmann temperatures (K) of the spin-orbit levels based on overall $O(^3P_J)$ TOF yields and on the contributions of the individual TOF components.

ASW on Copper	10,000 K	1800 K	400 K	82 K	Overall
Background	Negative	Negative	Negative	496	Negative
0.1 L	Negative	1226	2181	237	1229
1 L	543	383	492	161	324
5 L	1979	877	486	211	381
50 L	698	1004	770	267	378
600 L	2060	1148	1451	226	403

5.3.3 Irradiation dependence

The spin-orbit temperature reported for 1500 L ASW after 30 minutes of 157-nm irradiation was 1000 K,[74] and the present study also found significant changes due to increasing irradiation. The TOF spectra summarized in Table 5.1 were measured after the initial period of irradiation during which signal increases dramatically, as shown in Figure 5.8. Both $O(^3P_2)$ and $O(^3P_1)$ signals increased much more quickly for the 10,000 K

component (TOF = 0.7 μs) than for the 400 K component (TOF = 3.1 μs). The 10,000 K component seemed to decrease more quickly than the other components as well, but the difference between components in rate of decrease was minor compared to the difference in rate of increase during initial radiation.

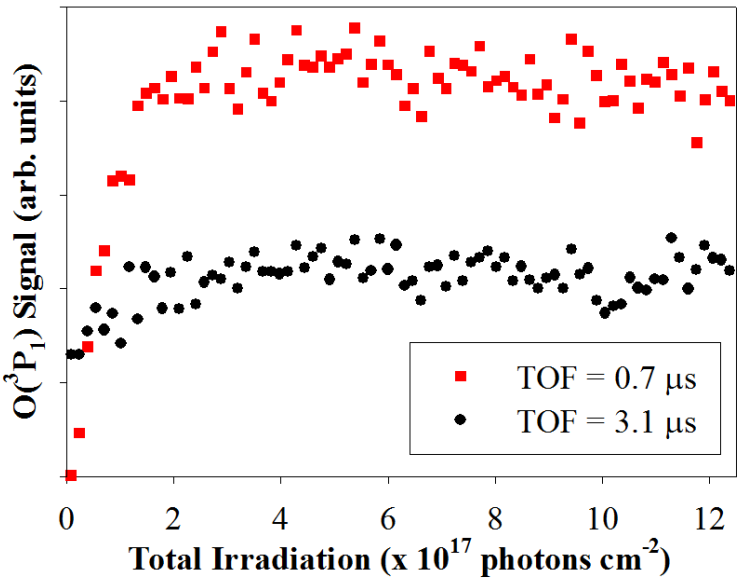

Figure 5.8. $O(^3P_1)$ desorbing from 1 L ASW on copper at 82 K as a function of total 157-nm irradiation. Red squares represent the 10,000 K component at TOF = 0.7 μs, and black circles represent the 400 K component at TOF = 3.1 μs. The same behavior was observed for $O(^3P_2)$.

A rapid increase in the 10,000 K component was observed for all exposures ≥ 1 L. After maximum signal was reached, $O(^3P_J)$ signal remained constant on experimental time scales for 50 L and 600 L. Figure 5.9 shows the change in total $O(^3P_2)$ signal (integrated over time from 0 to 20 μs) with cumulative irradiation for 1 L and 5 L ASW on copper. The dashed curves represent exponential fits of the form $y = Ae^{-\sigma x}$, where x

has units of photons cm^{-2} and σ is the cross section for $O(^3P_2)$ depletion. The cross sections were 1.3×10^{-19} and 6.5×10^{-20} cm^2 for 1 and 5 L, respectively. For 1 L, total signal increased until ~ 4×10^{17} photons cm^{-2} (Figure 5.8). For 5 L, total signal increased for ~ 2×10^{18} photons cm^{-2}, remained approximately constant until 4.5×10^{18} photons cm^{-2}, and then began to decrease. $O(^3P_2)$ signal increases as hydroxyls accumulate on the surface. Eventually, after five times as many photons as for 1 L, an equilibrium concentration of hydroxyls is reached, and the signal is constant until less than one layer of water remains.

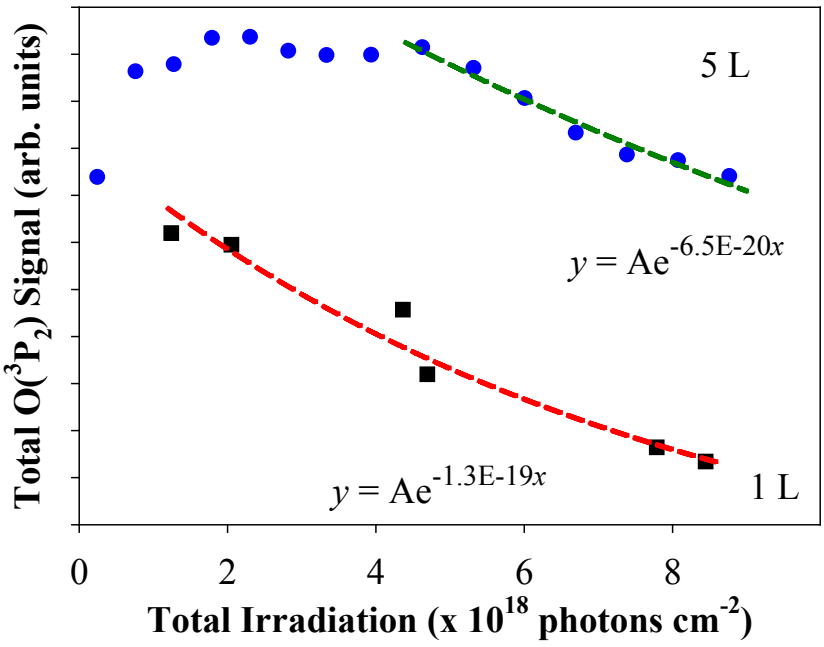

Figure 5.9. $O(^3P_2)$ desorbing from 1 L (black squares) and 5 L (blue circles) ASW on copper at 82 K as a function of total 157-nm irradiation. $O(^3P_2)$ TOF spectra were integrated from 0 to 20 μs to obtain the total signal. The dashed curves represent exponential fits of the form $y = Ae^{-\sigma x}$, where x has units of photons cm^{-2}.

5.4 Discussion

5.4.1 $O(^3P_J)$ formation by molecular elimination

$O(^3P_J)$ is a primary product of electron-stimulated dissociation of water ice, which involves a molecular elimination reaction (5.3) with a threshold of 6-7 eV.[66]

$$H_2O + e^- \rightarrow H_2 + O(^3P_J) \quad (5.3)$$

However, electrons and photons have different selection rules, and only $O(^1D)$ is observed in the molecular elimination reaction (5.4) for vacuum-ultraviolet photodissociation of gas-phase water.[97]

$$H_2O + h\nu \rightarrow H_2 + O(^1D) \quad (5.4)$$

In the condensed phase with 7.9-eV photons, reaction (5.4) leads to $O(^1D)$ desorption with T_{trans} = 800 K.[91] Quenching of these $O(^1D)$ atoms to the ground state is improbable because $O(^1D)$ readily reacts with H_2O to form H_2O_2 or 2 OH.[98]

In the condensed phase, conservation of momentum can involve neighboring water molecules, so gas-phase selection rules are not necessarily obeyed, and it is possible that molecular elimination of $O(^3P_J)$ could occur in water ice during photoexcitation. Additionally, $O(^3P_J)$ might be formed by molecular elimination if spin constraints are overcome by ionization of water and ion-electron recombination, according to reactions (5.5)-(5.7):

$$H_2O + h\nu \rightarrow H_2O^+ + e^- \quad (5.5)$$

$$H_2O^+ + e^- \rightarrow H_2O^* \quad (5.6)$$

$$H_2O \rightarrow H_2 + O(^3P_J) \quad (5.7)$$

If water is first ionized by 7.9-eV irradiation (5.5), ion-electron recombination (5.6) can produce triplet water that can subsequently dissociate according to reaction (5.7).

The water molecule produced in reaction (5.6) likely occupies the same excited state that leads to $O(^3P_J)$ during electron irradiation.[66] Although ionization of water at 7.9 eV has a low quantum yield (~2%) compared to 9.3 eV (22%), the amount of $O(^3P_J)$ formed as a result of reactions (5.5)-(5.7) may be significant compared to secondary mechanisms involving OH radicals. $O(^3P_J)$ formed in this manner is likely part of the 400 K component, as the energy corresponding to this component's peak (70 meV) is close to the energy reported for electron-stimulated desorption of $O(^3P_J)$ from D_2O ice (60 meV).[66]

5.4.2 Formation of $O(^3P_J)$ atoms through hydroxyl recombination reactions

The photodissociation of H_2O by 157-nm photons can also be described by the following equation:

$$H_2O(ads) + h\nu(157\ nm) \rightarrow H(i) + OH(i),\ E_{avail} = 2.22\ eV, \quad (5.8)$$

where "i" stands for the vacuum/ASW interface and "ads" stands for adsorbed.[74] Following photodissociation according to reaction (5.8), recombination of two hydroxyls can produce $O(^3P_J)$ and water. Four different exothermic recombination reactions of hydroxyls may be responsible for the observed $O(^3P_J)$ signal:

$$OH(i) + OH(i) \rightarrow H_2O(i) + O(^3P_J) \quad (5.9)$$

$$OH(i) + OH(i) \rightarrow H_2O(ads) + O(^3P_J) \quad (5.10)$$

$$OH(i) + OH(ads) \rightarrow H_2O(i) + O(^3P_J) \quad (5.11)$$

$$OH(i) + OH(ads) \rightarrow H_2O(ads) + O(^3P_J) \quad (5.12)$$

Enthalpies for these reactions are $\Delta_r H(5.9) = -0.73$ eV, $\Delta_r H(5.10) = -1.19$ eV, $\Delta_r H(5.11) = -0.17$ eV, and $\Delta_r H(5.12) = -0.63$ eV.[74]

Reactions (5.9) and (5.12) are close in energy and may both contribute to the observed "1800 K" component. As mentioned in Section 5.3.2, the temperature of this component was actually allowed to vary between 1600 and 2000 K in order to get the best fit for each TOF spectrum. The peak position seemed to change with increasing irradiation and with excimer laser energy. If the "1800 K" component actually results from two separate mechanisms, the behavior of this component can be rationalized. Reaction (5.9) involves two OH(i) fragments, so it should require two photons in close temporal and spatial proximity. Reaction (5.12) involves one OH(i) and one OH(ads), which is localized on the surface, so reaction (5.12) should only require one photon once a substantial number of hydroxyls have accumulated. The oxygen yield from reaction (5.9) should have a quadratic dependence on excimer energy, while the oxygen yield from reaction (5.12) should have a strong dependence on irradiation time and a linear dependence on excimer energy after significant irradiation. Therefore, it is not surprising that different peak positions were observed at different excimer energies and after differing amounts of irradiation. Because these two reactions have such similar energies, their Maxwell-Boltzmann distributions are convoluted, and both are contained in the "1800 K" component.

As discussed in Section 5.4.1, the 400 K component may be due in part to molecular elimination following ion-electron recombination. Reaction (5.11) may also contribute to this component, as it is less exothermic than reactions (5.9) and (5.12). As shown in Figure 5.8, the 400 K component increases with increasing irradiation. Reaction (5.11) involves an adsorbed hydroxyl group, so a buildup of hydroxyls due to increasing irradiation enhances the $O(^3P_J)$ signal from reaction (5.11).

Any time $O(^3P_J)$ is formed with an initial trajectory toward the surface, it may equilibrate with the surface and emerge with a translational temperature of 82 K, the surface temperature. Slower-than-thermal signal is seen for thick ASW layers because diffusion out of the porous ice takes time. As indicated in Table 5.1, both the thermal and diffusion components are much larger for J = 2 than for J = 1 or 0. When $O(^3P_{J=1 \text{ or } 0})$ thermalizes with the surface, it may also lose internal energy and fall to the ground state, where J = 2. The thermal and diffusion components may arise from all mechanisms proposed above as well as from direct photodissociation of hydroxyl groups.

No diffusion component was discussed in the similar study by Hama et al., even though their experimental data appeared to exceed the sum of the Maxwell-Boltzmann components at long flight times.[74] Because the TOF spectra we measured had similar shapes for 5 L, 50 L, and 600 L, with the exception of growing thermal and diffusion components, we would expect even larger thermal and diffusion components to be present at 1500 L exposure.

5.4.3 Formation of $O(^3P_J)$ atoms through photodissociation of adsorbed hydroxyls

As shown in Figure 5.8, the 10,000 K component is almost non-existent from freshly dosed ASW, but its signal increases rapidly with irradiation. Although none of the hydroxyl recombination reactions produce enough energy for a 10,000 K component, the photodissociation of adsorbed hydroxyls has more than enough available energy:

$$OH(ads) + h\nu(157 \text{ nm}) \rightarrow H(i \text{ or ads}) + O(^3P_J). \quad (5.13)$$

Reaction (5.13) has 2.85 eV available for H(i) or 3.03 eV available for H(ads).[74] In the gas phase, the majority of that available energy would be expected to go to the lighter H

fragment, but, since the hydroxyl is adsorbed on the surface, the partitioning of energy may depend in large part on the hydroxyl's orientation. When oxygen is pointed away from the surface, the hydrogen's initial trajectory is toward the surface. After photodissociation, the hydrogen fragment may rebound off the surface and collide with the oxygen fragment. In this scenario, much of the hydrogen's rebounded kinetic energy is transferred to the oxygen. A Maxwell-Boltzmann temperature of 10,000 K corresponds to ~1.8 eV. For H(i) in reaction (5.13), 1.8 eV corresponds to 63% of the total available energy. When the hydroxyl orientation is reversed, with H pointing away from the surface, the oxygen fragment collides with the surface and becomes part of the thermal component. A theoretical investigation of isolated OH radicals estimates the cross section for reaction (5.13) at 157 nm to be 3 x 10^{-18} cm^2.[99, 100] Therefore, after prolonged irradiation of ASW causes accumulation of surface hydroxyls, direct photodissociation of OH should contribute significantly to the observed $O(^3P_J)$ yield.

Because we measured TOF spectra at very low coverages and determined the precise value of *r* by setting the thermal component equal to the surface temperature of 82 K, we are confident that the fastest component has T_{trans} = 10,000 ± 2000 K. The peak of this component is clearly defined in Figures 5.4 and 5.5. Figures 5.6 and 5.7 show that this component was almost unnecessary for freshly dosed ASW. Like Hama et al.,[74] we observed a large increase in the fastest component after prior irradiation, so we attributed this component to the photodissociation of OH radicals.

5.4.4 Implications for the outer solar system

The E ring of Saturn is dominated by tiny water ice particles, which are replenished primarily by geysers on Enceladus.[101] When these particles are exposed to UV photons, the water may dissociate and produce $O(^3P_J)$ by the mechanisms discussed above. We can use our measured cross sections for $O(^3P_2)$ depletion to estimate the lifetime of a typical water ice particle in the E-ring due to photodissociation. More advanced models will of course include many other loss terms, as the icy grains are also expected to experience sputtering by a plasma in the magnetosphere.[102]

From Cassini's Imaging Science Subsystem, the median radius of E-ring particles has been determined to be 3.1 μm.[103] Assuming that 1 x 10^{15} molecules cm^{-2} is the density of molecules on the surface and that the particle is a sphere, there are 1.2 x 10^9 molecules on the surface of the typical E-ring particle. Since the Cassini images show E-ring particles at all stages of development, this median particle best size applies to particles that are not newly ejected from Enceladus. The typical E-ring particle will contain both H_2O and OH on the surface, since significant photodissociation has already occurred. For simplicity, we will assume that an equal number of OH and H_2O molecules are present on the surface. Since the most important $O(^3P_J)$ formation mechanisms involve hydroxyl groups, the measured $O(^3P_2)$ depletion cross sections can be considered to represent the removal of OH from the surface. Given our assumptions, there are ~ 6 x 10^8 hydroxyl groups on the typical ice grain in the E ring. We will use the cross section from 1 L ASW, σ = 1.3 x 10^{-19} cm^2, since this is the lowest coverage for which the cross section was measured. The solar photon flux near Saturn below 230 nm is 3.5 x 10^{11}

photons cm^{-2} s^{-1} (F_{ph}). The rate of $O(^3P_J)$ desorption, or hydroxyl depletion, can then be calculated according to the following equation:

$$\frac{dN}{dt} = -F_{ph}\,\sigma\,N, \tag{5.14}$$

where N is the number of OH groups on the surface. Initially, for a 3.1-μm grain, the rate of $O(^3P_J)$ desorption is 27 atoms per second, but this rate decreases as N decreases. After 840 days, only one $O(^3P_J)$ atom desorbs every second, and the radius is 0.59 μm. After 5.2 years, only one $O(^3P_J)$ atom desorbs every minute, and the radius is 0.076 μm. In general, the number of OH groups on the surface is given by the exponential equation:

$$N = N_0 e^{-F_{ph}\,\sigma\,t}, \tag{5.15}$$

where N_0 is the initial number of OH groups on the surface. For any size ice grain, the time required for the grain to shrink to half the surface area ($\tau_{1/2}$) equals $\ln(2)/F_{ph}\sigma$, ~180 days. The time required for the grain to shrink to half the radius equals $\ln(4)/F_{ph}\sigma$, ~350 days. Since the cross section in this calculation did not include H_2O photodesorption or direct photodissociation to produce $O(^1D)$, H, or OH, typical water ice particles in the E ring would be photo-destroyed in even less time. These results imply that photodissociation of ice grains in the E-ring region of Saturn may contribute $O(^3P_J)$ to the atomic oxygen cloud. More generally, there must be a replenishing source term for the ice grains that may be related to geyser activity on Enceladus.

5.5 Conclusion

Photodissociation of amorphous solid water deposited on a thinly oxidized copper substrate at 82 K was studied by measuring $O(^3P_J)$ photoproducts detected with resonance-enhanced multiphoton ionization. For each spin-orbit state, the oxygen atom

TOF spectrum was measured as a function of H_2O exposure and 157-nm irradiation time. Four Maxwell-Boltzmann distributions with translational temperatures of 10,000 K, 1800 K, 400 K, and 82 K were required to fit the data. The most likely formation mechanisms are molecular elimination following ionization of water and ion-electron recombination, secondary recombination of hydroxyl radicals, and photodissociation of adsorbed hydroxyl radicals. Evidence for diffusion out of pores in ASW was found for H_2O exposures of at least 1 L. The cross sections for $O(^3P_2)$ depletion were 1.3×10^{-19} and 6.5×10^{-20} cm^2 for 1 and 5 L, respectively. These cross sections imply that photodissociation of ice grains in the E-ring region of Saturn may contribute $O(^3P_J)$ to the atomic oxygen cloud. Given the known photon fluxes and observed grain sizes, these cross sections imply that photodissociation of ice grains in the E-ring region of Saturn may contribute $O(^3P_J)$ to the atomic oxygen cloud and that a replenishing source of ice grains is required.

CHAPTER 6

$O(^3P_J)$ FORMATION BY PHOTOIRRADIATION OF AMORPHOUS SOLID WATER ON GENUINE LUNAR SURFACES

6.1 Introduction

The measurement of oxygen in the Moon's atmosphere has been a priority of lunar scientists for many years. In 1973, scientists analyzing data from the Apollo 17 UV spectrometer placed an upper limit of 80 cm^{-3} on the concentration of atmospheric oxygen atoms near the lunar surface.[104] In 1991, re-analysis of the same data resulted in an upper limit of 500 cm^{-3}.[105] Most recently, pickup ion observations indicated large neutral abundances at mass 16, indicating a new upper limit for the density of oxygen atoms: 12,000 cm^{-3}, more than 20 times the previous optical limit.[106] This recent study also noted that some oxygen atoms were thermally equilibrated to the surface temperature, which would be surprising if they were ejected by solar-wind-ion sputtering.[106] Perhaps these unanticipated oxygen concentrations are not only due to sputtering, but also from recombination reactions of hydroxyls formed by photodissociation of water. Several studies support the presence of water on the Moon with infrared (IR) absorption data showing broad 3-μm hydration features.[23-25] The IR data show maximum absorption at 2.8 μm, indicating stretching vibrations of hydroxyls, and less intense absorptions at wavelengths greater than 3.0 μm are attributed to H_2O.

Vacuum ultraviolet irradiation of ASW has been studied extensively,[55, 57, 107, 108] but there are no reported studies that use a lunar sample as the substrate. The primary products of water photodissociation are H_2, $O(^1D)$, H, and OH. As discussed in Chapter 5, $O(^3P_J)$ may be formed through molecular elimination after ion-electron recombination

or as a secondary photoproduct by recombination or photodissociation of hydroxyls. In the present study, $O(^3P_J)$ produced by 157-nm irradiation of ASW on two lunar substrates has been measured as a function of spin-orbit (J) state, H_2O exposure, and irradiation time.

6.2 Experimental Details

All experiments were performed in the UHV chamber that was described in Chapter 3. The chamber's base pressure was 2 x 10^{-10} Torr, and background dosing of H_2O was typically performed at pressures between 1 x 10^{-8} and 5 x 10^{-8} Torr. The lunar substrates were an impact melt breccia collected during Apollo 16 (pictured in Figure 5.1) and a mare basalt collected during Apollo 17. Both slabs were porous, dark in color, and cut to be flat on one side so that efficient cooling was possible.

The experimental procedure was nearly identical to that described in Chapter 5. $O(^3P_{J=2,1,0})$ photoproducts were detected with 2 + 1 REMPI at 225.6 – 226.4 nm.[96] The time between desorption and ionization was varied from 0 to 50 μs. In order to determine the TOF spectrum of the O-atom desorbate, at each delay time the oxygen peak in the mass spectrum was integrated to obtain the total signal intensity.

As in Chapter 5, four Maxwell-Boltzmann components, $S(t, T_{trans})$, were required to adequately fit the experimental data according to Equation (5.1). Velocity distributions were also fit with four Maxwell-Boltzmann components according to Equation (5.2). The distance between the surface and the detection region based on laser alignment was 3 ± 0.5 mm for both slabs, but more precise values were determined by constraining the thermal components to have T_{trans} = surface temperature.

6.3 Results

6.3.1 REMPI spectrum

Figure 6.1 shows a representative REMPI spectrum for O(^3P_J - ^3P_J) transitions due to 157-nm irradiation of 1 L ASW on the impact melt breccia with TOF = 1.7 μs. The wavelengths shown in Figure 6.1 are in air, and the corresponding vacuum wavelengths can be found by adding ~ 0.06 nm. The ratio of the peak areas is 9.9 to 4.2 to 1 for J = 2, 1, and 0. As in Chapter 5, the shape of the TOF spectrum differs with spin-orbit state, so calculating the spin-orbit temperature at just one flight time does not make sense. Instead, the entire TOF spectrum and its components should be considered.

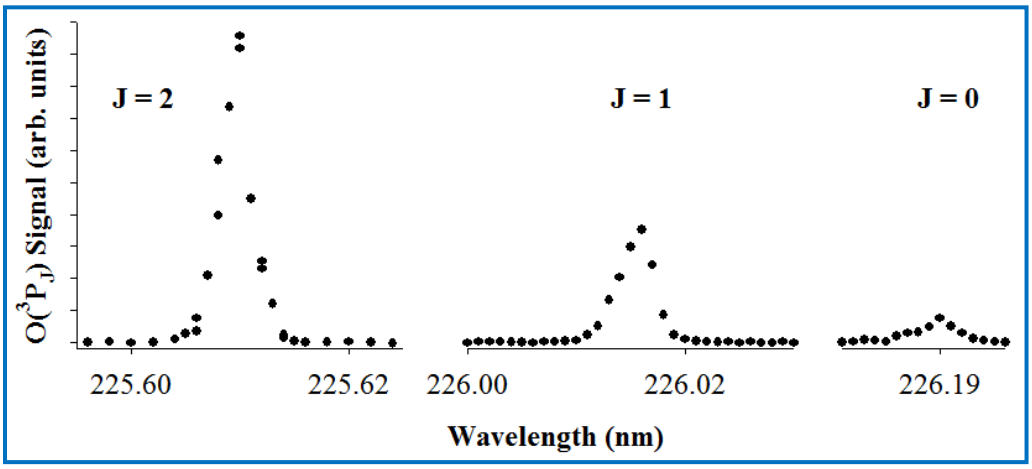

Figure 6.1. REMPI spectrum for O(^3P_J) produced by 157-nm of 1 L ASW on the impact melt breccia at 102 K.

6.3.2 Coverage and J-state dependences of TOF spectra

Figure 6.2 shows that on both lunar slabs the slow component of the O(^3P_J) TOF spectrum from 5 L ASW is much larger for J = 2 than for J = 1 or 0. When compared to

the TOF spectra in Figure 5.2, for 600 L ASW on copper, both lunar slabs have larger slow components for all spin-orbit states, but the difference is most apparent for J = 2.

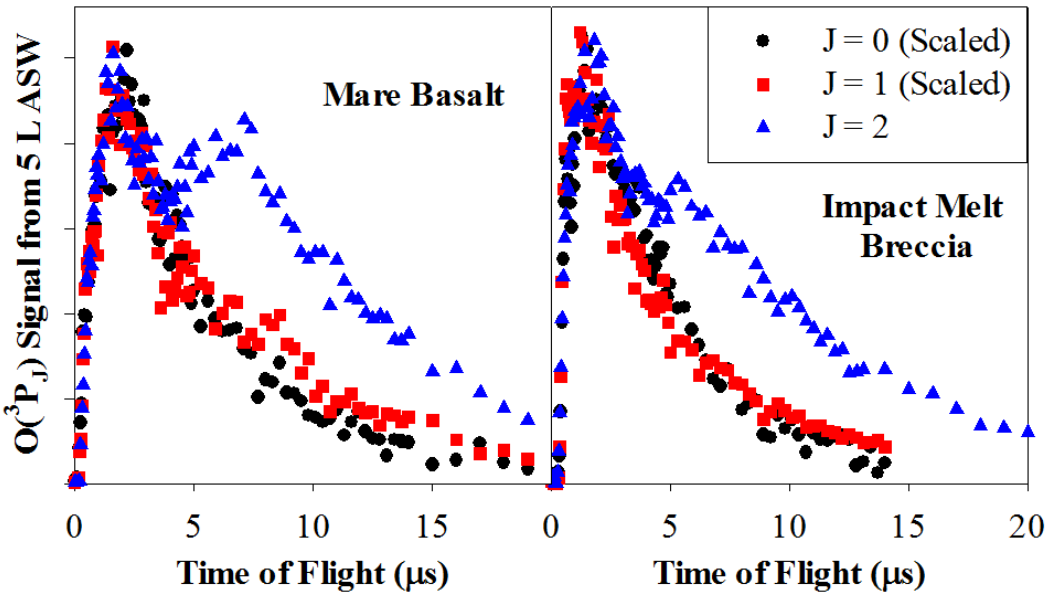

Figure 6.2. TOF spectra for $O(^3P_J)$ produced by 157-nm irradiation of 5 L ASW on the mare basalt at 89 K (left) and impact melt breccia at 102 K (right).

Figure 6.3 shows that this slow component increases with coverage for J = 2 on both lunar slabs. The magnitudes of the TOF spectra on the different lunar slabs should not be directly compared due to slightly different laser powers being used, and the two graphs in Figure 6.3 are not on the same scale. However, the relative intensities of the peaks can be compared. Clearly, the slow component is much larger relative to the other components on the mare basalt.

TOF spectra were also measured for J = 1 and J = 0 at 0.1, 1, 5, and 50 L. All of these TOF distributions were fit with a sum of four Maxwell-Boltzmann components with translational temperatures of 10,000 K, 1800 K (allowed to vary between 1600 and

2000 K to get best fit for each scan), 400 K, and the surface temperature. These are the same translational temperatures that were used to describe the TOF spectra for $O(^3P_J)$ from ASW on copper, although the relative intensities of these components differ. As in Chapter 5, signal that exceeded the sum of the four Maxwell-Boltzmann distributions at long flight times was referred to as the diffusion component. Figure 6.4 shows $O(^3P_2)$ TOF spectra on both lunar slabs for 50 L H_2O exposure, the four Maxwell-Boltzmann components, and the sum of those components. The error bars represent 95% confidence intervals calculated from several back-to-back scans after ample irradiation. Although Figure 6.4 only shows data up to 30 μs, signal was collected out to 50 μs in order to capture most of the diffusion component. The mare basalt had the most significant diffusion component, and copper had the least (see Figure 5.4).

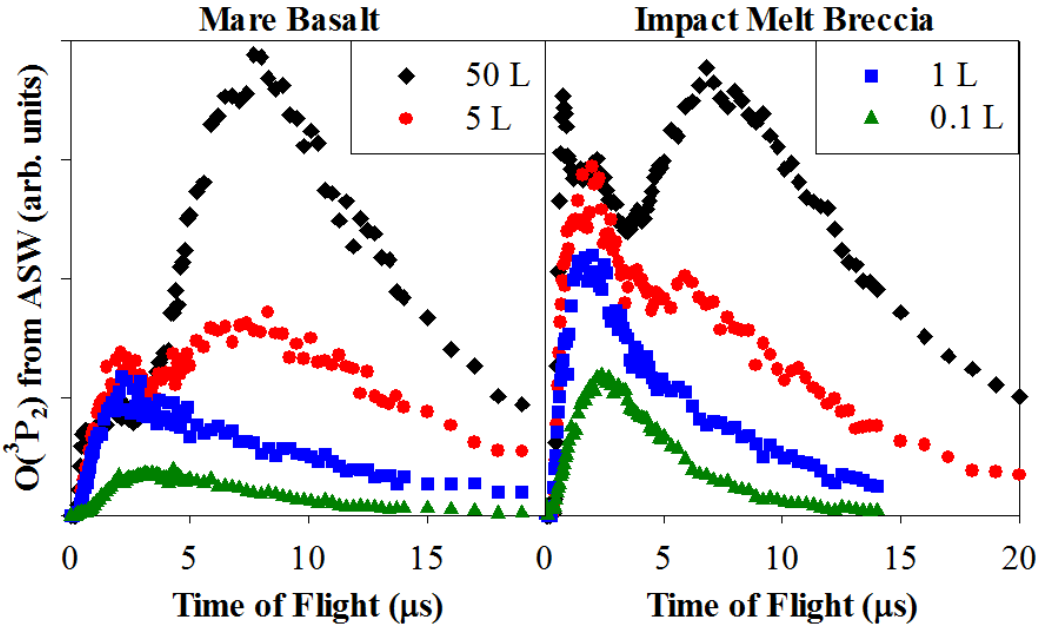

Figure 6.3. TOF spectra for $O(^3P_2)$ produced by 157-nm irradiation of 0.1, 1, 5, and 50 L ASW on the mare basalt at 89 K (left) and on the impact melt breccia at 102 K (right).

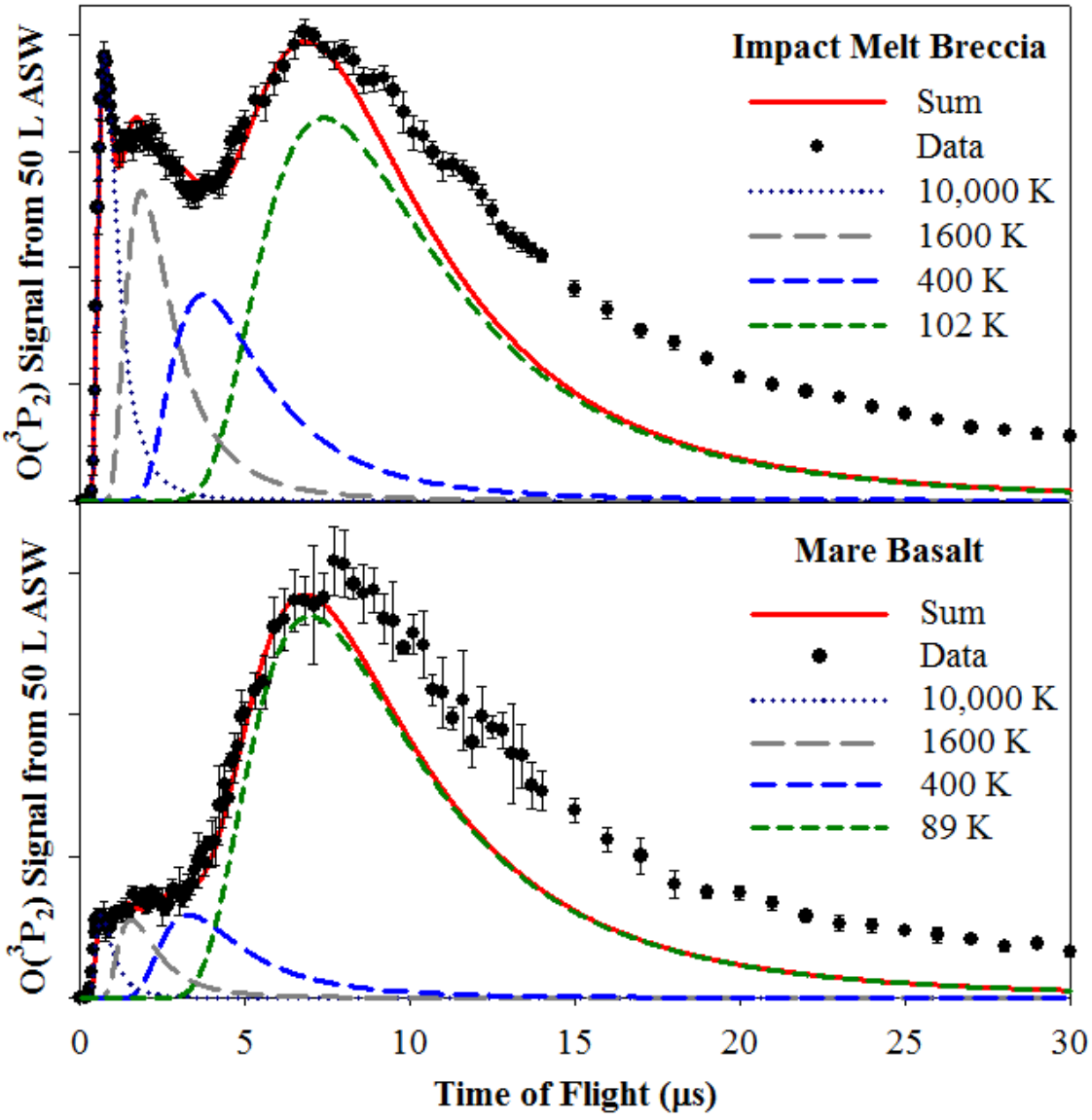

Figure 6.4. TOF spectra for $O(^3P_2)$ produced by long-term 157-nm irradiation of 50 L ASW on the impact melt breccia at 102 K (top) and on the mare basalt at 89 K (bottom). The sum of four Maxwell-Boltzmann components fits both experimental spectra well until about 8 μs. The remaining sub-thermal signals were not fit by Maxwell-Boltzmann distributions. r = 3.4 mm (top) and 3.0 mm (bottom).

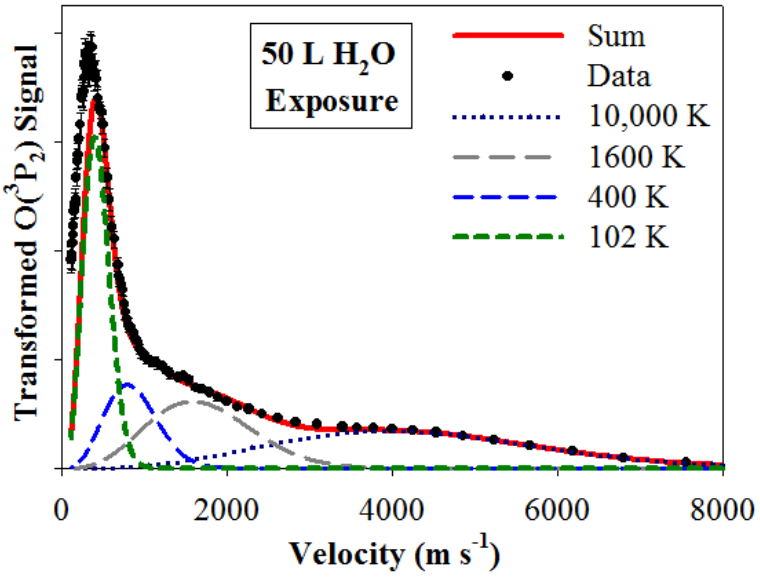

Figure 6.5. Velocity distribution for $O(^3P_2)$ produced by 157-nm irradiation of 50 L ASW on the impact melt breccia at 102 K. Four Maxwell-Boltzmann components with *r* = 3.4 mm sum to fit the data, except for the slow diffusion component.

In order to pinpoint the distance between the surface and the detection region (*r*), the thermal component of the velocity distribution needs to be fit accurately, but the large diffusion component at high H_2O exposures made such a determination difficult. Figure 6.5 shows the velocity distribution of $O(^3P_2)$ from 50 L ASW on the impact melt breccia, which could not be used to determine *r*. Instead, the velocity distribution of $O(^3P_2)$ from 1 L ASW on the impact melt breccia was used (Figure 6.6). Because the 102 K component fit the data best at 3.4 mm, that flight distance was used for all fits on the impact melt breccia. The most common velocities for $O(^3P_2)$ produced by 157-nm irradiation of 1 L ASW on the impact melt breccia were 450-950 m/s. For 50 L ASW (Figure 6.5), the most common velocities were lower (~370 m/s) due to the large diffusion component.

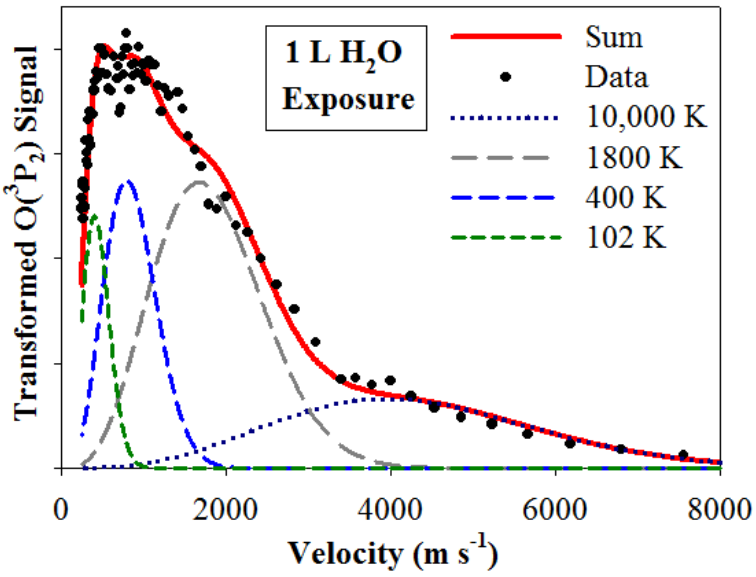

Figure 6.6. Velocity distribution for $O(^3P_2)$ produced by 157-nm irradiation of 1 L ASW on the impact melt breccia at 102 K. Four Maxwell-Boltzmann components with r = 3.4 mm sum to fit the data.

Because the diffusion component was more prominent on the mare basalt at 1 L H_2O exposure for J = 2, the velocity distribution for $O(^3P_0)$ was used to determine r (Figure 6.7). The 89 K component fit the data best at 3.0 mm, so that flight distance was used for all fits on the mare basalt. The most common velocities for $O(^3P_0)$ produced by 157-nm irradiation of 1 L ASW on the mare basalt were 350-750 m/s.

Table 6.1 summarizes the relative yields and component areas for each J state at each exposure on both lunar slabs. The relative yields on both lunar slabs are referenced to 0.1 L exposure at J = 0 (set as 1.0), but the yields on different lunar slabs cannot be compared directly since some experimental conditions, including laser powers, were not exactly the same. The rows labeled "Background" show the percentage of the total TOF area attributed to each Maxwell-Boltzmann component for scans performed without any intentional dosing of water.

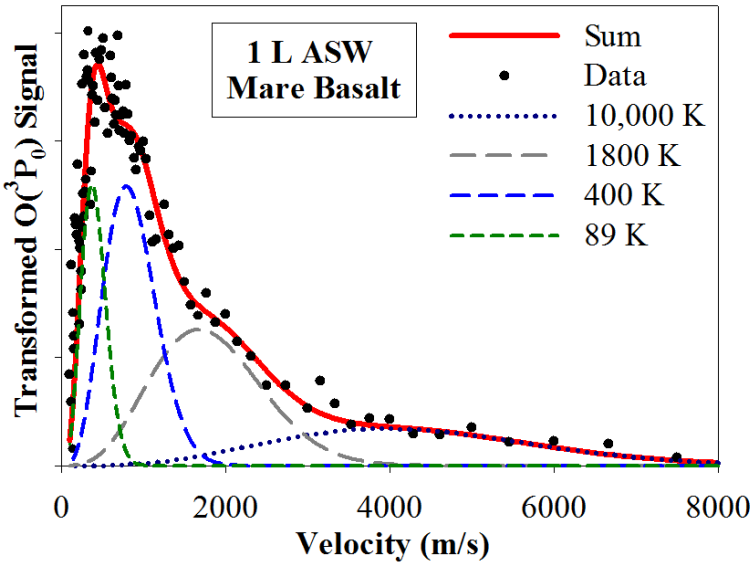

Figure 6.7. Velocity distribution for $O(^3P_0)$ produced by 157-nm irradiation of 1 L ASW on the mare basalt at 89 K. Four Maxwell-Boltzmann components with r = 3.0 mm sum to fit the data.

There was no measurable background signal after heating to 500 K over the previous night and then cooling with a background chamber pressure of 2 x 10^{-10} Torr. However, when the chamber pressure was elevated to about 1 x 10^{-9} Torr due to dosing a large amount of water the day before, even irradiating during cooling did not totally eliminate background signal. On the days when the scans on the impact melt breccia were performed, background signal was unavoidable, so it was included in Table 6.1. Therefore, "0.1 L" should be interpreted as 0.1 L plus a small amount of water deposited during cooling, which could not be quantified because irradiation during cooling was used in an attempt to keep the surface free of contaminants.

The velocity distribution of $O(^3P_2)$ measured before any intentional dosing on the impact melt breccia was nearly identical to the corresponding background velocity distribution on copper, so this signal was attributed to deposition of water from

Table 6.1. Relative yields for each TOF spectrum and percentages of TOF areas attributed to each Maxwell-Boltzmann or diffusion component on the impact melt breccia (top) and on the mare basalt (bottom).

Impact Melt Breccia	Rel. Yield	10,000 K	1800 K	400 K	102 K	Diffusion
J = 0						
Background	*0.34*	0	31.8	68.2	0	
0.1 L	*1.0*	14.3	34.5	51.2	0	
1 L	*1.8*	13.9	32.8	41.1	12.2	
5 L	*2.4*	17.6	32.0	36.6	13.8	
50 L	*3.9*	21.7	22.6	28.7	27.0	
J = 1						
Background	*0.83*	0	35.2	64.8	0	
0.1 L	*2.4*	11.5	33.4	42.4	12.7	
1 L	*4.4*	16.7	34.9	30.5	17.9	
5 L	*6.6*	17.4	29.2	28.6	24.8	
50 L	*14.0*	21.7	18.2	23.8	27.3	9.0
J = 2						
Background	*3.1*	0	19.4	69.8	10.8	
0.1 L	*8.6*	9.6	26.9	43.9	19.6	
1 L	*12.3*	5.9	24.0	18.4	28.7	23.0
5 L	*22.4*	5.8	7.2	9.6	33.9	43.5
50 L	*52.7*	6.1	5.8	10.5	26.9	50.7
50 L at 140 K	*37.2*	1.0	3.3	6.1	27.0	62.6

Mare Basalt	Rel. Yield	10,000 K	1800 K	400 K	89 K	Diffusion
J = 0						
0.1 L	*1.0*	2.6	11.8	44.6	41.0	
1 L	*2.0*	6.0	19.0	37.6	37.4	
5 L	*5.2*	7.4	26.5	32.1	29.0	5
50 L	*5.5*	5.2	15.9	20.4	34.0	24.5
J = 1						
0.1 L	*1.9*	2.5	15.3	45.0	37.2	
1 L	*5.1*	7.6	26.5	32.3	33.6	
5 L	*13.1*	6.1	22.3	23.1	33.4	15.1
50 L	*19.3*	3.2	9.1	12.9	39.8	35
J = 2						
0.1 L	*5.9*	1.1	13.1	39.4	46.4	
1 L	*22.0*	2.0	11.8	24.3	30.2	31.7
5 L	*75.9*	1.3	6.6	9.7	33.0	49.4
50 L	*143*	0.9	2.0	4.4	43.2	49.5

the UHV chamber's background rather than to oxygen intrinsic to the lunar material. It is not surprising that the rising edges of the velocity distributions in Figure 6.8 do not perfectly overlap because the copper was 20 K colder than the impact melt breccia.

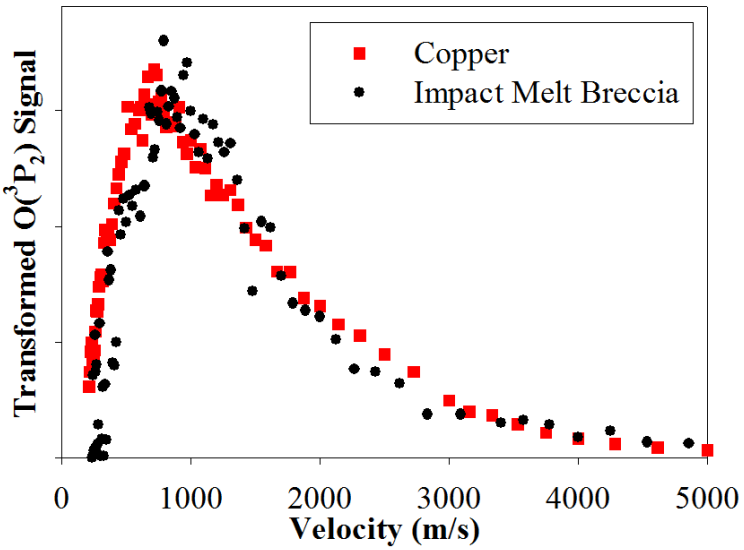

Figure 6.8. $O(^3P_2)$ velocity distributions produced by 157-nm irradiation of a thin layer of ASW background deposited on copper (82 K) and on the impact melt breccia (102 K).

Notice that the last blue row of Table 6.1 contains information about 50 L ASW at 140 K. Diffusion should be greatly enhanced by heat, and the diffusion component did indeed increase from 50.7 % to 62.6% of the total signal, even as the total yield dropped due to thermal desorption. Three components increased in magnitude with increasing coverage: 10,000 K, 102 K, and diffusion. The 1800 K and 400 K components appeared in every scan, but their magnitudes remained did not increase nearly as much as the other components with increasing ASW coverage.

Table 6.2 shows the Boltzmann temperatures of the spin-orbit levels, $T_{spin\text{-}orbit}$, associated with each TOF component and the overall yields for each exposure. The 0.1 L row for the impact melt breccia nicely illustrates the trend for components with higher translational temperatures to also have higher spin-orbit temperatures. The average overall spin-orbit temperature on the impact melt breccia was 524 K, which is similar to the 543 K average spin-orbit temperature on copper. On the mare basalt, the average overall spin-orbit temperature was 491 K, and a trend of decreasing $T_{spin\text{-}orbit}$ with increasing coverage was observed. On copper, this same trend was observed at low coverages, but the values of $T_{spin\text{-}orbit}$ for 1 to 600 L were quite similar.

Table 6.2. Boltzmann temperatures (K) of the spin-orbit levels based on component-specific and overall $O(^3P_J)$ TOF yields from ASW on the impact melt breccia (top) and on the mare basalt (bottom).

Impact Melt Breccia	**10,000 K**	**1800 K**	**400 K**	**102 K**	**Diffusion**	**Overall**
Background	N/A	2334	446	N/A		470
0.1 L	1247	865	631	102		513
1 L	Negative	9371	Negative	270		848
5 L	Negative	Negative	Negative	216		472
50 L	Negative	Negative	Negative	321	89	319
Mare Basalt	**10,000 K**	**1800 K**	**400 K**	**89 K**	**Diffusion**	**Overall**
0.1 L	Negative	966	2122	733		1130
1 L	Negative	1113	718	478		369
5 L	Negative	Negative	Negative	252	97	274
50 L	Negative	Negative	1660	167	136	189

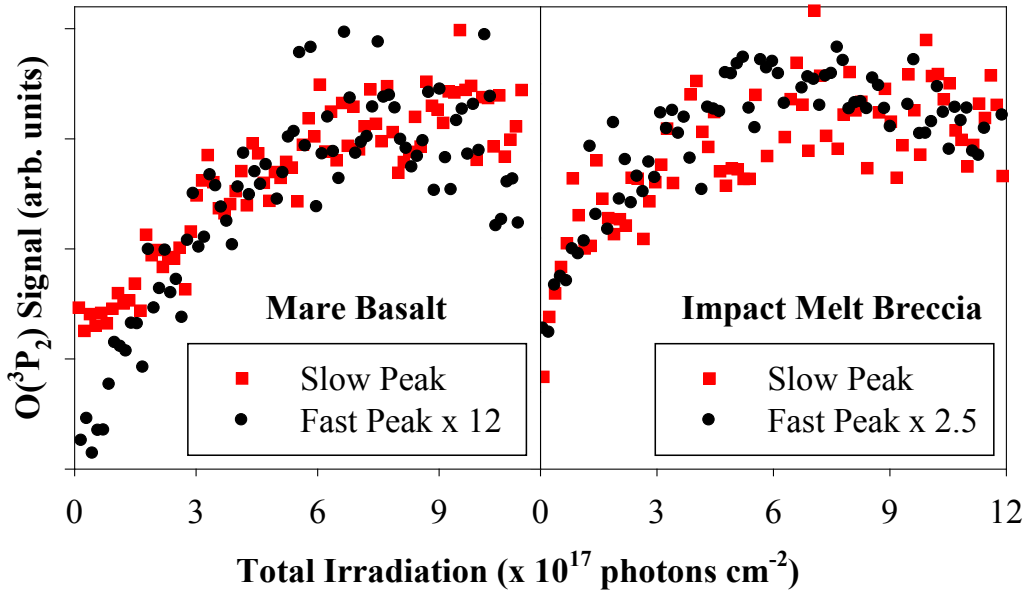

Figure 6.9. $O(^3P_2)$ signal produced by 157-nm irradiation of 50 L ASW on the mare basalt at 89 K (left) and on the impact melt breccia at 102 K (right) as a function of total irradiation. Black circles correspond to the 10,000 K component, and red squares correspond to the thermal component.

6.3.3 Irradiation dependence of TOF spectra

The TOF spectra summarized in Table 6.1 were measured after an initial period of irradiation during which signal increased rapidly, as shown in Figure 6.9. The $O(^3P_2)$ signal increased with similar rates for both the 10,000 K component (fast peak, TOF = 0.6 μs) and the 102 K component (slow peak, TOF = 7.0 μs) for 50 L ASW on the impact melt breccia. On the mare basalt, the 10,000 K (TOF = 0.45 μs) started at zero signal, while the 89 K component (TOF = 7.7 μs) started at a non-zero value and rose to 12 times the maximum height of the fast peak. The quick increase of the 10,000 K component from zero was also observed on copper (Figure 5.8).

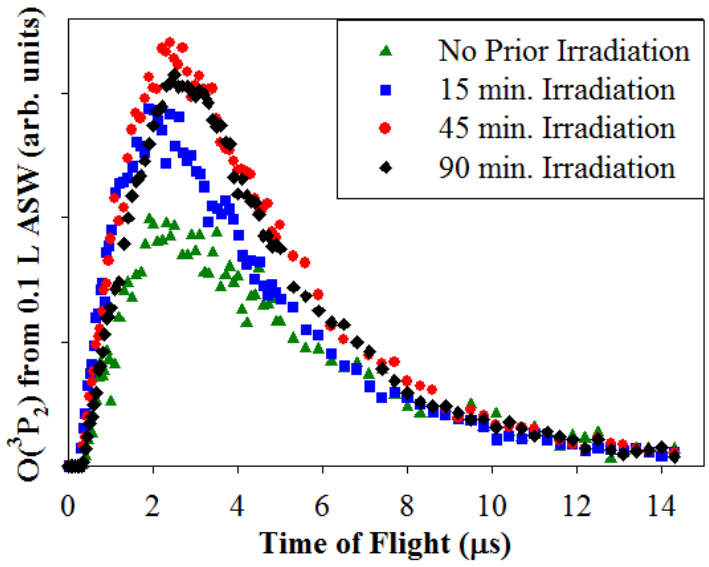

Figure 6.10. $O(^3P_2)$ TOF spectra from 0.1 L ASW on the impact melt breccia after 0, 15, 45, and 90 minutes of 157-nm irradiation.

While the irradiation time to reach maximum $O(^3P_2)$ signal was only about 4 minutes for 50 L ASW, it took much longer for signals from 0.1 – 5 L ASW to stabilize on the impact melt breccia. Figure 6.10 shows the effect of increasing irradiation on $O(^3P_2)$ signal from 0.1 L ASW. With increasing irradiation, the 400 K component increased while other components remained the same size, causing the peak maximum to shift to slightly longer times. After about 45 minutes of irradiation, the peak area started to decrease slowly. Several hours of irradiation did not make the signal disappear entirely, since the rate of background H_2O deposition eventually became comparable to the rate of $O(^3P_J)$ depletion. For higher coverages, the 400 K component is harder to pinpoint due to the increasing number and magnitude of other peaks. Similar results were obtained for 0.1 L ASW on the mare basalt, though a slightly larger thermal component was present at all irradiation times on the mare basalt (see Table 6.1).

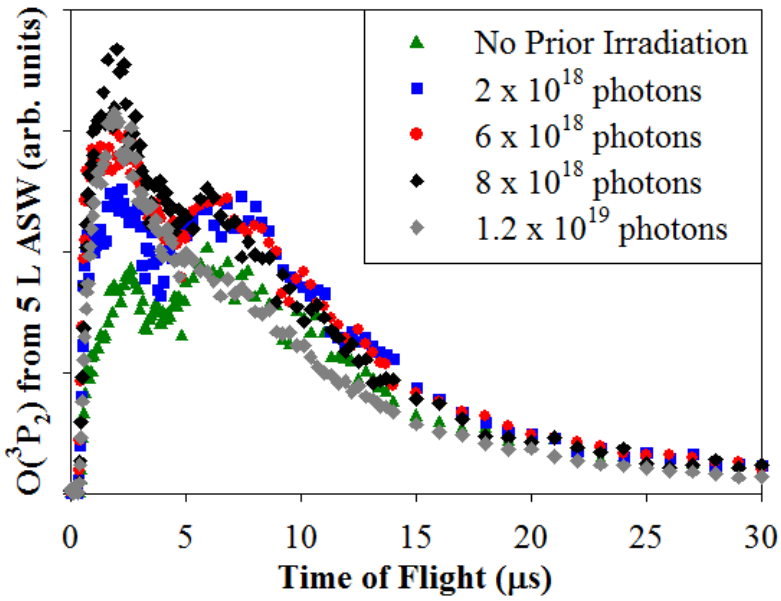

Figure 6.11. $O(^3P_2)$ TOF spectra from 5 L ASW on the impact melt breccia after irradiation by 0, 2, 6, 8, and 12 x 10^{18} photons cm^{-2}.

Figure 6.11 shows the effect of increasing irradiation on $O(^3P_2)$ signal for 5 L ASW on the impact melt breccia. Maximum total integrated signal was reached after irradiation with ~ 5 x 10^{18} photons cm^{-2}. However, the 1800 K and 400 K components continued to increase until ~ 7 x 10^{18} photons cm^{-2}, and the thermal component decreased much more quickly than the other components. Figure 6.12 shows that similar differences between components occurred on the mare basalt. The larger thermal and diffusion components on the mare basalt make this asymmetry even more obvious. Because the thermal and diffusion components were quite small on copper by comparison, no drastic changes in relative peak heights were seen on copper as overall signal decreased.

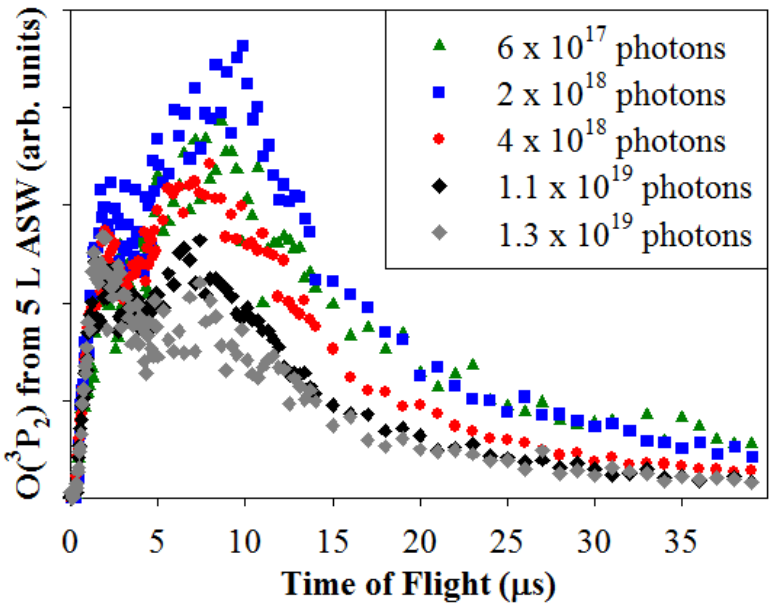

Figure 6.12. $O(^3P_2)$ TOF spectra from 5 L ASW on the mare basalt after irradiation by 0.6, 2, 4, 11, and 13 x 10^{18} photons cm^{-2}.

The TOF spectra depicted in Figures 6.11 and 6.12, along with several others, were fit with four Maxwell-Boltzmann components. The integrated areas of these components and the remaining area of the diffusion component were plotted as a function of total irradiation. Figure 6.13 summarizes these effects of total irradiation on each TOF component individually. Effective $O(^3P_2)$ depletion cross sections (σ) for each component were determined by fitting the decreasing TOF component areas with exponential equations of the form $y = Ae^{-\sigma x}$, where x has units of photons cm^{-2} and σ is the cross section for $O(^3P_2)$ depletion. As shown in Figure 6.13 (dotted lines), these cross section fits began after 5 x 10^{18} photons cm^{-2} for the impact melt breccia and after 2 x 10^{18} photons cm^{-2} for the mare basalt, as $O(^3P_2)$ signal on the mare basalt required less irradiation to reach maximum signal, probably due to the higher surface area of the mare basalt.

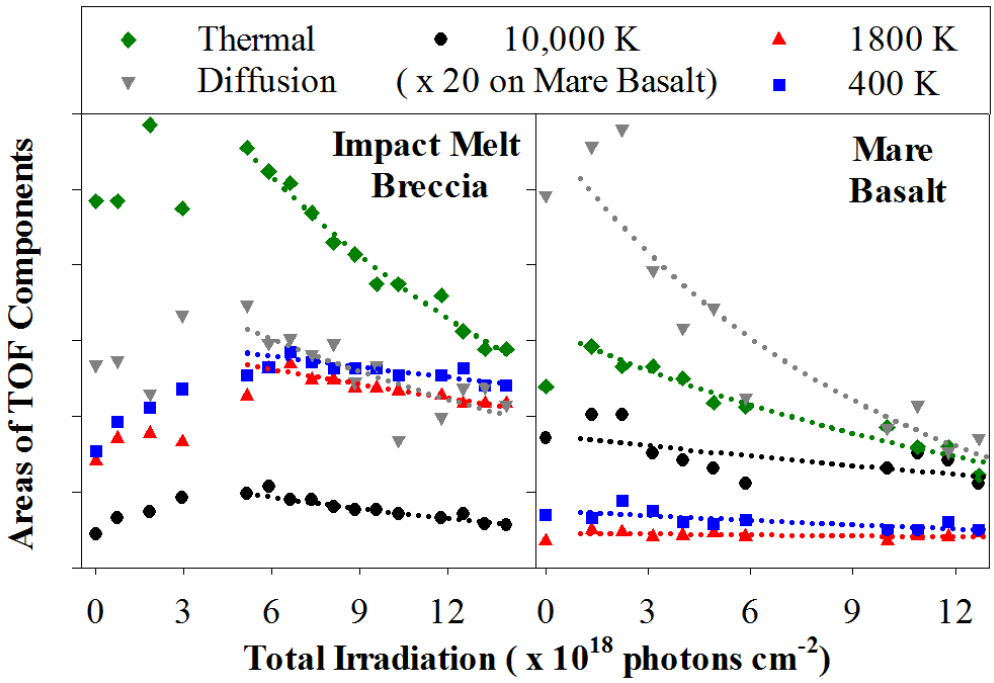

Figure 6.13. Integrated areas of components fitted to $O(^3P_2)$ TOF spectra for 5 L ASW on the impact melt breccia (left) and on the mare basalt (right). The 10,000 K component areas (black circles) were multiplied by 20 on the mare basalt for better visibility. Dotted lines represent exponential fits of the form $y = Ae^{-\sigma x}$, where x has units of photons cm^{-2}.

The component-specific cross sections are listed in Table 6.3, along with overall cross sections obtained by fitting the decreasing total yields with exponential equations. Component and overall cross sections were also obtained from 1 L ASW on both lunar slabs, and these are listed in Table 6.3 as well. For 1 L ASW on the mare basalt, the shape of the TOF spectrum did not change drastically as the intensity decreased, so the component-specific cross sections were all fairly similar. The shape of the TOF spectrum also did not appear to change for 0.1 L ASW on either lunar slab, so 0.1 L component-specific cross sections were not calculated. The overall $O(^3P_2)$ depletion cross sections from 0.1 L ASW were found to be 4.9×10^{-20} cm^2 on the impact melt breccia and 8.2 x

10^{-21} cm^2 on the mare basalt. For 50 L ASW, $O(^3P_2)$ signal did not decrease on either lunar slab within the experimental time frame, so no 50 L cross sections could be computed.

Table 6.3. Cross sections (x 10^{-20} cm^2) for $O(^3P_2)$ depletion by 157-nm irradiation of 5, 1, and 0.1 L ASW on the impact melt breccia (top) and on the mare basalt (bottom).

Impact Melt Breccia	**10,000 K**	**1800 K**	**400 K**	**102 K**	**Diffusion**	**Overall**
5 L	5.9	2.6	1.7	7.5	5.1	4.6
1L	9.6	6.6	4.1	15	-	6.6
0.1 L	-	-	-	-	-	4.9
Mare Basalt	**10,000 K**	**1800 K**	**400 K**	**89 K**	**Diffusion**	**Overall**
5 L	3.0	1.0	3.3	6.4	10.6	6.7
1L	2.9	0.7	2.9	3.4	4.3	2.8
0.1 L	-	-	-	-	-	0.82

While no clear trend with exposure was observed on the impact melt breccia, the cross sections on the mare basalt tended to decrease with decreasing exposure. This trend is the opposite of that observed for water removal cross sections (see Figure 4.7). However, these cross sections are measured at different times. The H_2O removal cross section is measured immediately following the start of irradiation, while the $O(^3P_2)$ removal cross section is measured after $O(^3P_2)$ signal reaches its maximum. Consequently, the opposite trends may actually indicate the same thing: photodissociation is more important at low coverages than at high coverages. A low rate

of $O(^3P_2)$ depletion could be due to hydroxyls on the surface being replaced by photodissociation of water almost as quickly as they react.

The $O(^3P_2)$ depletion cross section from 5 L ASW on copper was 6.5×10^{-20} cm^2, a value that is quite similar to the corresponding cross sections from the lunar slabs. However, the $O(^3P_2)$ depletion cross section from 1 L ASW on copper was 1.3×10^{-19} cm^2, which is greater than the corresponding cross sections from the lunar slabs. Unfortunately, it is difficult to extract useful information from these $O(^3P_2)$ cross section comparisons because the rate at which $O(^3P_2)$ decreases depends not only on the rate of photodissociation, but also on the concentration of adsorbed hydroxyls and the rate of recombination, which should depend on temperature and surface structure.

6.4 Discussion

6.4.1 Mechanisms of $O(^3P_J)$ formation

The mechanisms of $O(^3P_J)$ formation due to 157-nm irradiation of ASW are the same on the lunar slabs as on copper: molecular elimination, recombination of hydroxyls, and photodissociation of OH. As discussed in Section 5.4.1, $O(^3P_J)$ may be formed by molecular elimination if triplet water is produced by ionization and subsequent ion-electron recombination, according to reactions (5.5) – (5.7). The 400 K component has substantial signal from freshly dosed water, as indicated by the "Background" rows of Table 6.1, and the energy of the 400 K component (70 meV) is similar to the energy of $O(^3P_2)$ produced by molecular elimination in D_2O ice subjected to electron irradiation (60 meV).[66] Therefore, the molecular elimination mechanism may be responsible for the 400 K component.

As discussed in Section 5.4.2, $O(^3P_J)$ may be formed by hydroxyl recombination reactions following photodissociation of H_2O. Four different exothermic recombination reactions of hydroxyls are possible:

$$OH(i) + OH(i) \rightarrow H_2O(i) + O(^3P_J) \quad (6.1)$$

$$OH(i) + OH(i) \rightarrow H_2O(ads) + O(^3P_J) \quad (6.2)$$

$$OH(i) + OH(ads) \rightarrow H_2O(i) + O(^3P_J) \quad (6.3)$$

$$OH(i) + OH(ads) \rightarrow H_2O(ads) + O(^3P_J) \quad (6.4)$$

Reactions (6.1) and (6.4) are close in energy and may both contribute to the observed "1800 K" component, which was actually allowed to vary between 1600 and 2000 K in order to get the best fit for each TOF spectrum. The 400 K component may arise in part from reaction (6.3). As shown in Figure 6.10, for 0.1 L ASW on the lunar slab, this 400 K component increases more than the 1800 K component with increasing irradiation, causing the overall peak position to shift to longer times with increasing irradiation. Reaction (6.3) involves an adsorbed hydroxyl group, so a buildup of hydroxyls due to increasing irradiation enhances the $O(^3P_J)$ signal due to this reaction.

In Section 5.4.2, reaction (6.2) was not assigned to any particular Maxwell-Boltzmann component. If the released energy from that reaction (1.19 eV) goes entirely into kinetic energy and momentum conservation leads to a division of this kinetic energy among the products in a ratio determined by their masses, an upper bound of 3660 K can be calculated for the translational temperature of $O(^3P_J)$ produced by reaction (6.2). Consequently, it is probably not responsible for the 10,000 K component.

In reaction (6.2), the water molecule adsorbs, and excess internal energy is lost to the bulk through phonons. Therefore, reaction (6.2) is more likely to happen in a pore

than on the surface, as the water molecule will have more opportunity to lose its excess energy and adsorb when formed in a pore. However, $O(^3P_J)$ formed within a pore has a greater chance of making contact with the surface before being detected. These $O(^3P_J)$ atoms lose most of their kinetic energy and appear as part of the thermal and diffusion components.

Because unintentional background dosing is constant, it mimics the pulsed dosing of fresh water in the similar study by Hama et al.[74] Consequently, there is no 10,000 K component in the background TOF spectra on the impact melt breccia, as this component requires hydroxyl groups to be available for photodissociation (see Section 5.4.3). Dissociative adsorption on metal oxides was discussed in Section 1.2. While dissociative adsorption on these lunar slabs cannot be ruled out at higher temperatures, the lack of a 10,000 K component at low coverages of freshly dosed water suggests that the formation of hydroxyl groups requires irradiation at low temperatures.

Any time $O(^3P_J)$ is formed with an initial trajectory toward the surface, it may equilibrate with the surface and emerge with a translational temperature equal to the surface temperature. Slower-than-thermal signal is also observed because diffusion out of pores in the lunar slabs can take up to 20 μs. This diffusion signal is enhanced by heating, as seen in the last blue row of Table 6.1. The diffusion components are much larger on the lunar slabs than on copper due to the greater porosities of the lunar slabs. Similarly, the mare basalt appears to be more porous than the impact melt breccia, as it has larger diffusion components.

6.4.2 Effect of irradiation on ASW adsorbed on lunar slabs

As shown in Figure 6.13, irradiation of 5 L ASW on the impact melt breccia with ~ 5 x 10^{18} photons cm^{-2} was required to reach maximum signal. For 1 L ASW, < 1 x 10^{18} photons cm^{-2} was required. Similar irradiation doses were required before signal began to decrease on copper. However, there was a period of nearly constant signal on copper from 2 to 4.5 x 10^{18} photons cm^{-2} that was not observed on the impact melt breccia. It is probable that 1 L exposure is much less than one full layer of coverage, as the lunar slabs are more rough and porous than the copper surface. Apparently, 5 L is not enough water to form full layers on the impact melt breccia, so an equilibrium concentration of hydroxyls is not attained. Additionally, water may form three-dimensional clusters when adsorbed on the impact melt breccia, as the surface is expected to be mostly glassy and hydrophobic (see Section 4.2). However, it is also a multiphase material with a multitude of defects that may be amenable to water or hydroxyl chemisorption. Perhaps, once a hydroxyl group is produced, it migrates away from the ASW cluster until it finds a chemisorption site on the substrate. This migration continues to occur until the ASW islands are broken up into individually adsorbed hydroxyl groups. Because the clusters are five times larger for five times the exposure, this process requires five times as many photons for 5 L as for 1 L.

In contrast, much less irradiation was required to reach maximum signal on the mare basalt. Only ~ 2 x 10^{18} photons cm^{-2} were required to reach maximum signal at both 1 L and 5 L exposure, so it seems that water clusters are not spreading out on the mare basalt as they do on the impact melt breccia. Perhaps the increased porosity of the mare

basalt is less conducive to water clustering up on the surface, or perhaps the mare basalt is less glassy and thus interacts more favorably with water.

50 L ASW only required ~ 5 x 10^{17} photons cm^{-2} to reach maximum signal on all substrates studied. At 50 L exposure, the surface should be completely covered, so the cluster scenario no longer applies and irradiation dissociates the maximum number of water molecules per cm^2, and the top layer is most quickly hydroxylated.

6.4.3 Implications for oxygen in the lunar atmosphere

In Section 4.4.3, the flux of H_2O (v*) desorbing from the lunar surface due to ultraviolet photons was estimated. Since H_2O (v*) and $O(^3P_J)$ are both produced by hydroxyl recombination reactions, a similar calculation can be employed to estimate the flux of $O(^3P_J)$ desorbing from the lunar surface due to ultraviolet photons. Again, Goldschmidt crater will be used as an example due to its enhanced OH/H_2O signal.

The same assumptions will be made as in Section 4.4.3. The solar photon flux, F_{ph}, at the lunar surface above 8 eV is 10^{12} photons cm^{-2} s^{-1}.[79] In Goldschmidt crater, the top 0.66 nm (about 1 ML) of lunar regolith contains about 3.6 x 10^{14} water-equivalent hydrogens per cm^2.[29] Assuming that an equal number of OH groups and H_2O molecules are present, the water-equivalent hydrogens are part of 1.2 x 10^{14} OH groups and H_2O molecules cm^{-2}. Since 1 x 10^{15} molecules cm^{-2} generally corresponds to 1 L, 1.2 x 10^{14} molecules cm^{-2} roughly corresponds to 0.1 L. Since Goldschmidt crater has experienced many impact events, we choose the overall $O(^3P_J)$ depletion cross section from 0.1 L H_2O on the impact melt breccia, $\sigma = 4.9 \times 10^{-20}$ cm^2. The flux of $O(^3P_J)$, $\Phi_{O(3PJ)}$, from the sunlit parts of Goldschmidt crater due to solar photons is then:

$$\Phi_{O(3PJ)} = F_{ph} \sigma \theta \approx 5.9 \times 10^6 \text{ atoms cm}^{-2} \text{ s}^{-1}, \quad (6.5)$$

where θ is coverage in units of molecules cm^{-2}.

In order to estimate an atmospheric density of $O(^3P_J)$ from our calculated flux, we need to make a few approximations. In 1973, the Apollo 17 UV spectrometer found the density of oxygen to have an upper limit of ~80 cm^{-3} at a distance of about 100-300 km from the lunar surface.[104] As shown in Section 6.3.2, the most common velocities for $O(^3P_2)$ produced by 157-nm irradiation of 1 L ASW on the impact melt breccia were 450-950 m/s. Using 700 m/s for the velocity of every desorbing oxygen atom for simplicity, we calculate that oxygen atoms will be in the 100-300 km range for about 290 seconds. In order to calculate the density in cm^{-3}, we not only need to multiply $\Phi_{O(3PJ)}$ by 290 seconds and divide by the 200-km range, but we also need to account for the spreading out of molecules from the surface of the Moon to a larger sphere with an average radius 200 km greater than the Moon's radius (1737 km). Since area scales with the radius squared, this expansion causes the density to decrease by a factor of ~1.2. The result is a density of 71 cm^{-3}, which agrees with the optical estimate of 80 cm^{-3} from 1973.[104]

The more recent pick-up ion measurements of Halekas et al.[106] resulted in an upper limit of 12,000 cm^{-3} for the density of oxygen atoms in the lunar atmosphere. Our estimated density of 71 cm^{-3} only represents $O(^3P_J)$ atoms produced by photoirradiation, but $O(^1D)$ may be produced directly by photodissociation of H_2O and may contribute to the observed mass-16 signal in the pick-up ion measurements. Many other mechanisms of seeding the atmosphere with oxygen were also considered by Halekas et al.,[106] since the pick-up ions were observed after the Moon had been sitting in the magnetosheath's plasma for 30 hours. Furthermore, Halekas et al.[106] noted that the larger-than-anticipated

mass-16 signal could be partly due to CH_4 in the lunar atmosphere, and it could have contributions from mass-17 OH as well.

6.5 Conclusion

The formation mechanisms for $O(^3P_J)$ from ASW on the lunar slab are the same mechanisms indicated in Chapter 5 for ASW on copper, as all components had the same translational temperatures regardless of substrate. However, the results differ greatly between substrates in terms of relative peak heights. The irradiation dependence of $O(^3P_J)$ signal also depends on the substrate. The cross sections for $O(^3P_J)$ depletion from the lunar slabs, which should be correlated with hydroxyl depletion, can be used in modeling hydroxyl lifetimes on the Moon. They can also be used to estimate the density of $O(^3P_J)$ in the lunar atmosphere due to photoirradiation of water on the lunar surface.

CHAPTER 7

CONCLUSION

Water plays a central role in interstellar, planetary, and atmospheric chemistry, so understanding the interactions of water with ultraviolet photons and low-temperature surfaces is extremely important. Both H_2O and $O(^3P_J)$ photoproducts of ASW have been studied in the attempt to better understand the competition between photodesorption and photodissociation of water in the condensed phase. Because it is very difficult to distinguish between OH and H_2O in IR absorption spectra, reports of water of the Moon often conflate the two species, but a distinction needs to be made, for both scientific reasons and practical ones like making rocket fuel. Consequently, the competition between photodissociation and photodesorption of ASW has been investigated on three substrates: copper covered with a thin oxide layer, an impact melt breccia from Apollo 16, and a mare basalt from Apollo 17. Additionally, in order to better understand the observed variations in lunar water abundance with temperature, mineral composition, and crystallinity, the temperature-programmed desorption profiles of water from three lunar analogs were measured.

These temperature-programmed desorption experiments showed that glassy materials were hydrophobic, that water on multiphase materials occupied a continuum of adsorption sites, and that feldspar exhibited significant chemisorption of water. The impact melt breccia studied in Chapters 4 and 6 exhibited a characteristic of glassy materials, as expected based on its origin. As on a hydrophobic material, water formed three-dimensional clusters on the impact melt breccia, rather than spreading out to wet

the entire surface. In contrast, water on the mare basalt did not form large three-dimensional islands, as evidenced by the reduced amount of irradiation required to reach maximum $O(^3P_J)$ signal at 5 L exposure.

The photodesorption of water molecules from amorphous solid water by 157-nm irradiation has been examined using resonance-enhanced multiphoton ionization on copper and two lunar slabs. The rotational temperature of desorbing H_2O ($v = 0$) has been determined to be 425 ± 75 K on copper and 300 ± 75 K on the lunar slabs. The translational temperature of desorbing H_2O ($v = 0$) was 700 ± 200 K on oxide-coated copper. The most common velocities were similar on the lunar slabs, but the distributions were broader. Both lunar slabs are multiphase materials, so a continuum of adsorption sites should be available for chemisorption of water and hydroxyl groups. Only two TOF components were used in fitting the non-thermal desorption signal, corresponding to chemisorption through oxygen and through hydrogen, but both of these components represent a continuum of adsorption sites. In the future, adsorption of water on these genuine lunar samples will be studied more thoroughly with temperature-programmed desorption.

The cross sections for water removal at low coverages were higher on the lunar slabs than on copper. This enhancement of water removal on the lunar slabs cannot simply be explained by surface area differences, since the two lunar slabs have nearly identical cross sections at all H_2O exposures, even though the $O(^3P_J)$ TOF spectra indicate that the mare basalt is much more porous. Instead, we hypothesize that electronic interactions between adsorbed water molecules and the substrates are responsible for differences in the rates of water removal.

The branching between photodesorption and photodissociation may be different on the two lunar substrates, despite the similar overall water removal cross sections. $O(^3P_J)$ depletion cross sections on the mare basalt were found to decrease with decreasing coverage, while $O(^3P_J)$ depletion cross sections on the impact melt breccia exhibited no clear trend. Additionally, the time required to reach maximum $O(^3P_J)$ signal was greater on the impact melt breccia than on the mare basalt, indicating that water balls up in clusters on the impact melt breccia but not on the mare basalt. This behavior is expected because the impact melt breccia is glassier and the mare basalt is more porous. Consequently, at 5 L H_2O exposure, during initial irradiation when the difference in clustering is most significant, photodesorption is more likely to occur on the impact melt breccia than on the mare basalt because exciton diffusion, which reduces the likelihood of photodissociation, is possible in clusters. Similarly, photodissociation is more likely to occur on the mare basalt, where water molecules are more isolated and in pores. Because both photodissociation and photodesorption originate in the same excited state, the total water removal cross section is the same on the two lunar slabs.

There is much more research to be done regarding the complex interactions between water and lunar materials during photoirradiation. Both of the lunar substrates examined so far have been exterior surfaces of the Moon, weathered and bombarded by the solar wind for billions of years. The elemental compositions and the crystalline or amorphous structures of these exterior lunar surfaces may be quite different from the bulk rocks that have been extensively characterized. Future research will involve repeating the measurements in Chapters 3-6 on an interior lunar surface that has been cut to be flat on both sides. Having a flat surface removes the obstacle of determining a single flight

distance. Interior and exterior surfaces of the same mare basalt will be compared in order to investigate how solar wind bombardment changes the interactions of water and hydroxyls with the lunar surface.

Many additional measurements would be helpful in investigating the competition between photodissociation and photodesorption of water. REMPI detection of $O(^1D)$, OH, and H_2 during irradiation would help elucidate the mechanisms of H_2O photodissociation and OH recombination. Since water on the Moon experiences not just photoirradiation but also electron irradiation, the same TOF experiments could be performed with electrons or with electrons and photons synergistically. IR measurements of the surface during photoirradiation should show a shift in the 3-micron band from mostly H_2O to mostly OH. These IR measurements would be especially interesting because they could be directly compared to IR spectra from the Moon.

REFERENCES

1. C. A. Hibbitts, G. A. Grieves, M. J. Poston, M. D. Dyar, A. B. Alexandrov, M. A. Johnson and T. M. Orlando, Icarus **213** (1), 64-72 (2011).

2. A. J. DeSimone, V. D. Crowell, C. D. Sherrill and T. M. Orlando, Journal of Chemical Physics **139** (16), 164702 (2013).

3. P. A. Thiel and T. E. Madey, Surface Science Reports **7** (6-8), 211-385 (1987).

4. T. Cassidy, P. Coll, F. Raulin, R. W. Carlson, R. E. Johnson, M. J. Loeffler, K. P. Hand and R. A. Baragiola, Space Science Reviews **153** (1-4), 299-315 (2010).

5. M. Anand, Earth Moon and Planets **107** (1), 65-73 (2010).

6. D. E. Ramaker, Chemical Physics **80** (1-2), 183-202 (1983).

7. M. T. Sieger, W. C. Simpson and T. M. Orlando, Physical Review B **56** (8), 4925-4937 (1997).

8. S. Scheiner, Journal of Chemical Physics **75** (12), 5791-5801 (1981).

9. D. M. Chipman, Journal of Chemical Physics **124** (4), 044305 (2006).

10. J. Frenkel, Physical Review **37** (1), 17-44 (1931).

11. G. H. Wannier, Physical Review **52** (3), 0191-0197 (1937).

12. K. Kobayashi, Journal of Physical Chemistry **87** (21), 4317-4321 (1983).

13. A. Acocella, G. A. Jones and F. Zerbetto, J. Phys. Chem. Lett. **3**, 3610-3615 (2012).

14. A. B. Anderson, Surface Science **105** (1), 159-176 (1981).

15. Y. Joseph, C. Kuhrs, W. Ranke, M. Ritter and W. Weiss, Chemical Physics Letters **314** (3-4), 195-202 (1999).

16. V. M. Gun'ko, V. I. Zarko, B. A. Chuikov, V. V. Dudnik, Y. G. Ptushinskii, E. F. Voronin, E. M. Pakhlov and A. A. Chuiko, International Journal of Mass Spectrometry **172** (3), 161-179 (1998).

17. K. Watson, H. Brown and B. C. Murray, Journal of Geophysical Research **66** (9), 3033-3045 (1961).

18. S. Nozette, C. L. Lichtenberg, P. Spudis, R. Bonner, W. Ort, E. Malaret, M. Robinson and E. M. Shoemaker, Science **274** (5292), 1495-1498 (1996).

19. N. J. S. Stacy, D. B. Campbell and P. G. Ford, Science **276** (5318), 1527-1530 (1997).

20. D. B. Campbell, B. A. Campbell, L. M. Carter, J. L. Margot and N. J. S. Stacy, Nature **443** (7113), 835-837 (2006).

21. W. C. Feldman, S. Maurice, A. B. Binder, B. L. Barraclough, R. C. Elphic and D. J. Lawrence, Science **281** (5382), 1496-1500 (1998).

22. E. Robens and S. Halas, Geochronometria **33**, 23-31 (2009).

23. R. N. Clark, Science **326** (5952), 562-564 (2009).

24. J. M. Sunshine, T. L. Farnham, L. M. Feaga, O. Groussin, F. Merlin, R. E. Milliken and M. F. A'Hearn, Science **326** (5952), 565-568 (2009).

25. C. M. Pieters, J. N. Goswami, R. N. Clark, M. Annadurai, J. Boardman, B. Buratti, J. P. Combe, M. D. Dyar, R. Green, J. W. Head, C. Hibbitts, M. Hicks, P. Isaacson, R. Klima, G. Kramer, S. Kumar, E. Livo, S. Lundeen, E. Malaret, T. McCord, J. Mustard, J. Nettles, N. Petro, C. Runyon, M. Staid, J. Sunshine, L. A. Taylor, S. Tompkins and P. Varanasi, Science **326** (5952), 568-572 (2009).

26. G. R. Rossman, Water in Nominally Anhydrous Minerals **62**, 1-28 (2006).

27. A. Colaprete, P. Schultz, J. Heldmann, D. Wooden, M. Shirley, K. Ennico, B. Hermalyn, W. Marshall, A. Ricco, R. C. Elphic, D. Goldstein, D. Summy, G. D. Bart, E. Asphaug, D. Korycansky, D. Landis and L. Sollitt, Science **330** (6003), 463-468 (2010).

28. P. H. Schultz, B. Hermalyn, A. Colaprete, K. Ennico, M. Shirley and W. S. Marshall, Science **330** (6003), 468-472 (2010).

29. D. M. Hurley, D. J. Lawrence, D. B. J. Bussey, R. R. Vondrak, R. C. Elphic and G. R. Gladstone, Geophysical Research Letters **39**, L09203 (2012).

30. R. Klima, J. Cahill, J. Hagerty and D. Lawrence, Nature Geoscience **6** (9), 737-741 (2013).

31. F. S. Johnson, D. E. Evans and J. M. Carroll, Journal of Vacuum Science & Technology **9** (1), 450-456 (1972).

32. J. Goering, S. Sah, U. Burghaus and K. W. Street, Surface and Interface Analysis **40** (11), 1423-1429 (2008).

33. W. P. Jones, J. R. Watkins and T. A. Calvert, Moon **13** (4), 475-494 (1975).

34. C. S. Ray, S. T. Reis, S. Sen and J. S. O'Dell, Journal of Non-Crystalline Solids **356** (44-49), 2369-2374 (2010).

35. L. A. Taylor, C. M. Pieters, L. P. Keller, R. V. Morris and D. S. McKay, Journal of Geophysical Research-Planets **106** (E11), 27985-27999 (2001).

36. W. T. Wallace, C. J. Phillips, A. S. Jeevarajan, B. Chen and L. A. Taylor, Earth and Planetary Science Letters **295** (3-4), 571-577 (2010).

37. W. H. Casey, H. R. Westrich and G. R. Holdren, American Mineralogist **76** (1-2), 211-217 (1991).

38. J. Szanyi, J. H. Kwak and C. H. F. Peden, Journal of Physical Chemistry B **108** (12), 3746-3753 (2004).

39. A. M. Dejong and J. W. Niemantsverdriet, Surface Science **233** (3), 355-365 (1990).

40. M. J. Poston, G. A. Grieves, A. B. Aleksandrov, C. A. Hibbitts, M. D. Dyar and T. M. Orlando, Journal of Geophysical Research-Planets **118** (1), 105-115 (2013).

41. M. E. Brown, E. L. Schaller and W. C. Fraser, Astronomical Journal **143** (6), 146-152 (2012).

42. S. Vahidinia, J. N. Cuzzi, M. Hedman, B. Draine, R. N. Clark, T. Roush, G. Filacchione, P. D. Nicholson, R. H. Brown, B. Buratti and C. Sotin, Icarus **218** (1), 736-736 (2012).

43. C. Dominik, C. Ceccarelli, D. Hollenbach and M. Kaufman, Astrophysical Journal **635** (1), L85-L88 (2005).

44. K. I. Oberg, H. Linnartz, R. Visser and E. F. van Dishoeck, Astrophysical Journal **693** (2), 1209-1218 (2009).

45. M. S. Westley, R. A. Baragiola, R. E. Johnson and G. A. Baratta, Nature **373** (6513), 405-407 (1995).

46. M. Y. Kulikov, A. M. Feigin, S. K. Ignatov, P. G. Sennikov, T. Bluszcz and O. Schrems, Atmospheric Chemistry and Physics **11** (4), 1729-1734 (2011).

47. N. Nishi, H. Shinohara and T. Okuyama, Journal of Chemical Physics **80** (8), 3898-3910 (1984).

48. T. Hama, M. Yokoyama, A. Yabushita, M. Kawasaki and N. Watanabe, Nuclear Instruments & Methods in Physics Research Section B-Beam Interactions with Materials and Atoms **269** (9), 1011-1015 (2011).

49. S. Andersson and E. F. van Dishoeck, Astronomy & Astrophysics **491** (3), 907-916 (2008).

50. C. Arasa, S. Andersson, H. M. Cuppen, E. F. van Dishoeck and G. J. Kroes, Journal of Chemical Physics **132** (18), 184510 (2010).

51. M. A. Henderson, Surface Science Reports **46** (1-8), 1-308 (2002).

52. S. Warren, W. R. Flavell, A. G. Thomas, J. Hollingworth, P. M. Dunwoody, S. Downes and C. K. Chen, Surface Science **436** (1-3), 1-8 (1999).

53. D. F. Cox and K. H. Schulz, Surface Science **256** (1-2), 67-76 (1991).

54. N. G. Petrik and G. A. Kimmel, Journal of Physical Chemistry B **109** (33), 15835-15841 (2005).

55. S. Andersson, C. Arasa, A. Yabushita, M. Yokoyama, T. Hama, M. Kawasaki, C. M. Western and M. N. R. Ashfold, Physical Chemistry Chemical Physics **13** (35), 15810-15820 (2011).

56. F. M. Zimmermann and W. Ho, Surface Science Reports **22** (4-6), 127-247 (1995).

57. T. Hama, M. Yokoyama, A. Yabushita, M. Kawasaki, S. Andersson, C. M. Western, M. N. R. Ashfold, R. N. Dixon and N. Watanabe, Journal of Chemical Physics **132** (16), 164508 (2010).

58. C. M. Western, PGOPHER, a program for simulating rotational spectra, University of Bristol, http://pgopher.chm.bris.ac.uk (2010).

59. M. Yang and J. L. Skinner, Physical Chemistry Chemical Physics **12** (4), 982-991 (2010).

60. H. M. Pickett, R. L. Poynter, E. A. Cohen, M. L. Delitsky, J. C. Pearson and H. S. P. Muller, Journal of Quantitative Spectroscopy & Radiative Transfer **60** (5), 883-890 (1998).

61. J. W. C. Johns, Canadian Journal of Physics **49** (7), 944-947 (1971).

62. B. P. Bonev, M. J. Mumma, G. L. Villanueva, M. A. Disanti, R. S. Ellis, K. Magee-Sauer and N. Dello Russo, Astrophysical Journal **661** (1), L97-L100 (2007).

63. X. Y. Zhu, J. M. White, M. Wolf, E. Hasselbrink and G. Ertl, Journal of Physical Chemistry **95** (21), 8393-8402 (1991).

64. N. Watanabe, T. Horii and A. Kouchi, Astrophysical Journal **541** (2), 772-778 (2000).

65. B. Baron, D. Hoover and F. Williams, Journal of Chemical Physics **68** (4), 1997-1999 (1978).

66. G. A. Kimmel and T. M. Orlando, Physical Review Letters **75** (13), 2606-2609 (1995).

67. J. Herring-Captain, G. A. Grieves, A. Alexandrov, M. T. Sieger, H. Chen and T. M. Orlando, Physical Review B **72** (3), 035431 (2005).

68. T. Encrenaz, R. Kallenbach, T. C. Owen and C. Sotin, *The Outer Planets and their Moons*. (Springer, Dordrecht, The Netherlands, 2005).

69. A. E. Saal, E. H. Hauri, M. Lo Cascio, J. A. Van Orman, M. C. Rutherford and R. F. Cooper, Nature **454** (7201), 192-U138 (2008).

70. E. H. Hauri, T. Weinreich, A. E. Saal, M. C. Rutherford and J. A. Van Orman, Science **333** (6039), 213-215 (2011).

71. H. J. Hui, A. H. Peslier, Y. X. Zhang and C. R. Neal, Nature Geoscience **6** (3), 177-180 (2013).

72. J. P. Greenwood, S. Itoh, N. Sakamoto, P. Warren, L. Taylor and H. Yurimoto, Nature Geoscience **4** (2), 79-82 (2011).

73. P. H. Hahn, W. G. Schmidt, K. Seino, M. Preuss, F. Bechstedt and J. Bernholc, Physical Review Letters **94** (3), 4 (2005).

74. T. Hama, A. Yabushita, M. Yokoyama, M. Kawasaki and N. Watanabe, Journal of Chemical Physics **131** (11), 114511 (2009).

75. R. L. Korotev, Journal of Geophysical Research-Planets **105** (E2), 4317-4345 (2000).

76. L. Merlivat, M. Lelu, G. Nief and E. Roth, Proc. Lunar Sci. Conf. 7th, 649-658 (1976).

77. R. F. Dymek, A. L. Albee and A. A. Chodos, Proc. Lunar Sci. Conf. 6th, 49-77 (1975).

78. Kridelba.Sj, G. A. McKay and D. F. Weill, Science **179** (4068), 71-74 (1973).

79. B. V. Yakshinskiy and T. E. Madey, Nature **400** (6745), 642-644 (1999).

80. D. J. Lawrence, D. M. Hurley, W. C. Feldman, R. C. Elphic, S. Maurice, R. S. Miller and T. H. Prettyman, Journal of Geophysical Research-Planets **116**, E01002 (2011).

81. D. H. Crider and R. R. Vondrak, Journal of Geophysical Research-Planets **108** (E7), 5079 (2003).

82. G. R. Gladstone, K. D. Retherford, A. F. Egan, D. E. Kaufmann, P. F. Miles, J. W. Parker, D. Horvath, P. M. Rojas, M. H. Versteeg, M. W. Davis, T. K. Greathouse, D. C. Slater, J. Mukherjee, A. J. Steffl, P. D. Feldman, D. M. Hurley, W. R. Pryor, A. R. Hendrix, E. Mazarico and S. A. Stern, Journal of Geophysical Research-Planets **117** (E12), E003913 (2012).

83. Y. Futaana, J. Y. Chaufray, H. T. Smith, P. Garnier, H. Lichtenegger, M. Delva, H. Groller and A. Mura, Space Science Reviews **162** (1-4), 213-266 (2011).

84. H. T. Smith, R. E. Johnson, M. E. Perry, D. G. Mitchell, R. L. McNutt and D. T. Young, Journal of Geophysical Research-Space Physics **115**, A10252 (2010).

85. W. L. Tseng and W. H. Ip, Icarus **212** (1), 294-299 (2011).

86. D. E. Shemansky, P. Matheson, D. T. Hall, H. Y. Hu and T. M. Tripp, Nature **363** (6427), 329-331 (1993).

87. H. Melin, D. E. Shemansky and X. M. Liu, Planetary and Space Science **57** (14-15), 1743-1753 (2009).

88. T. A. Cassidy and R. E. Johnson, Icarus **209** (2), 696-703 (2010).

89. A. J. Farmer, Icarus **202** (1), 280-286 (2009).

90. S. Kempf, U. Beckmann, G. Moragas-Klostermeyer, F. Postberg, R. Srama, T. Economou, J. Schmidt, F. Spahn and E. Grün, Icarus **193** (2), 420-437 (2008).

91. T. Hama, A. Yabushita, M. Yokoyama, M. Kawasaki and N. Watanabe, Journal of Chemical Physics **131** (11), 114510 (2009).

92. T. Hama, A. Yabushita, M. Yokoyama, M. Kawasaki and S. Andersson, Journal of Chemical Physics **131** (5), 054508 (2009).

93. S. Andersson, A. Al-Halabi, G. J. Kroes and E. F. van Dishoeck, Journal of Chemical Physics **124** (6), 064715 (2006).

94. S. Andersson, G. J. Kroes and E. F. van Dishoeck, Chemical Physics Letters **408** (4-6), 415-421 (2005).

95. O. Votava, D. F. Plusquellic and D. J. Nesbitt, Journal of Chemical Physics **110** (17), 8564-8576 (1999).

96. Y. Matsumi, N. Shafer, K. Tonokura, M. Kawasaki, Y. L. Huang and R. J. Gordon, Journal of Chemical Physics **95** (10), 7311-7316 (1991).

97. L. J. Stief, W. A. Payne and R. B. Klemm, Journal of Chemical Physics **62** (10), 4000-4008 (1975).

98. W. Zheng, D. Jewitt and R. I. Kaiser, Physical Chemistry Chemical Physics **9** (20), 2556-2563 (2007).

99. E. F. Vandishoeck, S. R. Langhoff and A. Dalgarno, Journal of Chemical Physics **78** (7), 4552-4561 (1983).

100. E. F. Vandishoeck and A. Dalgarno, Journal of Chemical Physics **79** (2), 873-888 (1983).

101. F. Postberg, S. Kemp, J. K. Hillier, R. Srama, S. F. Green, N. McBride and E. Grun, Icarus **193** (2), 438-454 (2008).

102. R. E. Johnson, M. Fama, M. Liu, R. A. Baragiola, E. C. Sittler and H. T. Smith, Planetary and Space Science **56** (9), 1238-1243 (2008).

103. A. P. Ingersoll and S. P. Ewald, Icarus **216** (2), 492-506 (2011).

104. W. G. Fastie, P. D. Feldman, R. C. Henry, H. W. Moos, C. A. Barth, G. E. Thomas and T. M. Donahue, Science **182** (4113), 710-711 (1973).

105. P. D. Feldman and D. Morrison, Geophysical Research Letters **18** (11), 2105-2108 (1991).

106. J. S. Halekas, A. R. Poppe, G. T. Delory, M. Sarantos and J. P. McFadden, Journal of Geophysical Research-Planets **118** (1), 81-88 (2013).

107. A. Yabushita, T. Hama, M. Yokoyama, M. Kawasaki, S. Andersson, R. N. Dixon, M. N. R. Ashfold and N. Watanabe, Astrophysical Journal Letters **699** (2), L80-L83 (2009).

108. A. Yabushita, T. Hama, D. Iida, N. Kawanaka, M. Kawasaki, N. Watanabe, M. N. R. Ashfold and H. P. Loock, Journal of Chemical Physics **129** (4), 044501 (2008).